Fakultät Maschinenbau
fortschritt studieren

RUHR
UNIVERSITÄT
BOCHUM

RUB

Development of Efficient Numerical Methods for Non-Ideal Compressible Fluid Flows in Propulsion and Power

Dissertation
zur
Erlangung des Grades
Doktor-Ingenieur

der
Fakultät Maschinenbau
der Ruhr-Universität Bochum

von

Pascal Post

aus Diez

Bochum 2020

Thesis submitted:	04 June 2020
Thesis defense:	28 August 2020
Thesis Advisor:	Prof. Dr. Francesca di Mare Ruhr-Universität Bochum, Germany
Secondary Referee:	Prof. Dr.-Ing. Uwe Gampe Technische Universität Dresden, Germany

Abstract

Numerical modeling and simulation is central to modern industrial design. Virtualization of the whole product life cycle will increasingly require the intensive use of high-fidelity CFD simulations. The relevance of non-ideal gas effects in modern turbomachinery applications increases continuously with the demand for innovative net-zero power supply technologies, like ORC, supercritical CO_2 Brayton Cycles or geothermal steam applications, in addition to traditional steam turbines.

The design of computational methods for the accurate, robust and efficient prediction of flows in such devices is very involved and subject of the presented work. In addition to a state-of-the-art solution method for general application for the prediction of non-ideal gas flows, including scale resolving simulations of shocked condensing multi-phase flows, a solution method for highly accurate numerical experiments in terms of direct numerical simulation of geometrically simple configurations is presented.

These solution methods are thoroughly validated for their application in scale resolving computations and the capabilities are demonstrated showing a range of results for wet steam, ORC and supercritical CO_2 applications. This includes the presentation of the first large eddy simulation in the field of condensing wet steam flows, which is demonstrated to reproduce the experimental data much better compared to state-of-the-art computation techniques in this field.

Contents

1 Introduction

> *But we shall not satisfy ourselves simply with improving steam and explosive engines or inventing new batteries; we have something much better to work for, a greater task to fulfill. We have to evolve means for obtaining energy from stores which are forever inexhaustible, to perfect methods which do not imply consumption and waste of any material whatever.*
>
> Nikola Tesla, 1897

Numerical modeling and simulation is central to modern industrial design and optimization. Virtualization of the whole product life cycle (design, production, repair, maintenance and overhaul) by means of virtual prototypes will not only allow for better design but also for accurate predictions of life-cycle duration, enhanced overhaul and maintenance cycles, supported by a prediction of failure scenarios, and an overall reduction of production and maintenance costs. This requires intensive use of high-fidelity computational fluid dynamics (CFD) simulations at all stages of the industrial process. However, the design of predictive CFD methods is especially challenging as soon as thermo-physical characteristics of the fluid flow like supercritical, dense-gas and two-phase effects impede the use of idealized gas laws.

The relevance of such real gas effects in modern turbomachinery applications increases continuously. In addition to "traditional" steam turbines, with challenging condensation effects in the low-pressure stages, innovative cycles for the efficient exploitation of low temperature heat sources, like the Organic Rankine Cycle (ORC) and the supercritical CO_2 Brayton Cycle or steam in geothermal applications, gain in importance. In general, operating pressures in modern propulsion and energy systems are continuously increasing to attain higher efficiencies such that the working fluid reaches conditions close to and above the critical point, where strong real gas effects arise. Other examples are humid air effects in the intake of a jet engine or ingestion of water into gas turbines. The high technical relevance of such non-ideal gas effects renders the ability to accurately forecast their behavior in technical devices of paramount importance.

To date, the design process of technical systems is primarily based on the solution of the Raynolds-averaged Navier-Stokes (RANS) equations. For turbomachinery applications with high flow speeds, density based solution methods, adapted to the hyperbolic nature of compressible flows, are particularly suited. However, these methods are characterized by a strong coupling of underlying flow physics to numerical discretization, necessitating not only the efficient inclusion of real gas thermodynamics but also the adaption of the solution method to the particular formulation of the employed state equation. Furthermore, upwind schemes and boundary conditions, frequently derived based on idealized gas behavior assumptions, must be extended to account for real gas properties.

In this context, this work presents a newly developed turbomachinery optimized, density-based CFD solver targeted to the application in compressible non-ideal gas flows based extensively on tabulation techniques and with a hybrid CPU/GPU parallelization to exploit the computational power of modern computer architectures. On this basis, a wide range of real gas applications in turbomachines is presented including condensing wet steam flows in low-pressure steam turbines, a radial supercritical CO_2 compressor and a supersonic axial ORC turbine (an analysis of humid air effects in an axial compressor operated at ambient conditions is presented in [76]). After its validation based on RANS, the solution method is extended to large eddy simulation (LES), where special care is paid to the choice of the numerical discretization especially in the presence of shock-waves, because the energy transfer process is strongly affected by the dissipation properties of the numerical scheme. This implementation is used to present the first LES in the field of condensing wet steam flows. Results indicate that the inherent unsteady nature of the condensation process and its interaction with other unsteady flow phenomena is much better captured by LES compared to RANS and unsteady RANS (URANS).

The accuracy of the involved LES and RANS closure models in real gas flows has not been properly assessed up to now due to the lack of experimental and numerical reference data. To assess and potentially improve existing models in non-ideal gas flows a wide range of reliable direct numerical simulation (DNS) results are needed, for which a high-order finite difference method (FDM) solver with a hybrid energy-consistent weighted essentially non-oscillatory (WENO) scheme aimed for future detailed numerical investigation of shock-turbulence interaction (STI) in real gas flows is also presented. The highly optimized implementation on GPUs is demonstrated to allow the direct use of the very involved Span-Wagner equation of state for CO_2 for DNS computations in [134].

The work will be organized as follows: After this initial motivation for re-

search in the field of compressible non-ideal gas flows in turbomachines, the mathematical model of a single-phase real gas flow with general expressions for state equation and constitutive relations is introduced in chapter 2. On this basis, RANS and LES approaches to turbulent flows are discussed and an overview of relevant equations of state and techniques for their tabulation is given. Formulations in a rotating frame of reference, relevant to turbomachinery applications, are presented next. Finally, details of the current state-of-the-art modeling of condensing wet steam flows are presented. Chapter 3 describes numerical solution strategies to solve the introduced systems of partial differential equations in initial-boundary value problem (IBVP) settings. Following the method of lines approach, the spatial discretization is introduced first, containing descriptions of a 2^{nd} order finite volume method (FVM) and a high-order finite difference method (FDM) targeted at high-speed compressible flows of non-ideal working media. For the computation of the advective fluxes, real gas extensions of Roe and AUSM+ schemes are discussed, followed by details about the solution strategy for scale resolving computations, like DNS and LES. After the spatial discretization, time integration and real gas extensions of boundary conditions are presented, as applied in this work. Chapter 4 reports results of wet steam computations, starting with classical nozzle test cases for validation and RANS results of a turbomachinery configuration. On this basis, the first scale resolving computation in the field of condensing wet steam flows is presented. As further examples of the application of the presented solution method to real gas flows, results of a partially admitted axial supersonic ORC turbine for heat recovery in automotive applications and a radial compressor test case operating at supercritical CO_2 conditions are described in chapter 5 and chapter 6, respectively. This work closes with concluding remarks in chapter 7.

2 Mathematical Model

> *There is a physical problem that is common to many fields, that is very old, and that has not been solved. It is not the problem of finding new fundamental particles, but something left over from a long time ago—over a hundred years. Nobody in physics has really been able to analyze it mathematically satisfactorily in spite of its importance to the sister sciences. It is the analysis of circulating or turbulent fluids.*
>
> Richard Feynman (Nobel laureate)
> The Feynman Lectures on Physics Vol. 1

The first step towards the development of efficient numerical methods for non-ideal compressible fluid flows in propulsion and power is the definition and selection of a mathematical model, for which then a solution method can be developed. The mathematical model defines the level of approximation to the real physical process under consideration and casts it into a form, that can be solved applying mathematical solution strategies. The equations describing the dynamics of fluid motion, well known since the second half of the 19th century from the work of Navier and Stokes in particular [67], are extremely complicated (section 2.1). They form a system of nonlinear partial differential equations (PDEs), where the nonlinearity leads to the existence of turbulence, shock waves, spontaneous unsteadiness of flows, such as the vortex shedding behind a cylinder, possible multiple solutions and bifurcations [67]. The physical properties of the considered working fluid are introduced by additional constitutive laws, i.e., thermodynamic equations of state (section 2.1.1) and equations for transport properties like viscosity and heat conductivity (section 2.1.2). For non-ideal fluid flows, the conventionally applied assumption of idealized gas behavior is not applicable, increasing the overall complexity of the mathematical model and in consequence their numerical treatment enormously.

The complexity of the mathematical description of the Navier-Stokes equations in rotating domains of turbomachinery applications can be strongly reduced, formulating the Navier-Stokes equations in the rotating rather than the absolute (inertial) frame of reference (section 2.1.3).

Most technically relevant flows are in the turbulent flow regime characterized by the presence of statistical fluctuations of all the flow quantities (section 2.2), where their complete resolution, referred to as direct numerical simulation (DNS), is impossible in almost all relevant cases, even with modern computational resources. Consequently, appropriate modeling assumptions and simplifications have to be introduced to deal with turbulent flows. Considering the turbulent fluctuations as superimposed on mean or averaged values gives raise to the so-called Raynolds-averaged Navier-Stokes (RANS) equations (section 2.2.2). A reduction in complexity, more appropriate to retaining the basic three-dimensional unsteady nature of the Navier-Stokes equations, can also be achieved performing a spatial filtering, introducing a certain cutoff in size below which the turbulent fluctuations are not resolved. This is the basic idea of the large eddy simulation (LES) technique (section 2.2.1).

Adding to this basic flow description more complex phenomena of non-ideal gas flows like multiple phases and species, with effects of condensation, evaporation or chemical reactions, requires additional modeling in terms of physical laws. Describing these processes often involves physically justified trade-offs between accuracy and simplifications to their complexity. As relevant to this work, specifics to the description of condensation in turbomachines (section 2.3) are discussed.

2.1 Single-phase gas flows

The governing equations of fluid dynamics are based on the continuum assumption and consist of conservation and constitutive laws. Balancing mass, momentum and total energy results in the three fundamental principles of fluid dynamics: conservation of mass, conservation of momentum (Newton's second law) and conservation of the total internal energy (a generalization of the first law of thermodynamics). The resulting three-dimensional Navier-Stokes equations can be cast in differential (weak) conservative form

$$\partial_t \underline{w} + \operatorname{div} \underline{\underline{F}}\left(\underline{w}\right) = \underline{s}\left(\underline{w}\right), \tag{2.1}$$

with the source term $\underline{s}$ and the vector of unknowns comprising the conservative variables density, specific momentum and specific total internal energy density

$$\underline{w}\left(\underline{x}, t\right) := \left(\varrho, \varrho \underline{u}, \varrho E\right). \tag{2.2}$$

It is convenient to split the non-linear flux tensor in advective and diffusive fluxes

$$\underline{\underline{F}}\left(\underline{w}\right) = \underline{\underline{F}}^{a}\left(\underline{w}\right) - \underline{\underline{F}}^{d}\left(\underline{w}\right) \tag{2.3}$$

$$\underline{\underline{F}}^{a}\left(\underline{w}\right) := \left(\varrho\underline{u}, \varrho\underline{u}\otimes\underline{u} + p\left(\underline{w}\right)\underline{\underline{I}}, \varrho\underline{u}\left(E + p\left(\underline{w}\right)/\varrho\right)\right) \tag{2.4}$$

$$\underline{\underline{F}}^{d}\left(\underline{w}\right) := \left(\underline{0}, \underline{\underline{\tau}}\left(\underline{w}\right), \underline{\underline{\tau}}\left(\underline{w}\right)\cdot\underline{u} - \underline{q}\left(\underline{w}\right)\right), \tag{2.5}$$

where $\underline{\underline{I}}$ denotes the identity tensor. For the density-based solution approach pursued in this work, advective and diffusive fluxes are solved separately taking into account their distinct physical nature: transport by bulk motion and transport by molecular agitation, where only the latter can be present when the fluid is at rest [67]. When diffusion effects are neglected $\underline{\underline{F}}^{d} \simeq \underline{0}$, i.e., $\underline{\underline{F}} = \underline{\underline{F}}^{a}$, eq. (2.1) is referred to as the three-dimensional Euler equations.

There is some freedom in choosing a set of variables to describe the flow under consideration [181]. Instead of the conservative variables $\underline{w}$ resulting naturally from the fundamental conservation laws, it is sometimes convenient to express the Navier-Stokes equations in terms of the primitive variables density, velocity and pressure

$$\underline{w}_{p} := \left(\varrho, \underline{u}, p\right). \tag{2.6}$$

However, computationally there are big advantages in expressing the governing equations in terms of the conserved variables, because formulations based on variables other than the conserved variables (non–conservative formulations) fail at shock waves [181] and do not guarantee the conservation property of numerical methods, see chapter 3. Therefore, only conservative methods are used in this work.

The stated system of governing partial differential equations (2.1) is insufficient to completely describe the dynamics of compressible fluid flows, as it contains more unknowns than equations. Thus, closure conditions are required, dedicated to the physical nature of the fluid under consideration.

The first class of additional constitutive laws is given by thermodynamic equations of state, where the thermodynamic state of single-component flows in thermodynamic equilibrium is uniquely determined by two independent state variables. The natural choice for the employed conservative methods are density and specific internal energy (ϱ, e); with the definition of the specific total internal energy

$$E := e + \underline{u}\cdot\underline{u}/2, \tag{2.7}$$

they can directly be calculated from the resulting state $\underline{w}$

$$\varrho\left(\underline{w}\right) = \varrho \tag{2.8}$$

$$e\left(\underline{w}\right) = \left(\varrho E - \varrho\underline{u}\cdot\varrho\underline{u}/(2\varrho)\right)/\varrho. \tag{2.9}$$

Therefore, the mathematical description of the advective fluxes (2.4) is closed by the generalized equation of state

$$p := p\left(\varrho, e\left(\underline{w}\right)\right), \tag{2.10}$$

resulting in

$$\underline{\underline{F}}^{a}\left(\underline{w}\right) := \left(\varrho\underline{u}, \varrho\underline{u} \otimes \underline{u} + p\left(\varrho, e\left(\underline{w}\right)\right)\underline{\underline{I}}, \varrho\underline{u}\left(E + p\left(\varrho, e\left(\underline{w}\right)\right)/\varrho\right)\right). \tag{2.11}$$

To close the diffusive fluxes (2.5), the second class of closure condition contains additional constitutive relations for viscous stress tensor and heat flux vector. In this work, the viscous stress tensor is given assuming Newtonian fluids and applying Stokes' hypothesis

$$\underline{\underline{\tau}}\left(\underline{w}\right) := \mu\left(\varrho, e\left(\underline{w}\right)\right)\left(\operatorname{grad}\underline{u}\left(\underline{w}\right) + \left(\operatorname{grad}\underline{u}\left(\underline{w}\right)\right)^{\mathsf{T}} - 2/3\ \operatorname{div}\underline{u}\left(\underline{w}\right)\ \underline{\underline{I}}\right), \tag{2.12}$$

where the dynamic viscosity of the fluid $\mu\left(\varrho, e\left(\underline{w}\right)\right)$ depends on the thermodynamic state given by the independent state variables. Similarly, the heat flux is computed applying Fourier's law

$$\underline{q}\left(\underline{w}\right) := -\lambda\left(\varrho, e\left(\underline{w}\right)\right)\operatorname{grad} T\left(\varrho, e\left(\underline{w}\right)\right), \tag{2.13}$$

with the thermal conductivity $\lambda\left(\varrho, e\left(\underline{w}\right)\right)$ in function of the thermodynamic state and the generalized equation of state $T\left(\varrho, e\left(\underline{w}\right)\right)$ for the temperature.

Equations of state and relations providing viscosity and thermal conductivity must be provided for the working fluid being considered and are often not directly formulated in terms of (ϱ, e), necessitating an iteration procedure. A whole range of different equations of state and equations for transport properties are used in this work, introduced in the following.

2.1.1 Equations of State

Experience from classical thermodynamics shows that the thermodynamic state of a generic system is uniquely determined by n state variables X_n. Therefore, a dependent state variable Y can be determined by the generic relation

$$Y = Y\left(X_1, X_2, \ldots, X_n\right), \tag{2.14}$$

called equation of state (EoS). For single-component flows in thermodynamic equilibrium, the thermodynamic state is uniquely determined by two independent intensive state variables

$$Y = Y\left(X_1, X_2\right), \tag{2.15}$$

which are of arbitrary choice. State equations, which can also be given in form of a diagrams or tables, cannot be derived from principles of classical macroscopic thermodynamics. For gases, equations of state can be found on the basis of specific molecular models from statistical and quantum mechanics or by measurements.

Any relation involving only the thermal state variables, p, ϱ, or its reciprocal, the specific volume $v = 1/\varrho$, and T, is called thermal equation of state. A caloric equation of state refers to every relation including caloric state variable, like internal energy e, enthalpy h or entropy s. Thermal and caloric equations of state for a given fluid are closely related and necessary for the complete thermodynamic description, where the choice of a thermal EoS only restricts the choice of a caloric EoS but does not determine it [181].

The essential step from classical thermodynamics of reversible homogeneous processes to the thermodynamics of irreversible processes of fluid dynamics is the assumption that exactly the same equations of state govern fluids at rest as fluids in motion [169]. I.e., the thermodynamic state does not depend on the fluid motion and, although it changes from place to place, it is not dependent on the gradients of the state variables [169].

In this sense, we are concerned with macroscopic properties of a fluid without appealing to the individual molecular and atomic particles of which it is composed, where the macroscopic properties represent suitable averages over microscopic properties [5]. However, the real gas behavior is a manifestation of these microscopic properties and will be briefly discussed in the following as to understand the underlying assumptions of idealized gas behavior and why this assumption does not hold in the fluid flows considered in this work.

One can imagine a fluid to be made up of molecules in random motion, frequently colliding with neighboring molecules. Each molecule is surrounded by a force field, produced by electromagnetic action of the electrons and nuclei of the molecule [5]. This force field governs the interaction of the molecules and is hence referred to as the intermolecular force. A qualitative representation of the variation of the intermolecular force of a single molecule with distance is given in fig. 2.1. At small distances, the force is strongly repulsive, tending to push molecules away from each other, while the intermolecular force rapidly decreases with distance, even becoming a weak attractive force [5]. At a distance of approximately 10 molecular diameters away from the molecule, the magnitude of the intermolecular force is negligible [5]. I.e., intermolecular forces generally affect the molecular motions, which in turn influences the macroscopic thermodynamic properties of the fluid under consideration and, therefore, the intermolecular forces in real gases must be accounted for [5]. Only if the molecules are spaced ap-

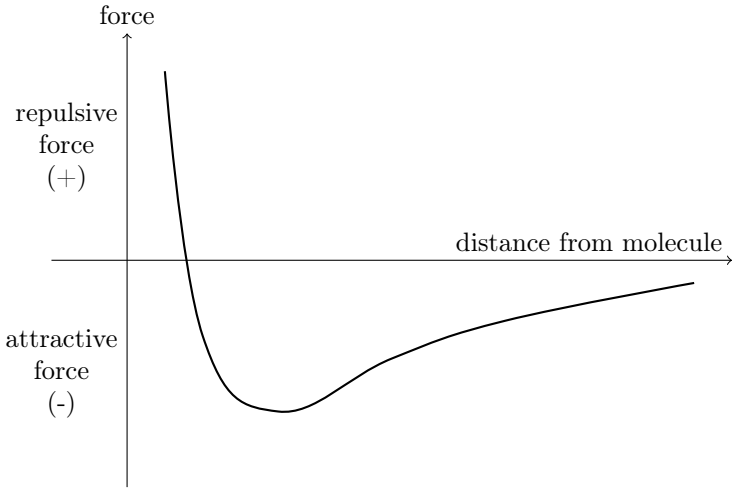

Figure 2.1: Qualitative representation of the variation of the intermolecular force of a single molecule with distance on basis of [5]

proximately more than 10 molecular diameters apart, the magnitude of the intermolecular forces are very small and can be neglected [5], referred to as idealized gas behavior.

2.1.1.1 Idealized gas models

For many problems in aerodynamics the assumption of idealized gas behavior is very reasonable and simplifies the mathematical treatment of the Navier-Stokes equations enormously. In general, there are two levels of idealization: a thermally and calorically perfect gas, which is in this work referred to as an ideal gas, and a thermally perfect but calorically imperfect gas, termed thermally perfect gas, here. The ideal gas assumption is commonly relied upon in the derivation and validation of numerical schemes.

A thermally perfect gas is defined as a gas having no forces of intermolecular attraction. This assumption is justified especially at pressures considerably lower than the critical pressure and at temperatures above the critical temperature, where the molecular motion and, therefore, the macroscopic properties of the system are not affected by intermolecular forces. The thermal equation of state of a thermally perfect gas represents a generalization

of Boyle's law, Charles's law and Avogadro's law

$$p = \varrho R_u / MT, \tag{2.16}$$

containing the universal gas constant $R_u = 8.3143\,\mathrm{kJ\,mol^{-1}\,K^{-1}}$. This equation can be derived from first principles using the concepts of either statistical mechanics or kinetic theory. For a thermally perfect gas, it can be demonstrated mathematically (see [132]) and experimentally (Joule's law) that the caloric equation of state for the internal energy is a function of the temperature only

$$e = e\,(T)\,. \tag{2.17}$$

The same holds for the enthalpy, formally defined as

$$h \coloneqq e + p/\varrho, \tag{2.18}$$

i.e.,

$$h = h\,(T)\,. \tag{2.19}$$

With the definitions of heat capacity at constant volume

$$c_v \coloneqq \left(\frac{\partial e}{\partial T}\right)_v \tag{2.20}$$

and heat capacity at constant pressure

$$c_p \coloneqq \left(\frac{\partial h}{\partial T}\right)_p, \tag{2.21}$$

related to the gas constant by

$$c_v = c_p - R_u/M, \tag{2.22}$$

the differential changes in internal energy and enthalpy of a thermally perfect gas can be expressed as

$$\mathrm{d}e = c_v\,(T)\,\mathrm{d}T \tag{2.23}$$

$$\mathrm{d}h = c_p\,(T)\,\mathrm{d}T\,. \tag{2.24}$$

Accurate analytical expressions for the heat capacities, based on direct measurements or gas kinetic calculations, are, e.g., available as the so-called NASA polynomials [16, 106] and used in this work as basis for real gas computations with the Peng-Robinson EoS.

A further simplification can be achieved by assuming constant heat capacities, irrespective of the temperature, reducing the caloric equation of state for the internal energy to

$$e = c_v T,\ c_v = \text{const.} \tag{2.25}$$

The gas, for which thermally perfect (2.16) and calorically perfect (2.25) equations of state hold, is referred to as the ideal gas model in this work. Introduction of the heat capacity ratio

$$\gamma \coloneqq c_p / c_v, \tag{2.26}$$

allows combining eqs. (2.16) and (2.25) to the single caloric equation of state for an ideal gas

$$p = (\gamma - 1)\, \varrho e. \tag{2.27}$$

As previously mentioned, this ideal gas model is very convenient for mathematical examination of the Navier-Stokes equations and commonly used in derivation and validation of new numerical solution methods. However, for the considered non-ideal fluid flows this conventionally applied assumption is not applicable and real gas behavior has to be accounted for.

2.1.1.2 Real gas models

Whenever intermolecular forces influence the macroscopic properties of a fluid flow, the perfect-gas equation of state is no longer valid. This is the case at high pressures and/or low temperatures (compared to their critical values), when the molecules are packed closely together and move slowly with consequent low inertia. To quantify the deviation from the thermally perfect equation of state (2.16) and its underlying assumptions, it is convenient to introduce the compressibility factor

$$Z \coloneqq \frac{p}{\varrho R_u / M T}, \tag{2.28}$$

which is $Z \equiv 1$ for a thermally perfect or ideal gas. For real gases, Z can be greater or less than unity and the deviation from unity quantifies the deviation from thermally perfect gas behavior. Based on reduced pressure

$$p_r \coloneqq p / p_c \tag{2.29}$$

and reduced temperature

$$T_r \coloneqq T / T_c, \tag{2.30}$$

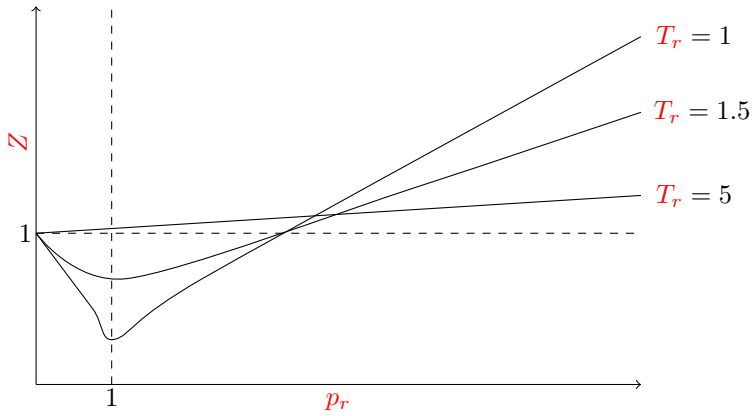

Figure 2.2: Outline of the generalized compressibility chart

with the critical pressure p_c and critical temperature T_c, generalized compressibility charts can be created from experimental data of several substances, as outlined in fig. 2.2. I.e., this scaling allows many substances to be represented graphically in generalized form [130], where strong deviations from thermally perfect gas behavior for all substances arise close to the critical point ($p_r \approx T_r \approx 1$) and large values of p_r in combination with small values of T_r. Here, real gas equations of state must be employed, of which there are many versions. A detailed overview is given in [130]. Generally, real gas EoS can be categorized into virial, analytical and purely empirical EoS.

Virial equations of state rely on a polynomial series expansion of the compressibility factor (2.28), which are for pure substances only functions of the temperature

$$Z = 1 + \frac{B(T)}{v} + \frac{C(T)}{v^2} + \frac{D(T)}{v^3} + \dots \tag{2.31}$$

and can be deduced form molecular theory. Equation (2.31) is typically truncated at the second or third order term and is then able to represent modest deviations from ideal gas behavior, but not liquid properties [130]. Alternative EoS forms are more accurate, especially for dense fluids [130].

Most prominent among analytical EoS are cubic equations of state of which a very detailed overview is given in [130]. The basic idea of cubic EoS is the theorem of corresponding states that there should exist an equation of state valid for all substances. This principle is also manifested in fig. 2.2. The simplest cubic EoS dates back to van der Waals [187], incorporating correction factors for pressure and volume with respect to the thermally perfect gas

assumption. Between the multiple cubic EoS, there appears to be no obvious choice [130], as all analytic models show deviations in the critical region. Away from the critical point however, cubic EoS represent a good compromise between accuracy and computational speed. Another big advantage is their straightforward extension to real gas mixtures based on mixing rules, which is also made use of in this work. Especially the cubic EoS formulations of Soave-Redlich-Kwong [166] and Peng-Robinson [124] are used for real gas simulations in industry and academic applications [3]. Near the critical point, the latter exhibits slightly higher accuracy, rendering it better suited for supercritical simulations [3]. Hence, the Peng-Robinson EoS with an appropriate mixing rule is implemented and used in this work for the computation of a real gas mixture. Its application to an ORC turbine is presented in chapter 5.

Strictly empirical equations of state are determined by mathematically correlated measurements and embodied in equations only valid for the considered substance within the measured phase space. Thus, the empirically determined coefficients do not physically consider the intermolecular forces or the molecular structure but are based on a great number of measurements to obtain high accuracy. In this work, multi-parameter equations of state are used formulated in terms of the dimensionless Helmholtz energy

$$\alpha := a\left(T, \varrho\right) / (RT)\,, \tag{2.32}$$

which is split into an ideal and a residual part

$$\alpha\left(1/T_r, \varrho_r\right) = \alpha^0\left(1/T_r, \varrho_r\right) + \alpha^r\left(1/T_r \varrho_r\right)\,, \tag{2.33}$$

as functions of inverse reduced temperature T_r and reduced density

$$\varrho_r := \varrho/\varrho_c. \tag{2.34}$$

Since the Helmholtz energy as a function of density and temperature represents a fundamental EoS, all other thermodynamic properties can be obtained as simple combinations of its partial derivatives, see, e.g., [180]. Final formulations of eq. (2.33) typically contain large numbers of parameters whose values are obtained by regression on experimental data for many properties over wide ranges of conditions [130]. This fact, on one hand, renders multi-parameter EoS often times the benchmark description of a pure substance with an accuracy that probably exceeds that of the underlying measurements [130], provided sufficient experimental data exist. One example is the Span-Wagner formulation for CO_2 [168], which is implemented and used in this work. A large collection of multi-parameter EoS is also contained in the NIST REFPROP [94] framework; an interface to this library is also implemented and used, e.g., for validation purposes. On the other hand, this

accuracy comes at very high computational costs connected with the evaluation of a vast number of complicated parameters, which renders the use of multi-parameter EoS unfeasible in the computation of technical applications.

The only viable option to include the accuracy of multi-parameter EoS in demanding computations is the use of tabulation techniques, first published in [41]. The basic idea is to precompute appropriate values employing an underlying EoS for storage in a lookup table. During the simulation, values are interpolated from this precomputed table instead of a costly evaluation of the EoS. This reduces the computational effort significantly, while maintaining high accuracy, provided appropriate table resolutions and interpolation techniques are employed. Furthermore, such tabulation methods allow for a universal interface to arbitrarily complicated and formulated underlying EoS. An optimal tabulation method provides highly accurate and consistent thermodynamic data, with low storage requirements and a fast lookup. In this work, the spline based table lookup method [87, 89] (SBTL) is used for H_2O and CO_2 computations. A version for humid air real gas mixtures is used in [76]. This method employs a bi-quadratic spline interpolation on structured grids. More details on the SBTL method are also given in section 2.3.2. Unstructured grid based techniques are also possible and published in the literature [24, 42, 138, 150, 204].

In order to prevent an iteration process, the governing equations, introduced in section 2.1, require an EoS formulation in the independent state variables density and internal energy (ϱ, e), as these are the only state variables, which can be directly computed from the conservative variables, see eq. (2.8) and eq. (2.9). Therefore, the SBTL tabulation is formulated in terms of (ϱ, e). Multi-parameter EoS and Peng-Robinson EoS are, however, formulated in (ϱ, T), necessitating an iteration process. Here, the Newton–Raphson method is employed to find the roots of

$$f(T) := e - e(\varrho, T)\Big|_{\varrho}, \tag{2.35}$$

with the derivative

$$\mathrm{d}f/\mathrm{d}T = -c_v(\varrho, T)\Big|_{\varrho}. \tag{2.36}$$

Furthermore, boundary conditions, flux inversion and initialization process require additionally the computation from (ϱ, p), (T, p), (h, s) and (p, s). The derivation of the necessary derivatives for the iteration process analogously to eq. (2.35) and eq. (2.36) is very involved and not shown here for brevity. Useful references in this context are [146] for the Peng-Robinson EoS and [180] for the multi-parameter EoS. State equations for condensing wet steam computations are introduced in section 2.3.2.

2.1.2 Transport properties

In addition to equations of state, the transport properties viscosity and thermal conductivity must be provided for the working fluid in dependence of the thermodynamic state. The simplest expression for the viscosity, aside from a constant viscosity assumption, is following power-law relation

$$\mu\left(T\right) = \mu\left(T_{\mathrm{ref}}\right)\left(\frac{T}{T_{\mathrm{ref}}}\right)^{n}, \tag{2.37}$$

where the viscosity must be specified at the reference temperature T_{ref}. A more sophisticated approach is the use of Sutherland's formula [175]

$$\mu\left(T\right) = \mu\left(T_{\mathrm{ref}}\right)\left(\frac{T}{T_{\mathrm{ref}}}\right)^{3/2}\frac{T_{\mathrm{ref}}+S}{T+S}, \tag{2.38}$$

with the Sutherland temperature S. It is based on the kinetic theory of an ideal gas with an idealized intermolecular force potential and is still commonly used with most often fairly accurate results with an error less than a few percent over a wide range of temperatures. For air, the viscosity at $T_{\mathrm{ref}} = 273.15\,\mathrm{K}$ is $\mu\left(T_{\mathrm{ref}}\right) = 1.716 \times 10^{-5}\,\mathrm{kg\,m^{-1}\,s^{-1}}$, with a Sutherland temperature $S = 110.4\,\mathrm{K}$. Given the viscosity, the thermal conductivity for an ideal gas can be computed specifying a constant Prandtl number

$$\lambda\left(T\right) = c_p\left(T\right)\mu\left(T\right)/Pr. \tag{2.39}$$

Analogously to the discussion in section 2.1.1.2, there exists a vast number of different options to compute the transport properties of a real gas; an overview is given in [130]. For multi-parameter equations of state, corresponding formulations for viscosity and thermal conductivity are used, e.g., for CO_2 the formulations of [39] for viscosity and of [156] for thermal conductivity. The most accurate formulations for other substances are, e.g., provided in REFPROP. For the real gas mixture computation presented in chapter 5, the low-pressure gas mixture variants of the corresponding state method of Chung et al. [19] are used for the computation of the transport properties, as presented in [130]. This method allows for a one-fluid treatment, analogously to the thermodynamic properties computed by the Peng-Robinson EoS.

At this point, the description of thermodynamically generalized single-phase gas flows is complete, at least for non-turbulent flows. However, for the rotating sections of turbomachines, it is very convenient to reformulate the governing equations in the rotating frame of reference, as described in the following.

2.1.3 Steadily rotating frame of reference

The complexity of the mathematical description of the Navier-Stokes equations in steadily rotating domains of turbomachinery applications can be strongly reduced, formulating the Navier-Stokes equations relative to the rotating rather than the absolute (inertial) frame of reference. Employing a formulation in the relative system renders the problem, which is unsteady in the stationary (inertial) frame, steady with respect to the rotating frame and allows obtaining steady-state solutions. Conducting unsteady computations in the relative frame allows accounting only for unsteadiness due to a natural fluid instability, like, e.g., vortex shedding from a rotor blade, rather than relative motion with respect to an inertial system.

The Navier-Stokes equations in the relative frame of reference can be formulated in two different ways, in terms of the relative or absolute velocities. In this work, the relative velocity formulation is solved and introduced in the following. Absolute velocity $\underline{u}$, relative to the inertial system, and relative velocity $\underline{u}_{\mathrm{rel}}$, relative to the rotating frame of reference, are related by

$$\underline{u} = \underline{u}_{\mathrm{rel}} + \underline{u}_{\mathrm{e}}, \tag{2.40}$$

where the entrainment velocity of the steadily rotating system is given by

$$\underline{u}_{\mathrm{e}} = \omega \times r, \tag{2.41}$$

with the constant angular velocity ω around a given constant axis.

The continuity equation remains unchanged, since mass balance is invariant to system rotation. Forces of inertia must, however, be included in momentum and energy equation. The source term of the momentum equation must account for effects due to Coriolis forces

$$\underline{f}_{\mathrm{coriolis}} = -2\left(\omega \times \underline{u}_{\mathrm{rel}}\right) \tag{2.42}$$

and centrifugal forces

$$\underline{f}_{\mathrm{centrifugal}} = -\omega \times \left(\omega \times r\right). \tag{2.43}$$

In the energy equation, only the work of the centrifugal forces must be added, since the Coriolis forces do not contribute. Thus, eq. (2.1) is now formulated in terms of the conservative variables

$$\underline{w} := \left(\varrho, \varrho\underline{u}_{\mathrm{rel}}, \varrho E_{\mathrm{rel}}\right), \tag{2.44}$$

with the relative total internal energy

$$E_{\mathrm{rel}} := e + \underline{u}_{\mathrm{rel}} \cdot \underline{u}_{\mathrm{rel}}/2 - \underline{u}_{\mathrm{e}} \cdot \underline{u}_{\mathrm{e}}/2. \tag{2.45}$$

The advective fluxes are given by

$$\underline{\underline{F}}^{a} \coloneqq \left(\varrho \underline{u}_{\mathrm{rel}}, \varrho \underline{u}_{\mathrm{rel}} \otimes \underline{u}_{\mathrm{rel}} + p\underline{\underline{I}}, \varrho \underline{u}_{\mathrm{rel}} \left(E_{\mathrm{rel}} + p/\varrho\right)\right), \tag{2.46}$$

the diffusive fluxes by

$$\underline{\underline{F}}^{d} \coloneqq \left(\underline{0}, \underline{\underline{\tau}}, \underline{\underline{\tau}} \cdot \underline{u}_{\mathrm{rel}} - \underline{q}\right), \tag{2.47}$$

with the altered viscous stress tensor

$$\underline{\underline{\tau}} \coloneqq \mu\left(\varrho, e\right)\left(\mathrm{grad}\, \underline{u}_{\mathrm{rel}} + \left(\mathrm{grad}\, \underline{u}_{\mathrm{rel}}\right)^{\mathsf{T}} - 2/3\ \mathrm{div} \underline{u}_{\mathrm{rel}}\, \underline{\underline{I}}\right). \tag{2.48}$$

The following source term has to be added to the sources $\underline{s}$ of the governing equations (2.1)

$$\underline{s}_{\mathrm{rel}} \coloneqq \left(0, \underline{f}_{\mathrm{coriolis}} + \underline{f}_{\mathrm{centrifugal}}, 0\right). \tag{2.49}$$

In the following, all equations and solution schemes are only presented in the absolute frame of reference for brevity. The respective formulation in the relative frame is straightforward to derive based on this section. The treatment of turbulence is discussed next.

2.2 Turbulent single-phase gas flows

As mentioned in the introduction to this chapter, the Navier-Stokes equations form a system of nonlinear PDEs, which has major implications on the whole physics of fluid motion. This nonlinearity is dominantly caused by the advective term of the momentum equation, which leads to the appearance of turbulence, characterized by statistical (chaotic) fluctuations of all flow quantities. For the considered turbomachinery flows in propulsion and power, turbulence often dynamically interacts with shock waves and other discontinuities, which are result of the nonlinearity of the products of density and velocity in absence of other mechanisms like condensation. This poses a considerable challenge for derivation, design and execution of numerical models of fluid flows.

Laminar flows can directly be solved based on the governing equations introduced until now. However, once a critical Reynolds number

$$Re = \varrho \mathcal{U} \mathcal{L} / \mu, \tag{2.50}$$

with representative velocity $\mathcal{U}$ and length $\mathcal{L}$ scales, is exceeded, a turbulent flow is encountered, which is the case for almost all technically relevant flow configurations. Turbulent flows are characterized by turbulent fluctuations

over a wide range of length and time scales, as indicated in fig. 2.3, which are dependent on the Reynolds number. The size of the smallest turbulent eddies decreases proportional to $\sim Re^{3/4}$, as described by the Kolmogorov length scale. The total number of numerical operation required for a complete resolution of the spectrum can be estimated to scale with $\propto Re^3$ [67]; the number of time steps scales with $\propto Re^{3/4}$, the number of required grid points with $\propto Re^{9/4}$ in three dimensions. As Reynolds numbers in technically relevant configurations are typically of the order 10^5 to 10^7, a complete resolution of the turbulent spectrum at these Reynolds numbers is impossible, also in the long term.

I.e., the complete resolution of the turbulent spectrum, termed DNS, is only possible at reduced Reynolds numbers and is employed as a "numerical experiment" to better understand the fundamental mechanisms of turbulence and to improve and calibrate approximate models to the description of turbulence, mainly LES and RANS. These approximations are needed for the computation of turbulent high Reynolds number flows, where the basic idea is to model the entire or at least certain parts of the turbulent spectrum and only account approximately for the influence on the resolved part of the flow, as also indicated in fig. 2.3. A reduction in complexity, appropriate to retaining the basic three-dimensional unsteady nature of the Navier-Stokes equations, can be achieved performing a spatially filtering, introducing a certain cutoff in size below which the turbulent fluctuations are not resolved, referred to as LES. I.e., the larger turbulent scales are completely resolved, with the smaller scales being modeled. The RANS approach does not resolve the turbulent fluctuations and aims at calculating mean flow quantities, only. Here, the whole turbulent spectrum is modeled by turbulence models. Application of this approach to unsteady flows is termed URANS. Overall, this approach is currently the most widely applied approximation for turbulent fluid flows. More details on turbulent flows is found, e.g., in [131, 198].

All three methods, DNS, LES and RANS/URANS, are employed in this work. The modeling approaches are introduced in the following with special reference to real gas flows. It must also be noted that scale resolving computations, like DNS and LES, require advanced computational methods, especially when shock waves or other discontinuities are present in the domain. These are presented in the next chapter.

2.2.1 LES

The basic idea of LES is to reduce the computational effort of turbulent flows by removing small scale turbulent structures through filtering of the Navier-Stokes equations. The turbulent scales are separated using a scale high-pass

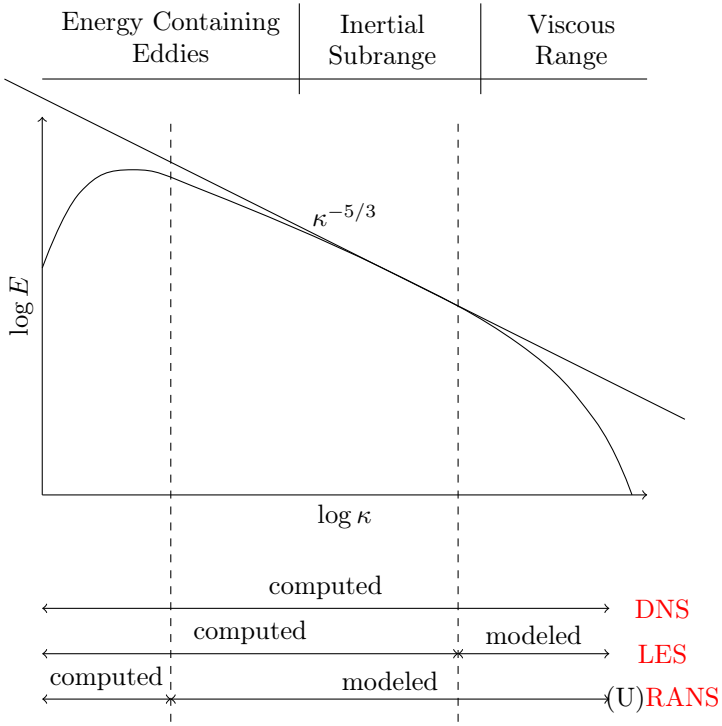

Figure 2.3: Energy spectrum of turbulence with indication of the range of application of the different turbulence modeling approaches

filter, which is also a low-pass filter in frequency [46], retaining the basic three-dimensional unsteady nature of the Navier-Stokes equations. The influence of the unresolved scales below the introduced cutoff associated with the filtering on the resolved scales is only modeled, leading to a dramatic reduction in computational effort compared to DNS.

The filtering in physical space can mathematically be expressed as a convolution product [46, 48, 129], where the resolved part of a space-time variable $\phi\left(\underline{x}, t\right)$ is given by

$$\bar{\phi}\left(\underline{x}, t\right) := \int_{-\infty}^{\infty} G\left(\underline{x} - \underline{x}', t - t'; \Delta\right) \phi\left(\underline{x}', t'\right) \mathrm{d}\underline{x}' \, \mathrm{d}t' \,. \tag{2.51}$$

The filtering is characterized by the kernel G and associated with a cutoff in space Δ and implicitly with a cutoff in time [46]. The filter can be explicitly

specified; however, in practice the filter is given implicitly by numerical grid and solution scheme [46, 151]. To prevent additional terms requiring closure, it is common for compressible flows to introduce Favre-filtering: weighting certain filtered variables by the density

$$\tilde{\phi}\left(\underline{x}, t\right) \coloneqq \frac{1}{\bar{\varrho}} \int_{-\infty}^{\infty} G\left(\underline{x} - \underline{x}', t - t'; \Delta\right) \varrho\phi\left(\underline{x}', t'\right) \mathrm{d}\underline{x}' \, \mathrm{d}t' \tag{2.52}$$

eliminates correlations with the unresolved subgrid scale density from the filtered equations, without removing their effect on the turbulence [198]. Thus, the resolved low frequency part of a Favre-filtered quantity is given by

$$\tilde{\phi} = \overline{\varrho\phi} / \bar{\varrho} \tag{2.53}$$

and the unresolved, high frequency part follows as

$$\phi'' \coloneqq \phi - \tilde{\phi}. \tag{2.54}$$

Applying the filtering (2.51) to the governing equations described in section 2.1 and assuming that the filtering operator commutes with differentiation (see, e.g., [45, 54]) yields eq. (2.1) formulated now in terms of the filtered conservative variables

$$\underline{w}\left(\underline{x}, t\right) = \left(\bar{\varrho}, \bar{\varrho}\tilde{\underline{u}}, \bar{\varrho}\tilde{E}\right), \tag{2.55}$$

where the filtered total internal energy is given by

$$\tilde{E} \coloneqq \tilde{e} + \frac{\tilde{\underline{u}} \cdot \tilde{\underline{u}}}{2} + \frac{\mathrm{tr}\left(\underline{\tau}^{\mathrm{sgs}}\right)}{2\,\bar{\varrho}}. \tag{2.56}$$

The filtering leads to additional terms, combined in an additional subgrid scale (SGS) flux

$$\underline{\underline{F}} = \underline{\underline{F}}^{a} - \underline{\underline{F}}^{d} + \underline{\underline{F}}^{\mathrm{sgs}}, \tag{2.57}$$

where the individual fluxes are given by

$$\underline{\underline{F}}^{a}\left(\underline{w}\right) \coloneqq \left(\bar{\varrho}\tilde{\underline{u}}, \bar{\varrho}\tilde{\underline{u}} \otimes \tilde{\underline{u}} + p\left(\bar{\varrho}, \tilde{e}\right) \underline{\underline{I}}, \bar{\varrho}\tilde{\underline{u}}\left(\tilde{E} + p\left(\bar{\varrho}, \tilde{e}\right) / \bar{\varrho}\right)\right) \tag{2.58}$$

$$\underline{\underline{F}}^{d}\left(\underline{w}\right) \coloneqq \left(\underline{0}, \check{\underline{\tau}}\left(\underline{w}\right), \check{\underline{\tau}}\left(\underline{w}\right) \cdot \tilde{\underline{u}} - \check{q}\left(\underline{w}\right)\right) \tag{2.59}$$

$$\underline{\underline{F}}^{\mathrm{sgs}}\left(\underline{w}\right) \coloneqq \begin{pmatrix} 0 \\ \underline{\tau}^{\mathrm{sgs}} + \left(\overline{p\left(\varrho, e\right)} - p\left(\bar{\varrho}, \tilde{e}\right)\right) \underline{\underline{I}} - \left(\bar{\underline{\tau}} - \check{\underline{\tau}}\right) \\ \underline{q}^{\mathrm{sgs}} + \underline{D}_t + \underline{D}_v + \left(\bar{\underline{q}} - \check{\underline{q}}\right) \end{pmatrix}^{\mathsf{T}}. \tag{2.60}$$

The additional SGS terms $\underline{\underline{F}}^{\text{sgs}}$ comprise, in addition to nonlinear terms occurring in the viscous terms, the heat fluxes and the pressure, SGS stress tensor, SGS heat flux, turbulent and viscous diffusion

$$\underline{\underline{\tau}}^{\text{sgs}} = \bar{\varrho}\left(\widetilde{\underline{u}\otimes\underline{u}} - \tilde{\underline{u}}\otimes\tilde{\underline{u}}\right) \tag{2.61}$$

$$\underline{q}^{\text{sgs}} = \bar{\varrho}\left(\widetilde{\underline{u}h} - \tilde{\underline{u}}\tilde{h}\right) \tag{2.62}$$

$$\underline{D}_t = \frac{1}{2}\left(\bar{\varrho}\widetilde{\underline{u}\underline{u}\cdot\underline{u}} - \bar{\varrho}\tilde{\underline{u}}\tilde{\underline{u}}\cdot\tilde{\underline{u}} - \tilde{\underline{u}}\,\mathrm{tr}\left(\underline{\underline{\tau}}^{\text{sgs}}\right)\right) \tag{2.63}$$

$$\underline{D}_v = \overline{\underline{\underline{\tau}}\cdot\underline{u}} - \check{\underline{\underline{\tau}}}\cdot\tilde{\underline{u}}. \tag{2.64}$$

Computable stress tensor and heat flux are defined as

$$\check{\underline{\underline{\tau}}} \coloneqq \mu\left(\bar{\varrho},\tilde{e}\right)\left(\mathrm{grad}\,\tilde{\underline{u}} + \left(\mathrm{grad}\,\tilde{\underline{u}}\right)^{\mathsf{T}} - 2/3\ \mathrm{div}\tilde{\underline{u}}\ \underline{\underline{I}}\right) \tag{2.65}$$

$$\check{\underline{q}} \coloneqq -\lambda\left(\bar{\varrho},\tilde{e}\right)\mathrm{grad}\,T\left(\bar{\varrho},\tilde{e}\right). \tag{2.66}$$

The additional SGS terms (2.60) require closure and the current modeling standard as given, e.g., in [46] is adopted in this work as follows: The deviatoric part of the SGS stress tensor is modeled based on the Boussinesq hypothesis

$$\underline{\underline{\tau}}^{\text{sgs}} - \frac{1}{3}\mathrm{tr}\left(\underline{\underline{\tau}}^{\text{sgs}}\right)\underline{\underline{I}} \simeq \mu^{\text{sgs}}\left(\mathrm{grad}\,\tilde{\underline{u}} + \left(\mathrm{grad}\,\tilde{\underline{u}}\right)^{\mathsf{T}} - \frac{2}{3}\mathrm{div}\tilde{\underline{u}}\ \underline{\underline{I}}\right), \tag{2.67}$$

where the SGS viscosity μ^{sgs} is given by either the classic Smagorinski model [165] with the standard constant $C_s = 0.18$ or the Wall-Adapting Local Eddy-Viscosity (WALE) model [119] with the constant $C_w = 0.325$. The isotropic part of the SGS stress tensor is neglected

$$\mathrm{tr}\left(\underline{\underline{\tau}}^{\text{sgs}}\right) \simeq 0, \tag{2.68}$$

justified by the assumption that it assumes large values in areas of high compression/dilatation, where the underlying numerical scheme introduces a large amount of numerical dissipation probably overwhelming the effect of a model [46]. This implies

$$\underline{\underline{\tau}}^{\text{sgs}} \simeq \mu^{\text{sgs}}\left(\mathrm{grad}\,\tilde{\underline{u}} + \left(\mathrm{grad}\,\tilde{\underline{u}}\right)^{\mathsf{T}} - \frac{2}{3}\mathrm{div}\tilde{\underline{u}}\ \underline{\underline{I}}\right) \tag{2.69}$$

and

$$\tilde{E} \simeq \tilde{e} + \frac{\tilde{\underline{u}}\cdot\tilde{\underline{u}}}{2}. \tag{2.70}$$

The SGS heat flux is modeled based on a constant Prandtl number

$$\underline{q}^{\mathrm{sgs}} \simeq -\lambda^{\mathrm{sgs}} \operatorname{grad} T\left(\bar{\varrho}, \tilde{e}\right), \tag{2.71}$$

with the SGS conductivity

$$\lambda^{\mathrm{sgs}} = \mu^{\mathrm{sgs}} c_p\left(\bar{\varrho}, \tilde{e}\right) / Pr^{\mathrm{sgs}} \tag{2.72}$$

where Pr^{sgs} is in interval $[0.3, 0.9]$ [46].

The turbulent diffusion is modeled analogously to RANS (see eq. (2.98))

$$\underline{D}_t \simeq \underline{\tau}^{\mathrm{sgs}} \cdot \tilde{\underline{u}}. \tag{2.73}$$

As common practice [46], the non-linear terms occurring in the viscous terms and in the heat fluxes are neglected

$$\bar{\underline{\tau}} - \check{\underline{\tau}} \simeq 0 \tag{2.74}$$

$$\bar{\underline{q}} - \check{\underline{q}} \simeq 0, \tag{2.75}$$

as is the viscous diffusion

$$\underline{D}_v \simeq \underline{0}. \tag{2.76}$$

The term describing the effects of SGS fluctuations on the generalized state relation is only immanent to real gas flows and is neglected at present time

$$\overline{p\left(\varrho, e\right)} - p\left(\bar{\varrho}, \tilde{e}\right) \simeq 0, \tag{2.77}$$

where this relation holds exactly for an ideal gas, for which

$$\overline{p\left(\varrho, e\right)} = p\left(\bar{\varrho}, \tilde{e}\right) = \left(\gamma - 1\right) \bar{\varrho} \tilde{e}. \tag{2.78}$$

To the author's best knowledge, the effect of this assumption has not yet been thoroughly investigated and the development of a real gas DNS code, also presented in this work, is aimed to address this research need in the future. In fact, very little is also known about the other previously mentioned nonlinear terms [46], especially in compressible real gas flows.

With this modeling assumptions, the remaining SGS fluxes can be merged into the diffusive fluxes, reducing eq. (2.57) to

$$\underline{\underline{F}} = \underline{\underline{F}}^a - \underline{\underline{F}}^d \tag{2.79}$$

where the diffusive flux

$$\underline{\underline{F}}^d\left(\underline{w}\right) \coloneqq \left(\underline{0}, \underline{\tau}^*\left(\underline{w}\right), \underline{\tau}^*\left(\underline{w}\right) \cdot \tilde{\underline{u}} - \underline{q}^*\left(\underline{w}\right)\right) \tag{2.80}$$

contains effective shear stress tensor and effective heat flux vector

$$\underline{\tau}^* := \left(\mu\left(\bar{\varrho},\tilde{e}\right)+\mu^{\mathrm{sgs}}\right)\left(\operatorname{grad}\tilde{\underline{u}}+\left(\operatorname{grad}\tilde{\underline{u}}\right)^{\mathsf{T}}-2/3\ \operatorname{div}\tilde{\underline{u}}\ \underline{\underline{I}}\right) \tag{2.81}$$

$$\underline{q}^* := -\left(\lambda+\lambda^{\mathrm{sgs}}\right)\left(\bar{\varrho},\tilde{e}\right)\operatorname{grad}T\left(\bar{\varrho},\tilde{e}\right). \tag{2.82}$$

Reynolds-averaging the Navier-Stokes equations formally leads to similar terms, which are, however, of quite different nature. The resulting RANS equations are introduced in the following.

2.2.2 RANS

A much higher reduction of effort in the computation of turbulent flows compared to LES is achieved by solving the RANS equations, which do not resolve any turbulent fluctuations and aim at calculating time mean flow quantities only. Consequently, the whole turbulent spectrum has to be modeled by so-called turbulence models to account for their influence on the mean flow. Its comparably low expense renders this approach the most widely applied approximation for turbulent fluid flows in practice.

For stationary turbulence, the mean flow quantity of an instantaneous flow variable $\phi\left(\underline{x},t\right)$ is given by its time average

$$\bar{\phi}\left(t\right) := \lim_{T\to\infty}\int_{t}^{t+T}\phi\left(\underline{x},t'\right)\mathrm{d}t'. \tag{2.83}$$

Other formal definitions of Reynolds-averages are also possible [131, 198], see also eq. (2.104). This temporal averaging can be seen as a special case of space-time filtering, eq. (2.51), for which the idempotence property holds [48]. Therefore, applying Reynolds-averaging to the Navier-Stokes equations yields similar formal relations as in case of filtering, which can, however, be further simplified due to the idempotence property of time averaging and the quite different physical nature must always be adhered to. For compressible flows it is convenient to introduce the Favre-average

$$\tilde{\phi}\left(t\right) := \frac{1}{\bar{\varrho}}\lim_{T\to\infty}\int_{t}^{t+T}\varrho\left(\underline{x},t'\right)\phi\left(\underline{x},t'\right)\mathrm{d}t', \tag{2.84}$$

which eliminates—analogously to (2.52) for the filtering—the density fluctuations from the Reynolds-averaged equations, but does not remove the effect the density fluctuations have on the turbulence [198]. For Favre-averaged flow

quantities, the same formal notation as in eq. (2.53) is adapted, the fluctuating part is then formally given by eq. (2.54).

Applying Reynolds-averaging to the governing equations described in section 2.1 yields eq. (2.1) formulated now in terms of the Reynolds-averaged conservative variables, formally given by (2.55) with the averaged total internal energy

$$\tilde{E} \coloneqq \tilde{e} + \frac{\tilde{\underline{u}} \cdot \tilde{\underline{u}}}{2} + \frac{\mathrm{tr}\left(\underline{\underline{\tau}}^t\right)}{2\,\bar{\varrho}} \tag{2.85}$$

and an additional turbulent flux

$$\underline{\underline{F}} = \underline{\underline{F}}^a - \underline{\underline{F}}^d + \underline{\underline{F}}^t, \tag{2.86}$$

with the other fluxes formally given by eq. (2.58) and eq. (2.59), respectively. The turbulent fluxes are formally similar to the additional fluxes due to filtering (2.60)

$$\underline{\underline{F}}^t\left(\underline{w}\right) \coloneqq \begin{pmatrix} 0 \\ \underline{\underline{\tau}}^t + \left(\overline{p\left(\varrho, e\right)} - p\left(\bar{\varrho}, \tilde{e}\right)\right) \underline{\underline{I}} - \left(\underline{\underline{\bar{\tau}}} - \underline{\underline{\check{\tau}}}\right) \\ \underline{q}^t + \underline{D}_t + \underline{D}_v + \left(\underline{\bar{q}} - \underline{q}^t\right) \end{pmatrix}^{\mathsf{T}}, \tag{2.87}$$

some contained quantities can, however, be further simplified due to the idempotence property of the Reynolds-averaging operator

$$\underline{\underline{\tau}}^t = \bar{\varrho}\left(\widetilde{\underline{u} \otimes \underline{u}} - \tilde{\underline{u}} \otimes \tilde{\underline{u}}\right) = \bar{\varrho}\widetilde{\underline{u}'' \otimes \underline{u}''} \tag{2.88}$$

$$\underline{q}^t = \bar{\varrho}\left(\widetilde{\underline{u}h} - \tilde{\underline{u}}\tilde{h}\right) = \bar{\varrho}\widetilde{\underline{u}''h''} \tag{2.89}$$

$$\underline{D}_t = \frac{1}{2}\left(\bar{\varrho}\widetilde{\underline{u}\underline{u} \cdot \underline{u}} - \bar{\varrho}\tilde{\underline{u}}\tilde{\underline{u}} \cdot \tilde{\underline{u}} - \tilde{\underline{u}}\,\mathrm{tr}\left(\underline{\underline{\tau}}^t\right)\right) = \tilde{\underline{u}} \cdot \underline{\underline{\tau}}^t + \frac{1}{2}\bar{\varrho}\widetilde{\underline{u}''\underline{u}'' \cdot \underline{u}''} \tag{2.90}$$

$$\underline{D}_v = \overline{\underline{\underline{\tau}} \cdot \underline{u}} - \underline{\underline{\check{\tau}}} \cdot \tilde{\underline{u}} = \left(\underline{\underline{\bar{\tau}}} - \underline{\underline{\check{\tau}}}\right) \cdot \tilde{\underline{u}} + \overline{\underline{\underline{\tau}} \cdot \underline{u}''}. \tag{2.91}$$

In this work, only turbulence model closure based on Boussinesq hypothesis

$$\underline{\underline{\tau}}^t - \frac{1}{3}\mathrm{tr}\left(\underline{\underline{\tau}}^t\right)\underline{\underline{I}} \simeq \mu^t\left(\mathrm{grad}\,\tilde{\underline{u}} + \left(\mathrm{grad}\,\tilde{\underline{u}}\right)^{\mathsf{T}} - \frac{2}{3}\mathrm{div}\tilde{\underline{u}}\,\underline{\underline{I}}\right) \tag{2.92}$$

and Spalart-Allmaras turbulence model [167] (SA) is considered (a comprehensive overview is, e.g., given in [95, 131, 198]). For this one equation model, it is common to neglect the isotropic part of the turbulent stress tensor

$$\mathrm{tr}\left(\underline{\underline{\tau}}^t\right) \simeq 0, \tag{2.93}$$

which is a good approximation for flows with Mach numbers below hypersonic speeds, where $\mathrm{tr}\left(\underline{\underline{\tau}}^t\right) \ll p\left(\bar{\varrho}, \tilde{e}\right)$ in most flows of engineering interest [198]. This implies

$$\underline{\underline{\tau}}^t \simeq \mu^t \left(\mathrm{grad}\, \underline{\tilde{u}} + \left(\mathrm{grad}\, \underline{\tilde{u}}\right)^{\mathsf{T}} - \frac{2}{3} \mathrm{div} \underline{\tilde{u}}\, \underline{\underline{I}} \right) \tag{2.94}$$

and

$$\tilde{E} \simeq \tilde{e} + \frac{\underline{\tilde{u}} \cdot \underline{\tilde{u}}}{2}. \tag{2.95}$$

The turbulent heat flux is modeled based on a constant Prandtl number

$$\underline{q}^t \simeq -\lambda^t \,\mathrm{grad}\, T\left(\bar{\varrho}, \tilde{e}\right), \tag{2.96}$$

with the turbulent conductivity

$$\lambda^t = \mu^t c_p\left(\bar{\varrho}, \tilde{e}\right) / Pr^t, \tag{2.97}$$

where the turbulent Prandtl number is commonly set to $Pr^t = 0.9$.

In the turbulent diffusion term, the turbulent transport of the turbulent kinetic energy is neglected

$$\underline{D}_t \simeq \underline{\tilde{u}} \cdot \underline{\tau}^t, \tag{2.98}$$

as are viscous diffusion and the non-linear terms occurring in the viscous terms and in the heat fluxes

$$\underline{D}_v \simeq 0 \tag{2.99}$$

$$\bar{\underline{\tau}} - \breve{\underline{\tau}} \simeq 0 \tag{2.100}$$

$$\bar{\underline{q}} - \breve{\underline{q}} \simeq 0. \tag{2.101}$$

As in the filtered case, the term describing the effects of turbulent fluctuations on the generalized state relation is only immanent to real gas flows and is neglected analogously to eq. (2.77), which holds exactly only for an ideal gas. To the author's best knowledge, the effect of this assumption has not yet been thoroughly investigated, as in the case of LES closure, and the development of a real gas DNS code in this work is aimed, among other things, to address this research need in the future.

With these modeling assumptions, the turbulent fluxes can be merged into the diffusive fluxes, reducing eq. (2.86) to a formally similar expression to eq. (2.79), with the diffusive flux (2.80). The contained effective shear stress tensor and effective heat flux vector are given by

$$\underline{\underline{\tau}}^* := \left(\mu\left(\bar{\varrho}, \tilde{e}\right) + \mu^t\right) \left(\mathrm{grad}\, \underline{\tilde{u}} + \left(\mathrm{grad}\, \underline{\tilde{u}}\right)^{\mathsf{T}} - 2/3\ \mathrm{div} \underline{\tilde{u}}\, \underline{\underline{I}} \right) \tag{2.102}$$

$$\underline{q}^* := -\left(\lambda + \lambda^t\right)\left(\bar{\varrho}, \tilde{e}\right) \mathrm{grad}\, T\left(\bar{\varrho}, \tilde{e}\right). \tag{2.103}$$

Whenever RANS modeling is adopted to the computation of a time dependent solution, the term URANS has become common [43]. For unsteady flows with some basic frequency, a phase average with a triple decomposition can be introduced [43]. For some flows, the mean flow contains very slow variations with time that are not of turbulent nature and a finite-time temporal average can be used [43, 198]

$$\bar{\phi}\left(\underline{x}, t\right) \coloneqq \frac{1}{T} \int_{t}^{t+T} \phi\left(\underline{x}, t'\right) \mathrm{d}t' \quad \text{where} \quad T_t \ll T \ll T_{\mathrm{mean}}. \tag{2.104}$$

The time scale of the turbulent fluctuations T_t and the time scale of slow mean flow variations of non-turbulent nature T_{mean} must differ by several orders of magnitude, as mean and fluctuating components must not be correlated. Many unsteady flows of engineering interest do not satisfy this condition, which is often referred to as the spectral gap problem, while LES does not suffer from this problem and thus represents a rigorous approach [198].

In the following, the mathematical model is expanded to describe condensing wet steam flows. Both turbulence modeling approaches, RANS and also LES, are adopted to the computation of turbulent wet steam flows; respective results are presented in chapter 4.

2.3 Condensing wet steam flows

During the expansion of pure steam in a steam turbine, condensation in the mean flow does not commence once the saturation line is crossed. With no solid surfaces present in the core of the flow to promote the condensation, a free-energy barrier to form a vast number of extremely small liquid droplets must be overcome. During this process, the steam is in a metastable state and increasingly supersaturated (in terms of pressure or subcooled in terms of temperature) until the energy barrier is transcended. An equilibrium state is subsequently reattained via the formation and growth of liquid droplets. This homogeneous nucleation process is well described in detail in [107, 108]. A state-of-the-art review is given in [6].

To account for the process of non-equilibrium condensation, the governing equations describing a single-phase gas flow, introduced in section 2.1, must be extended. The modeling of turbulent wet steam flows is very involved and is based on different models—describing the condensation process, the resulting second phase and the thermodynamic properties—and their complex interaction, indicated in fig. 2.4. Consequence of this complexity can be regarded the fact that yet no universal wet steam modeling

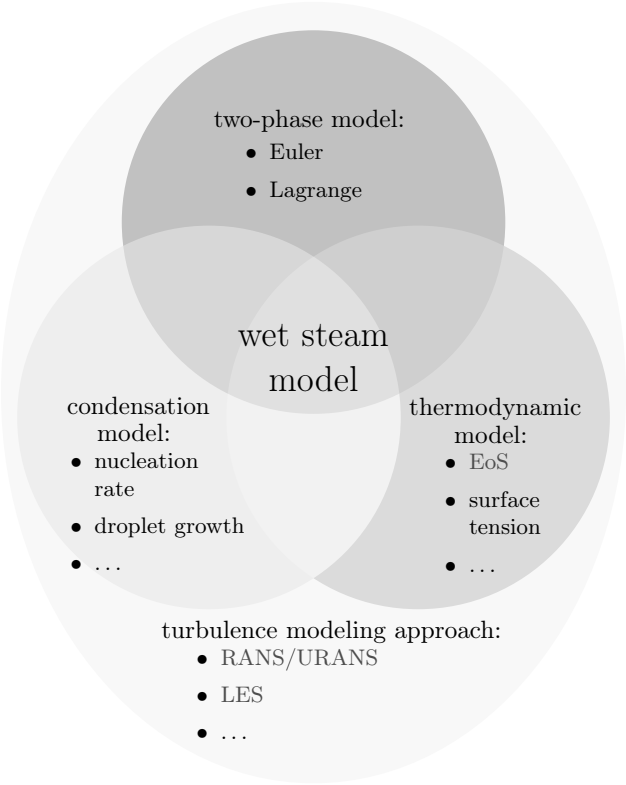

Figure 2.4: Interacting modeling approaches in the description of turbulent wet steam flows (see also [137])

approach has emerged for wet steam flows [171] despite research dating back to as far as the 1880s [63]. Wet steam computations are still associated with significant uncertainty and sufficient accuracy can only be achieved based on thorough calibrations for the considered operating conditions [171]. The overall uncertainty of wet steam modeling results from the uncertainty associated with each submodel.

The condensation modeling in modern wet steam solution methods is based on the classical homogeneous nucleation theory [171], while heterogeneous condensation is most often neglected. Various combinations of adjustments to the description of the nucleation process and the subsequent droplet growth are in use today [6, 171]. The classical nucleation theory is

briefly introduced in the next section. Uncertainties of the thermodynamic model include, among other things, the accurate description of metastable states [159], for which no validation data is available, and the dependence of the surface tension on the embryonic liquid cluster size [171], often incorporated by correcting factors to the planar surface tension of a flat film.

Two-phase treatment is challenging and can be based on Euler-Euler or Euler-Lagrange approaches, connected with different modeling of the droplet size distribution [70, 135, 171]. The classical approach of coupling the Eulerian gas phase calculation with an explicit droplet integration in a Lagrangian frame of reference suffers when scaling to large configurations and an efficient parallelization is hard to achieve [51]. Another disadvantage is high computing times for steady state computations. Therefore, development has begun to focus on Euler-Euler models, where the most general two-fluid model in the context of condensing wet steam calculations is often simplified to source term and even to mixture models [99]. For Euler-Euler models, the simplest approach for modeling the continuous droplet size spectrum is to assume a single, mean droplet size, allowing to approximate the droplet size spectrum based on only two additional transport equations. These monodispersed models provide satisfactory results for straightforward nucleating expansions with a single nucleation event [70], which is the case for all presented test cases in this work. Therefore, only monodispersed models are presented here. More sophisticated, polydispersed approaches to the description of the droplet size spectrum in Euler-Euler methods are possible with quadrature based moment methods like standard method of moments (SMOM) and quadrature method of moments (QMOM), where the SMOM method is already implemented in the solver.

Some aspects of the complex interaction of these three submodels have been investigated [135, 171], however, this does not yet include the effect of turbulence and the modeling approach to it. With this work, the importance of the turbulence modeling approach to the predictability of the wet steam model is shown. This fact is apparent, for example, in classical nozzle test cases, where the state of the boundary layers in the nozzle's throat influences strongly the results [170], though, classical RANS approaches are not capable of accounting for laminar turbulent transition. As is proven by the first scale resolving LES computation in the field of wet steam flows presented in chapter 4, classical RANS and URANS approaches confine the inherently unsteady nature of condensation and its interaction with the turbulent scales due to their mathematical nature, see previous section. This work uses the example of a typical low-pressure turbine flow, where relatively moderate Reynolds numbers and the continuously increasing computational power allow the application of high-fidelity, unsteady, scale-resolving simulation tech-

niques like LES.

In the following, the classical nucleation theory is briefly introduced. Popular EoS and transport property formulations for wet steam computations are presented next. Finally, the wet steam formulations employed in this work are described.

2.3.1 Classical nucleation theory

In this section, the relations to describe the nucleation rate and the growth of the droplet used in this work are summarized. These are based on the classical nucleation theory. An overview of other models and detailed derivations of the expressions can be found, e.g., in [6, 107, 108, 171, 208]. The formation rate of critically sized droplets per unit volume in a supersaturated vapor at pressure p and temperature T_G is obtained by the classical nucleation rate formulation

$$J_c = q_c \frac{\varrho_G{}^2}{\varrho_L} \sqrt{\frac{2\sigma\left(T_G\right)}{\pi {m_M}^3}} \exp\left(-\frac{4\pi\sigma\left(T_G\right)}{3kT_G} {r_c}^2\right), \tag{2.105}$$

with the non-isothermal correction of Kantrowitz [80]

$$J = \frac{J_c}{1+\phi}, \tag{2.106}$$

where

$$\phi = 2\frac{\gamma\left(T_G, p\right) - 1}{\gamma\left(T_G, p\right) + 1} \frac{h_{fg}}{RT_G} \left(\frac{h_{fg}}{RT_G} - \frac{1}{2}\right). \tag{2.107}$$

Source of much controversy is the capillarity approximation [6], i.e., the assumption that the surface tension of a small liquid droplet equals the surface tension of a flat film. Here, accurate values are of paramount importance, as small changes in the surface tension change the nucleation rate in orders of magnitude, as demonstrated in [171]. If not otherwise stated, the planar surface tension of the IAPWS in the version given in [190] is used in this work. The dependence of the surface tension on cluster size and droplet radius, respectively, remains an unresolved issue and Tolman length based approaches as, e.g., introduced in [120], might be worth considering in the future. The condensation coefficient q_c is traditionally defined as the fraction of actually condensing molecules to the total amount of molecules impinging on the droplet. The generally accepted value for water is unity [111], while its value for many other substances is much lower [208]. Therefore,

$$q_c \coloneqq 1 \tag{2.108}$$

is used in this work.

The smallest size of droplets, which are in thermodynamic sense viable and start to grow in the surrounding supersaturated vapor, are described by the Kelvin-Helmholtz critical radius

$$r_c = \frac{2\sigma\left(T_G\right)}{\varrho_L R T_G \ln S}. \tag{2.109}$$

Often, the supersaturation ratio

$$S \coloneqq p/p_s \tag{2.110}$$

is expressed in terms of subcooling

$$\Delta T_s \coloneqq T_s\left(p\right) - T_G, \tag{2.111}$$

where their relation is approximated based on the Clausius-Clapeyron relation

$$\ln S \approx \frac{h_{fg}}{R T_s\left(p\right)} \frac{\Delta T_s}{T_G}. \tag{2.112}$$

From the author's experience, this approximation significantly influences the results despite minimal deviations introduced by eq. (2.112), due to a high sensitivity of the nucleation rate. Thus, the original expression (2.109) is used, if not otherwise stated.

The subsequent droplet growth is computed based on Young's [208] droplet growth equation

$$\frac{\mathrm{d}r}{\mathrm{d}t} = \frac{\lambda\left(T_G, p\right)\left(1 - r_c/r\right)\Delta T_s}{\varrho_L h_{fg} r \left(\left(1 + 2\beta Kn\right)^{-1} + 3.78\left(1 - \nu\right) Kn/Pr\right)}, \tag{2.113}$$

where

$$\nu = \frac{R T_s\left(p\right)}{h_{fg}} \left(\alpha - \frac{1}{2}\frac{2 - q_c}{2q_c}\frac{\gamma\left(T_G, p\right) + 1}{2\,\gamma\left(T_G, p\right)}\frac{c_p\left(T_G, p\right) T_s\left(p\right)}{h_{fg}}\right). \tag{2.114}$$

Equation (2.113) contains two parameters α and β. The growth parameter α stems from a linearization of the ratio of condensation and evaporation coefficients and is a constant to be determined empirically [208]. In [208], $\alpha \coloneqq 9$ is found suitable, however, the best choice is likely to depend on other wet steam model parameters like the EoS [171]. The parameter β comes from the simple Langmuir model to describe the intermediate Knudsen number regime surrounding the condensing droplet with an arbitrarily situated interface at radius $\left(r + \beta\tilde{l}\right)$ separating the application of the free molecular

theory close to the droplet's surface and the continuum theory outside this region and enforced conservation through the interface. The mean free path is computed from the kinetic theory formula

$$\tilde{l} = \frac{1.5\,\mu\,(T_G, p)\,\sqrt{RT_G}}{p}. \tag{2.115}$$

Values used in [171] are in the range 0 to 2. In this work, a value of $\beta := 0$ is used.

The computation of nucleation rate and subsequent droplet growth requires accurate thermodynamic data in the metastable region. Common EoS and transport property formulations used in wet steam computations are introduced in the following section.

2.3.2 Equations of state and transport properties

Due to its technical significance, many specialized equations of state for H_2O have been developed over the years and the development of ever more accurate EoS will remain subject of ongoing research, e.g., driven by the IAPWS. The first EoS for H_2O was presented by Clausius [21] in 1881 and was essentially a generalization of the van der Waals EoS [187]. In 1906 Mollier [114] published his well known steam tables. These were superseded by the VDI-Steam tables [157, 158]. To provide an international standard for industrial use, the International Formulation Committee (IFC) was founded. In 1967 "The 1967 IFC Formulation for Industrial Use (IFC-67)" [75] was published. To achieve a higher accuracy, the phase space was split into several distinct regions with one equation describing each. Simultaneously, a fundamental equation for water was developed by the IAPWS and published in 1995: "The IAPWS Formulation 1995 for the Thermodynamic Properties of Ordinary Water Substance for General and Scientific Use" [188] (IAPWS-95). IAPWS-95 is a multi-parameter EoS and provides the most accurate description of the whole phase space of H_2O to date. However, the formulation is computationally very involved.

In 1997 an improved formation for industrial use "IAPWS Industrial Formulation 1997 for the Thermodynamic Properties of Water and Steam" [86, 189] (IAPWS 1997 industrial formulation [189, 190] (IAPWS-IF97)) was published. In comparison to IFC-67, IAPWS-IF97 significantly improves accuracy and computational speed [190]. Between 2001 and 2005 so-called backward equations were adopted by IAPWS, which are all given in [190]. To achieve a high accuracy, IAPWS-IF97 is coupled to the scientific standard [188]. Figure 2.5 outlines the different fundamental regions in p-T space,

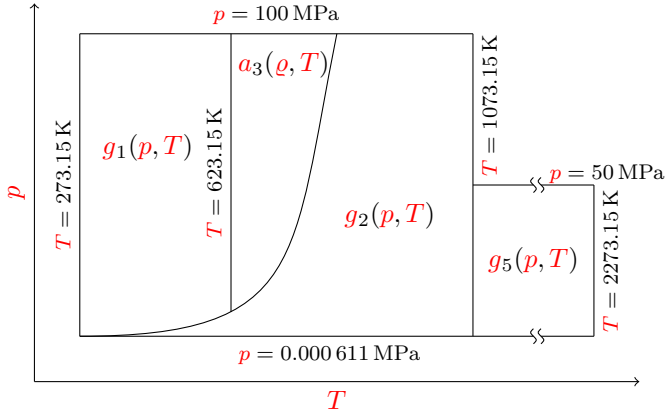

Figure 2.5: Outline of the IAPWS-IF97 structure; for details see [190]

for which either a fundamental equation for the specific Gibbs free energy $g = g(p, T)$ or for the specific Helmholtz free energy $a = a(\varrho, T)$ is given. The saturation curve is formulated in terms of saturation pressure and saturation temperature equations. The backward equations enable the direct calculation of the quantities without having to compute them iteratively from the basic equations. A complete description of the IAPWS-IF97 is given in [190]. In addition to thermodynamic properties, IAPWS also provides steadily updated formulations for transport properties and also for the surface tension of a flat water film. These can also be found in [190], updated versions are available on the website of the IAPWS.

In order to further improve the computational speed while maintaining high accuracy, so-called table look-up methods can be employed, see section 2.1.1.2. For its application to H_2O, IAPWS issued the "Guideline on the Fast Calculation of Steam and Water Properties with the Spline-Based Table Look-Up Method (SBTL)" as an international standard [89]. It applies polynomial spline interpolation to reproduce the results of existing equations of state, like IAPWS-95 or IAPWS-IF97, with high accuracy and low computing time [88]. The advantage of using spline functions lies in a continuous representation of the thermodynamic properties over the whole tabulated phase space in contrast to IAPWS-IF97 and, e.g., the Tabular Taylor Series Expansion method [74, 113]. The SBTL method employs bi-quadratic spline polynomials, which are continuously differentiable once and can easily be solved analytically in terms of the independent variables to provide numerically consistent backward functions (inverse spline functions). Especially

manufactured for the density-based solution approach, the spline functions are formulated in (ϱ, e) [87, 89]. Backward functions for the combinations (p, ϱ), (e, s), (h, s) and (p, s) are available. Details of accuracy and speed for a tabulation of IAPWS-IF97 are given in [87, 89].

It is emphasized that the SBTL method is applicable to any available EoS, providing a universal interface for every considered working medium. This allows to use the same solver implementation with only minor adaptions. In addition to SBTL library versions for H_2O an implementation for CO_2 is also used in this work, as published in [81]. Furthermore, the SBTL methodology has been extended for real gas mixtures and applied in the presented solution method to humid air computations in [76].

As previously explained, modeling and computation of condensing flows requires properties at metastable conditions normally obtained by extrapolation. As no experimental data is available, state equations cannot be properly validated in this region. The library adopted in this work for condensing wet steam flows is based on the most accurate thermodynamic data available, using the IAPWS-95 state equation for liquid states and the Wagner and Pruß gas equation [188] for gas and metastable states. It is well known that direct extrapolation of IAPWS-95 into the metastable region leads to anomalous behavior [159, 189] (for this reason, the gas equation also serves as basis for the IAPWS-IF97 formulation in the metastable region [189]).

For comparison of computational speed and accuracy, another popular EoS for wet steam flows is implemented. Young's state equation from 1988 [207] is a virial EoS

$$p\left(\varrho, T\right) = \varrho R_u T \left(1 + B(T)\varrho + C(T)\varrho^2\right), \tag{2.116}$$

with additional formulations for the saturation curve $p_s = p_s\left(T_s\right)$ and an expression for the liquid density $\varrho_L = \varrho_L\left(T_s\left(p\right)\right)$. The additionally needed properties surface tension, molecular viscosity and thermal conductivity coefficient are calculated in all presented computations based on according IAPWS formulations, as presented in [190].

On basis of nucleation theory and the thermodynamic description of H_2O, the wet steam model formulations used in this work are introduced in the next section.

2.3.3 Wet steam model formulations

In the following section, monodispersed source term and mixture models are presented and compared. The equations describing the condensing liquid phase are simplified by means of several assumptions specific to the considered wet steam flows [135, 136] (see also [99]):

- Only homogeneous condensation is taken into account and modeled based on the classical nucleation theory described in section 2.3.1.
- Both phases are at same pressure p.
- The condensed droplets are so small in size (in the considered test cases in the order of ten nanometers) that they perfectly follow the surrounding vapor. Neglecting the velocity slip, only one momentum equation must be solved.
- Droplets do not appear at high mass fractions, therefore, the volume occupied by the liquid can be neglected.
- The droplet distribution can be adequately represented by an equivalent monodispersion of a mean size. This is considered to provide satisfactory results for straightforward nucleating expansions with a single nucleation event [70].

To account for the condensed liquid phase, one additional governing equation for the liquid phase mass (wetness) fraction y must be formulated and solved. Then, the monodispersed assumption allows to compute an approximate droplet size distribution based on only one additional transport equation for the droplet number per unit mass N. Assuming spherical droplets with a mass

$$m_D = 4/3\,\pi \varrho_L r^3, \tag{2.117}$$

in combination with a cell-averaged droplet mass

$$\langle m_D \rangle \simeq y/N, \tag{2.118}$$

allows to compute a cell-averaged droplet radius

$$\langle r \rangle = \left(3y/(4\varrho_L \pi N)\right)^{1/3}. \tag{2.119}$$

The condensing mass flow per unite volume is then given by

$$\dot{m}_c = 4/3\pi {r_c}^3 \varrho_L J + 4\pi \langle r \rangle^2 N \varrho_L \varrho_G \,\mathrm{d}\langle r \rangle / \mathrm{d}t. \tag{2.120}$$

On this basis, the mixture model and the source term model are introduced in the following in a monodispersed formulation for brevity. Formulations based on the moment method are straightforward extensions with additional transport equations for the higher order moments and corresponding adaptions to the radius computation (2.119). Both formulations are compared in chapter 4.

2.3.3.1 Monodispersed mixture model

The most commonly used mathematical model for wet steam flows in the literature is the mixture model, which also represent the most often employed formulation in [171]. Basic idea of the mixture model is to formulate the governing equations (2.1) in terms of mixture quantities of a gas-liquid mixture

$$\underline{w}\left(\underline{x},t\right) \coloneqq \left(\varrho_m, \varrho_m \underline{u}, \varrho_m E_m, \varrho_m y, \varrho_m N\right), \tag{2.121}$$

defined by

$$\varrho_m{}^{-1} = \left(1-y\right)\varrho_G{}^{-1} + y\varrho_L{}^{-1} \tag{2.122}$$

and

$$e_m = \left(1-y\right)e_G + y e_L. \tag{2.123}$$

The mixture's total internal energy is given by

$$E_m \coloneqq e_m + \underline{u}\cdot\underline{u}/2. \tag{2.124}$$

As $y \ll 0$ and $\varrho_L \gg 1$, the simplification to neglect the volume occupied by the condensed liquid is justified, allowing to compute the gas density simply by

$$\varrho_G \approx \left(1-y\right)\varrho_m. \tag{2.125}$$

Then, the mixture pressure

$$p\left(\underline{w}\right) = p\left(\varrho_m, e_m, y\right) \tag{2.126}$$

can be iterated from

$$0 = e_m - \left(1-y\right)e\left(\varrho_G, p\right) - y\, e_L\left(T_s\left(p\right), p\right). \tag{2.127}$$

I.e., that the advective fluxes corresponding to the conservative variables, given in eq. (2.121),

$$\underline{\underline{F}}^a\left(\underline{w}\right) \coloneqq \left(\varrho_m\underline{u}, \varrho_m\underline{u}\otimes\underline{u} + p\left(\underline{w}\right)\underline{\underline{I}}, \varrho_m\underline{u}\left(E_m + p\left(\underline{w}\right)/\varrho_m\right), \varrho_m\underline{u}y, \varrho_m\underline{u}N\right), \tag{2.128}$$

as used in the governing equations (2.1), contain an additional active scalar y, which influences the thermodynamic state. This complicates the derivation and implementation of the numerical flux calculation, the reconstruction, the boundary treatment and the derivation of the Jacobian of the advective fluxes. As the coupling of both phases is realized based on the definition of

the mixture quantities (2.122) and (2.123), the source terms to be used in eq. (2.1) are given by

$$\underline{s}\left(\underline{w}\right) \coloneqq \left(0, \underline{0}, 0, \dot{m}_c, J\right). \tag{2.129}$$

In the diffusive fluxes, the diffusivity of the wetness fraction is neglected

$$\underline{\underline{F}}^d\left(\underline{w}\right) \coloneqq \left(\underline{0}, \underline{\tau}\left(\underline{w}\right), \underline{\tau}\left(\underline{w}\right) \cdot \underline{u} - \underline{q}\left(\underline{w}\right), 0, 0\right). \tag{2.130}$$

Overall, the mixture model represents a straightforward extension to account for non-equilibrium condensation effects in wet steam flows, substantiating its popularity. However, it has the disadvantage of containing an active scalar complicating derivation and implementation and also necessitating the cumbersome iteration process (2.127) with negative implications on the computational speed, see fig. 4.3.

2.3.3.2 Monodispersed source term model

A viable alternative to the mixture model represents the source term model. Assuming $\varrho \approx \varrho_G$ and $e \approx e_G$ allows to formulate the governing equations (2.1) in terms of gas properties with two additional equations

$$\underline{w}\left(\underline{x}, t\right) \coloneqq \left(\varrho_G, \varrho_G \underline{u}, \varrho_G E_G, \varrho_G y, \varrho_G N\right). \tag{2.131}$$

The corresponding advective fluxes are given by

$$\underline{\underline{F}}^a\left(\underline{w}\right) \coloneqq \left(\varrho_G \underline{u}, \varrho_G \underline{u} \otimes \underline{u} + p\left(\underline{w}\right) \underline{\underline{I}}, \varrho_G \underline{u}\left(E_G + p\left(\underline{w}\right)/\varrho_G\right), \varrho_G \underline{u} y, \varrho_G \underline{u} N\right), \tag{2.132}$$

where

$$E_G \coloneqq e_G + \underline{u} \cdot \underline{u}/2. \tag{2.133}$$

With this formulation, the pressure can directly be computed from the gas phase properties

$$p\left(\underline{w}\right) = p\left(\varrho_G, e_G\right) \tag{2.134}$$

and the wetness fraction y is a passive scalar without influence on thermodynamic and transport properties, in difference to the mixture model formulation.

The phases are coupled directly through appropriate source terms

$$\underline{s}\left(\underline{w}\right) \coloneqq \left(-\dot{m}_c, -\dot{m}_c \underline{u}, -\dot{m}_c\left(H_G - h_{fg}\right), \dot{m}_c, J\right), \tag{2.135}$$

where the condensing mass flow $\dot{m}_c$ and associated losses of momentum and energy are subtracted from the transport equations of the gas phase. In

the energy equation source term, the latent heat release is accounted for. The diffusive fluxes are again given by eq. (2.130).

Overall, the source term model has the big advantage, compared to the mixture model, that the wetness fraction is a passive scalar without immediate influence on thermodynamic and transport properties. This allows for a straightforward extension of the reconstruction and the boundary treatment for the additional scalars and a straightforward derivation of the Jacobian of the advective fluxes. Also, no iteration process is necessary leading to enhanced computational speed as compared to the mixture model, see fig. 4.3. Therefore, this formulation is employed for all complex computations. The Favre-filtered version of the monodispersed source term model is presented in [137].

After the introduction of the governing equations in different formulations with increasing complexity, ranging from thermodynamically generalized single-phase gas flows in absolute and relative frames, their extension to convenient descriptions of turbulent flows and the mathematical description to condensing wet steam flows, the development of numerical solution strategies for these governing equations in concrete technical applications is subject of the next chapter.

3 Solution Method

The purpose of computation is insight, not numbers.

Richard Hamming, American computer scientist and mathematician, 1973

In this chapter, we are concerned with finding the solution to a concrete fluid dynamical problem described mathematically by an initial-boundary value problem (IBVP). It consists of a set of nonlinear PDEs, representing the governing equation of a fluid flow, here, with special emphasis on flows including complicated gas properties as described in the last chapter, a set of boundary conditions confining and characterizing a finite domain in which the flow is to be computed and an initial field, as the starting point of the time integration.

Until today, no general closed-form analytical solution to the Navier-Stokes equations could be found [4] and so the only possibility to make an at least approximate prediction of the flow solution to the considered IBVP is the application of numerical methods. Such numerical methods for high speed flows, possibly including shock waves and strong real gas effects, are developed and presented in this chapter. In fact, the only few known exact analytical solutions for very simple IBVPs are often employed for the validation of numerical methods, which is otherwise based on experimental results. Another source of validation data are validated numerical methods of high quality, which can be employed for detailed "numerical experiments". These also allow insight into problems not realizable under laboratory conditions. A high quality numerical method for such "numerical experiments" is also presented in this chapter.

The development of a numerical solution method is concerned with finding a suitable transformation of complex mathematical equations into a representation, which can be solved via algebraic computation on digital computers, leading ultimately to a close approximation of the exact solution. Such numerical solution methods for complex non-ideal gas flows, of which the mathematical description is presented in the previous chapter, are described in the following. Their implementation on digital computers allows finding approximate numerical solutions, where the accuracy and the predictive na-

ture of the numerical solution depends on the mathematical model and the quality of the numerical solution method. Here, the ultimate goal is to account accurately for all relevant physical aspects as to create a full virtualization of the product—a digital twin—to attain optimized design and to reduce production and life cycle costs.

The transformation of the continuously defined IBVP into a discrete counterpart is termed discretization. As customary in computational gas dynamics [127], the method of lines approach is adopted in this work, where the spatial discretization and the subsequent integration in time are separated. In this work, we deal exclusively with density-based fully-coupled solution schemes exploiting the physical properties of high speed flows. Pressure-based solution methods, devised originally for the incompressible Navier-Stokes equations, have also been extended to application in compressible flows; however, it is not very likely that any pressure-based alternative could compete with the existing density-based solvers in the case of compressible flows [110]. Details about pressure-based solution methods may be found, e.g., in [40, 67, 69], a detailed comparison of density-based and pressure-based solution methods over a range of flow speeds is, e.g., given in [110].

Following the methodology of the method of lines approach, the spatial discretization of the governing equations is discussed first. Here, the finite volume method (FVM) is presented as the current standard and preferred discretization technique for general purpose technical numerical flow solvers. In addition, the finite difference method (FDM) is introduced, as applied for highly accurate simulations of simple geometries appropriate for "numerical experiments". Both discretization techniques result in ordinary differential equations (ODEs), which are integrated in time by the schemes presented in section 3.2. Accurate treatment of the boundary conditions of the IBVP is essential and discussed in section 3.3. Finally, both solvers are validated for their use in scale resolving computations in section 3.4.

3.1 Spatial discretization

In this work, we focus exclusively on structured grids, where complex geometries are conveniently treated applying the FVM up to second order accuracy, while the FDM is suitable for arbitrary order discretizations of "simple" geometries. An introduction to both methods can be found, e.g., in [68, 181], a comparison is given in [185]. High order methods for complex geometries based on unstructured grids are focus of ongoing research. A vast number of different approaches have been developed, including discontinuous Galerkin (DG) [8, 22], Spectral Difference [84, 191, 195], Spectral Volume [194, 195], Flux

Reconstruction [73, 200] and arbitrary accuracy schemes based on derivative Riemann problems (ADER) [181] schemes. Reviews are given, e.g., in [35, 192, 193]. Extensions of these methods to application in real gas flows will be subject of future research.

3.1.1 Finite Volume Method

The integral (weak) form of a conservation law is the basis of the FVM. In this way, the FVM is constructed to automatically satisfy the discrete conservation property and deals naturally with complex geometries, allowing for a discretization directly in physical space.

Let $\Omega \subset \mathbb{R}^3$ be the computational domain and $\hat{\underline{n}}$ the outward unit normal vector to the boundary $S(\Omega)$ of Ω. Integration of a governing equation of the form (2.1) over Ω and application of Gauss's theorem yields the weak conservative form

$$\partial_t \int_\Omega \underline{w} \, \mathrm{d}\underline{x} + \oint_{S(\Omega)} \hat{\underline{n}} \cdot \underline{\underline{F}} \, \mathrm{d}S = \int_\Omega \underline{s} \, \mathrm{d}\underline{x} \,. \tag{3.1}$$

By decomposition of Ω into n non-overlapping control volumes Ω_i

$$\Omega = \bigcup_{i=1}^{n} \Omega_i, \tag{3.2}$$

eq. (3.1) can be given equivalently by n equations

$$\partial_t \int_{\Omega_i} \underline{w} \, \mathrm{d}\underline{x} + \oint_{S(\Omega_i)} \hat{\underline{n}}_i \cdot \underline{\underline{F}} \, \mathrm{d}S = \int_{\Omega_i} \underline{s}_i \, \mathrm{d}\underline{x} \quad \forall i = 1..n. \tag{3.3}$$

The continuous solution within each control volume Ω_i is approximated by

$$\underline{w}_i(t) \cong \underline{w}(\underline{x}, t)\Big|_{\underline{x} \in \Omega_i}, \tag{3.4}$$

which should be considered an approximation of the mean value of $\underline{w}$ over the control volume Ω_i [57]

$$\underline{w}_i(t) \approx |\Omega_i|^{-1} \int_{\Omega_i} \underline{w}(\underline{x}, t) \, \mathrm{d}\underline{x} \,, \tag{3.5}$$

where $|\Omega_i|$ denotes the volume of Ω_i. Formally assigning $\underline{w}_i$ to the center $\underline{x}_i$ of Ω_i, eq. (3.5) represents the second order accurate midpoint rule. I.e.,

the solution of the IBVP is approximated with second order accuracy by n discrete values

$$\underline{w}\left(\underline{x},t\right)\Big|_{\underline{x}\in\Omega} \cong \bigcup_{i=1}^{n} \underline{w}_i\left(t\right). \tag{3.6}$$

Introducing the second order approximation (3.5) into eq. (3.3) yields the semidiscrete equation

$$\frac{\mathrm{d}}{\mathrm{d}t}\,\underline{w}_i\left(t\right) = -\left|\Omega_i\right|^{-1} \sum_{j\in N(i)} \left|S_{ij}\right| \underline{\Phi}\left(\underline{w}_i\left(t\right), \underline{w}_j\left(t\right), \underline{\hat{n}}_{ij}, \ldots\right) + \underline{s}_i\left(t\right) \;\forall i = 1..n, \tag{3.7}$$

with the set of adjacent cells of Ω_i

$$N\left(i\right) := \left\{ j \in \mathbb{N} \,|\, S\left(\Omega_i\right) = \bigcup_{j=1}^{m} S_{ij}\,,\; S_{ij} := \Omega_i \cap \Omega_j \right\}, \tag{3.8}$$

where the m intersections (inter-cell boundaries) S_{ij} are characterized by the areas $\left|S_{ij}\right|$ and the outward unit normal vectors $\underline{\hat{n}}_{ij}$. As the numerical solution is discontinuous on the inter-cell boundaries, the surface integral of the flux has to be evaluated approximately introducing a numerical flux function $\underline{\Phi}\left(t\right)$ constructed from the adjacent states. Independent of the numerical flux formulation, the physical flux given by the surface integral across S_{ij} in eq. (3.7) is approximated at most with second order accuracy, as the midpoint rule is applied again.

The actual challenge is the proper design of the numerical flux function, which has to account for the underlying nature of the physical flux. As advective and diffusive fluxes, defined in eq. (2.3), are of distinct physical nature, their numerical fluxes are independently designed

$$\underline{\Phi}\left(t\right) := \underline{\Phi}^a\left(t\right) + \underline{\Phi}^d\left(t\right), \tag{3.9}$$

where the advective flux is governed by hyperbolic and the diffusive flux by parabolic behavior [68, 69]. The diffusive fluxes are always centrally discretized [69], here with a second order approximation, and unaffected by real gas behavior. In the developed solution method, the gradients are calculated using finite differences applying a local transformation from Cartesian to curvilinear coordinates to attain high accuracy. The appropriate construction of numerical fluxes for the advective part is much more involved and influenced by gas properties, because commonly upwind schemes based on the physical properties of wave propagation are employed. Special care has also to be paid to their construction for application in scale-resolving simulations

like LES. The construction of numerical fluxes for the advective part is discussed in section 3.1.3. The FVM method has been validated and used for a number of publications, ranging from wet steam flows [136, 137], supercritical real gas CO_2 flows [81] to even real gas mixtures, like humid air [76] and ORC flows [210].

To attain high order schemes for "numerical experiments" in simple geometry settings, another discretization technique is employed, as described in the following.

3.1.2 Finite Difference Method

The FDM is applied directly to the differential form of the governing equations (2.1), where the derivative operators of the flux divergence, shown here in Cartesian tensor index notation with Greek indices for convenience

$$\partial_t \underline{w} + \sum_{\alpha=1}^{3} \underline{\hat{e}}_\alpha \cdot \frac{\partial}{\partial \underline{x}_\alpha} \left(\underline{\underline{F}}^a - \underline{\underline{F}}^d \right) = \underline{s}, \tag{3.10}$$

are approximated by finite differences, typically of high order, as follows.

In this work, the FDM is applied only on three-dimensional uniform structured Cartesian grids, consisting of the discrete points

$$\underline{x}_{i,j,k} \coloneqq \underline{x}_{0,0,0} + i\Delta_1 \, \underline{\hat{e}}_1 + j\Delta_2 \, \underline{\hat{e}}_2 + k\Delta_3 \, \underline{\hat{e}}_3, \tag{3.11}$$

with the space increments Δ_i and the Cartesian unit vectors $\{\underline{\hat{e}}_1, \underline{\hat{e}}_2, \underline{\hat{e}}_3\} \in \{\underline{\hat{e}}_x, \underline{\hat{e}}_y, \underline{\hat{e}}_z\}$. An extension to general structured curvilinear grids is possible by mapping to a regular computational grid [40]. The continuous solution at each grid point is approximated by

$$\underline{w}_{i,j,k}(t) \cong \underline{w}(\underline{x}_{i,j,k}, t), \tag{3.12}$$

such that the solution of the IBVP is approximated by the discrete values

$$\underline{w}(\underline{x}, t)\Big|_{\underline{x} \in \Omega} \cong \bigcup_{i=1}^{I} \bigcup_{j=1}^{J} \bigcup_{k=1}^{K} \underline{w}_{i,j,k}(t), \tag{3.13}$$

with I, J, K being the number of grid points in i, j, k direction.

Introducing the discretization of the derivatives of the fluxes at $\underline{x}_{i,j,k}$ in direction $\underline{\hat{e}}_\alpha$ adequately constructed from the available discrete values

$$D_{i,j,k}\left(\underline{\hat{e}}_\alpha \cdot \underline{\underline{F}}\,; \underline{x}_{i,j,k}, \ldots, t\right) \cong \frac{\partial \left(\underline{\hat{e}}_\alpha \cdot \underline{\underline{F}}\right)}{\partial \underline{x}_\alpha}(\underline{x}_{i,j,k}, t), \tag{3.14}$$

yields the semidiscretization

$$\frac{\mathrm{d}}{\mathrm{d}t}\,\underline{w}_{i,j,k} = -\sum_{\alpha=1}^{3}\left(D_{i,j,k}\left(\hat{\underline{e}}_\alpha \cdot \underline{\underline{F}}^a\right) - D_{i,j,k}\left(\hat{\underline{e}}_\alpha \cdot \underline{\underline{F}}^d\right)\right) + \underline{s}_{i,j,k}, \tag{3.15}$$

which can be integrated in time by dedicated schemes for ODEs (see section 3.2).

To improve accuracy and robustness [127, 153], the diffusive fluxes are discretized in non-conservative form, as follows: Introducing the Cartesian index notation with Greek indices for clarity, the diffusive fluxes are given by

$$\frac{\partial\left(\hat{\underline{e}}_\alpha \cdot \underline{\underline{F}}^d\right)}{\partial \underline{x}_\alpha} = \frac{\partial F^d_{\alpha\beta}}{\partial x_\alpha} = \frac{\partial}{\partial x_\alpha}\begin{pmatrix} 0 \\ \tau_{\alpha\beta} \\ \tau_{\alpha\beta}u_\beta - q_\alpha \end{pmatrix}. \tag{3.16}$$

The diffusive flux of the momentum conservation equation

$$\frac{\partial \tau_{\alpha\beta}}{\partial x_\alpha} = \frac{\partial}{\partial x_\alpha}\left(\mu\left(\frac{\partial u_\beta}{\partial x_\alpha} + \frac{\partial u_\alpha}{\partial x_\beta}\right) - \frac{2}{3}\mu\frac{\partial u_\gamma}{\partial x_\gamma}\delta_{\alpha\beta}\right) \tag{3.17}$$

is expended to

$$\begin{aligned}\frac{\partial \tau_{\alpha\beta}}{\partial x_\alpha} = \mu\frac{\partial^2 u_\beta}{\partial x_\alpha^2} + \frac{\partial \mu}{\partial x_\alpha}\left(\frac{\partial u_\beta}{\partial x_\alpha} + \frac{\partial u_\alpha}{\partial x_\beta}\right) \\ + \frac{1}{3}\mu\frac{\partial}{\partial x_\beta}\left(\frac{\partial u_\alpha}{\partial x_\alpha}\right) - \frac{2}{3}\frac{\partial u_\gamma}{\partial x_\gamma}\frac{\partial \mu}{\partial x_\beta},\end{aligned} \tag{3.18}$$

where dedicated second derivative approximations are used for the appearing second order terms to avoid odd-even decoupling. The same applies to the diffusive flux of the energy conservation equation

$$\frac{\partial}{\partial x_\alpha}(\tau_{\alpha\beta}u_\beta + q_\alpha) = u_\beta\frac{\partial \tau_{\alpha\beta}}{\partial x_\alpha} + \tau_{\alpha\beta}\frac{\partial u_\beta}{\partial x_\alpha} + \frac{\partial \lambda}{\partial x_\alpha}\frac{\partial T}{\partial x_\alpha} + \lambda\frac{\partial^2 T}{\partial x_\alpha^2}. \tag{3.19}$$

The appearing derivatives are approximated by 6$^{\text{th}}$ order central differences

$$D_i(\phi) = \frac{\phi_{i+3} - 9\phi_{i+2} + 45\phi_{i+1} - 45\phi_{i-1} + 9\phi_{i-2} - \phi_{i+3}}{60\Delta_i} + \mathcal{O}\left(\Delta_i^6\right), \tag{3.20}$$

and for second derivatives

$$\begin{aligned}D_i^{(2)}(\phi) = \\ \frac{2\phi_{i+3} - 27\phi_{i+2} + 270\phi_{i+1} - 490\phi_i + 270\phi_{i-1} - 27\phi_{i-2} + 2\phi_{i+3}}{180\Delta_i} \\ + \mathcal{O}\left(\Delta_i^6\right).\end{aligned} \tag{3.21}$$

Coefficients, optimized for behavior in wave number-frequency space, called dispersion-relation-preserving schemes [13, 176], are also implemented. Implicit compact schemes [93] are not yet implemented, as their efficient multi-thread parallelization is much more involved.

To ensure conservation, the advective fluxes are discretized in local discrete conservative form [30]

$$\sum_{\alpha=1}^{3} D_{i,j,k}\left(\underline{\hat{e}}_\alpha \cdot \underline{\underline{F}}^a\right) = \frac{\underline{\Phi}^a_{i+1/2,j,k}\left(\underline{\hat{e}}_1,\dots\right) - \underline{\Phi}^a_{i-1/2,j,k}\left(\underline{\hat{e}}_1,\dots\right)}{\Delta_1} + \frac{\underline{\Phi}^a_{i,j+1/2,k}\left(\underline{\hat{e}}_2,\dots\right) - \underline{\Phi}^a_{i,j-1/2,k}\left(\underline{\hat{e}}_2,\dots\right)}{\Delta_2} + \frac{\underline{\Phi}^a_{i,j,k+1/2}\left(\underline{\hat{e}}_3,\dots\right) - \underline{\Phi}^a_{i,j,k-1/2}\left(\underline{\hat{e}}_3,\dots\right)}{\Delta_3}, \quad (3.22)$$

with the numerical fluxes $\underline{\Phi}^a$ approximating the advective fluxes at the uniformly spaced grid interfaces, as presented in the following section. High order central, upwind or hybrid flux functions are employed in the FDM solver. The FDM solver is thoroughly validated for ideal gas as well as for CO_2 real gas flows in [134].

3.1.3 Numerical flux functions for the advective Fluxes

The advective fluxes represent the "Euler-part" of the full Navier-Stokes equations (see chapter 2), a set of hyperbolic PDEs [68, 181]. This fact has certain implications on the construction of the numerical flux functions, as hyperbolic systems are associated with wave propagation and admit wave-like solutions [67]. Numerically, it is generally accepted that the hyperbolic part poses the most stringent requirements on the discretization techniques [181]. However, the theory of hyperbolic systems is much more advanced than that for the full Navier-Stokes equations, which are of parabolic-hyperbolic type [68]. I.e., the solution of the full Navier-Stokes equations in density-based solution methods, as presented in this work, can be regarded as an extension of the solution method to the hyperbolic "Euler-part"—represented by the advective fluxes—by addition of the centrally discretized diffusive fluxes. This is often done without sound mathematical basis, but experience shows that satisfactory results can be obtained as long as one is not concerned with fine details of the flow [181], as, e.g., in "numerical experiments".

When shock waves—associated with hyperbolic behavior—enter the solution, all methods for smooth turbulent flows—governed by parabolic behavior—suffer from spurious Gibbs oscillations near shock jumps, which may

lead to nonlinear instabilities [127]. The onset of oscillations in the proximity of shock waves can be avoided or at least limited by either shock-fitting or shock-capturing approaches, whereas only the latter is feasible for general application [127]. Shock waves are extremely thin regions of the order of the mean-free molecular path length of the fluid molecules; this suggests that the continuum hypothesis, applied in the derivation of the governing equations, is not appropriate to resolve their physical structure [79]. To achieve an accurate and stable resolution of shocked flows on a computational grid without special shock fitting, traditional shock-capturing methods rely on two basic ingredients: formulation and solution of the governing equations in conservative from to ensure the convergence to the correct weak solution [181] and the addition of numerical dissipation in the vicinity of shock waves, resulting in smearing the shocks over a certain number of grid points [79]. In this section, upwind flux shock-capturing formulations adapted to real gas flows are presented.

Such traditional shock-capturing methods are, however, independent of their order, not appropriate for "numerical experiments" or accurate scale resolving computations of shock-turbulence interaction (STI)—smooth turbulence in presence of shock waves—due to the inevitable numerical dissipation in smooth turbulence regions, leading to the depletion especially of important small structures, and their high computational demand. The proper numerical treatment of STI is still subject to ongoing research [79, 90]. Its accurate numerical treatment is challenging due to the contradictory requirements to minimize any numerical dissipation for a precise representation of the turbulent spectrum, especially at the small scales, whilst providing stability in the presence of shock waves typically accomplished by introducing numerical dissipation [90].

Even in absence of shocks, the straightforward central discretization of the compressible Navier-Stokes equations in divergence form—the form as given in eq. (2.4)—works only as long as nonlinearities are weak [127]. In high-Reynolds number fluid turbulence, numerical instabilities are encountered and upwinding, filtering, energy- or entropy-consistent schemes must be used [127]. In this work, non-dissipative central discretizations in energy-consistent split form are described and employed.

To ensure the same dissipation-free treatment of turbulence in presence of shock waves, an obvious idea is to combine a baseline spectral-like scheme with shock-capturing capabilities through the local replacement with a classical shock-capturing approach forming a hybrid scheme. A similar strategy, though not pursued in this work, is nonlinear filtering for the controlled addition of shock-capturing dissipation [127]. A key role in this class of schemes is played by the shock sensor; this sensor must be defined in such a way that

numerical dissipation is effectively confined in shocked regions, so that it does not pollute smooth parts of the flow field [127]. Overall, hybrid methods offer the potential for shock-turbulence calculations with substantially reduced dissipation and computational times [90] and are here employed for scale resolving simulations of complex real gas flows, including condensing wet steam flows.

3.1.3.1 Central flux

To discretize the governing equations in smooth flow regions, the most obvious choice is the application of finite central difference approximations to the divergence of the advecitve flux (2.4) [127], given here in Cartesian tensor index notation with Greek indices for convenience,

$$\frac{\partial \varrho u_\alpha \varphi_\beta}{\partial x_\alpha}, \underline{\varphi} = (1, \underline{u}, H) \tag{3.23}$$

and $\partial p / \partial x_\alpha$. These approximations can be explicit or implicit (compact) [93] with coefficients optimized for maximal formal accuracy (order) or behavior in wave number-frequency space (dispersion-relation-preserving schemes [13, 176]).

In the present work, central flux formulations in energy-consistent split form are employed of 2$^{\text{nd}}$ order in the FVM and of 6$^{\text{th}}$ order in the FDM solver, respectively. Energy-consistent schemes attempt to replicate the energy preservation properties of the governing equations in the discrete sense [127] by splitting the convective derivatives in the advective fluxes. The presented split forms are often improperly referred to as skew-symmetric forms [127]. Application of explicit central finite differences in these formulations does not only allow a straightforward parallel implementation on GPU architectures, but also guarantees local discrete conservation contrary to compact approximations [127].

Different split forms of eq. (3.23) have been proposed by Feiereisen et al. [38]

$$\frac{\partial \varrho u_i \varphi}{\partial x_i} = \frac{1}{2}\left(\frac{\partial \varrho u_i \varphi}{\partial x_i} + \varphi \frac{\partial \varrho u_i}{\partial x_i} + \varrho u_i \frac{\partial \varphi}{\partial x_i}\right), \tag{3.24}$$

preserving kinetic energy at the semi-discrete level [126], by Blaisdell et al. [11]

$$\frac{\partial \varrho u_i \varphi}{\partial x_i} = \frac{1}{2}\left(\frac{\partial \varrho u_i \varphi}{\partial x_i} + u_i \frac{\partial \varrho \varphi}{\partial x_i} + \varrho \varphi \frac{\partial u_i}{\partial x_i}\right), \tag{3.25}$$

minimizing the aliasing error [127], and by Kennedy and Gruber [82]

$$\frac{\partial \varrho u_i \varphi}{\partial x_i} = \alpha \frac{\partial \varrho u_i \varphi}{\partial x_i} + \beta \left(u_i \frac{\partial \varrho \varphi}{\partial x_i} + \varrho \frac{\partial u_i \varphi}{\partial x_i} + \varphi \frac{\partial \varrho u_i}{\partial x_i} \right) + (1 - \alpha - 2\beta) \left(\varrho u_i \frac{\partial \varphi}{\partial x_i} + \varrho \varphi \frac{\partial u_i}{\partial x_i} + u_i \varphi \frac{\partial \varrho}{\partial x_i} \right) \tag{3.26}$$

for additional robustness in the presence of strong density variations and semi-discrete energy conservation for $\alpha = \beta = 1/4$ [127].

For the split forms (3.24) and (3.25) [30] presented corresponding flux formulations up to 6$^{\text{th}}$ order for the local discrete conservative form (3.22) on uniformly spaced grids. E.g., the 2$^{\text{nd}}$ order central flux in direction $\underline{\hat{n}}$ for split form (3.24) is given by

$$\underline{\Phi}^{c,\mathrm{F},\mathcal{O}(2)}_{i+1/2}\left(\underline{\hat{n}}, \dots\right) = 1/4 \left((\underline{\varrho u} \cdot \underline{\hat{n}})_i + (\underline{\varrho u} \cdot \underline{\hat{n}})_{i+1} \right) \left(\underline{\varphi}_i + \underline{\varphi}_{i+1} \right), \tag{3.27}$$

and for (3.25) by

$$\underline{\Phi}^{c,\mathrm{B},\mathcal{O}(2)}_{i+1/2}\left(\underline{\hat{n}}, \dots\right) = 1/4 \left((\underline{\varrho \varphi})_i + (\underline{\varrho \varphi})_{i+1} \right) \left((\underline{u} \cdot \underline{\hat{n}})_i + (\underline{u} \cdot \underline{\hat{n}})_{i+1} \right). \tag{3.28}$$

The corresponding flux in convective form equals

$$\underline{\Phi}^{c,\mathcal{O}(2)}_{i+1/2}\left(\underline{\hat{n}}, \dots\right) = 1/2 \left((\underline{\varrho u} \cdot \underline{\hat{n}} \underline{\varphi})_i + (\underline{\varrho u} \cdot \underline{\hat{n}} \underline{\varphi})_{i+1} \right). \tag{3.29}$$

Later, Pirozzoli [126] extended these fluxes and also the Kennedy and Gruber split form (3.26) to arbitrary order. The latter yields for the previous example

$$\underline{\Phi}^{c,\mathrm{KG},\mathcal{O}(2)}_{i+1/2}\left(\underline{\hat{n}}, \dots\right) = 1/8 \left(\varrho_i + \varrho_{i+1} \right) \left((\underline{u} \cdot \underline{\hat{n}})_i + (\underline{u} \cdot \underline{\hat{n}})_{i+1} \right) \left(\underline{\varphi}_i + \underline{\varphi}_{i+1} \right). \tag{3.30}$$

All three split forms (3.24) to (3.26) are implemented in both solvers, the Kennedy and Gruber split form (3.26) is used by default due to its improved robustness. Obviously, these central flux formulations are invariant with respect to the underlying gas model, as the discretization does not account for physical properties of the underlying terms (apart perhaps from the choice of splitting). This is not the case in upwind terms, where the wave propagation properties of the underlying equations are taken into account in the flux formulation.

3.1.3.2 Upwind flux

When shock waves enter the domain, all methods for smooth turbulent flows suffer from spurious Gibbs oscillations near shock jumps. In this work, classic shock-capturing upwind schemes are employed for shocked flows on

computational grids without special shock fitting as long as the required accuracy of the computations admits this. Otherwise, a hybrid treatment is used (see section 3.1.3.3). As mentioned in the introduction to this section, traditional shock-capturing methods rely on two basic ingredients: formulation and solution of the governing equations in conservative from to ensure the convergence to the correct weak solution [181] and the addition of numerical dissipation in the vicinity of shock waves to guarantee the stability of the numerical method. Such shock-capturing upwind schemes are in literature generally formulated under the assumption of ideal gas behavior, a comprehensive overview is given, e.g., in [69, 181]. Their extension to real gas flows is the main subject of the discussion here, where the complexity of this adaption depends strongly on the type of scheme.

Generally, classic shock-capturing schemes can be divided in two distinct categories: Flux Vector Splitting and Flux Difference Splitting methods. Flux Vector Splitting methods identify the upwind direction with less effort compared to the Flux Difference Splitting methods by splitting the fluxes with respect to the wave propagation of each underlying equation. This results in much more efficient schemes, however, with poorer resolution of discontinuities [181]. For non-ideal gas flows, their big advantage is the straightforward extension; often only the computation of the speed of sound has to be adapted. In this work, two type of AUSM schemes [103] are implemented and used for real gas flows based on a simple average of the sound speed, in particular AUSM+ [101] and AUSM+-up [100] for low speed flows.

The Flux Difference Splitting methods rely on the Godunov approach [58]. The basic idea is based on the observation that for a first order method at each interface in isolation, two constant states $\underline{w}_i$ and $\underline{w}_j$ meet. In a local, interface normal coordinate system this results in the (augmented) 1D Riemann problem

$$\left.\begin{aligned} \partial_t \underline{w} + \frac{\partial\left(\hat{\underline{n}}_{ij} \cdot \underline{\underline{F}}^a\right)}{\partial\left(\hat{\underline{n}}_{ij} \cdot \underline{x}\right)} &= \underline{0} \\ \underline{w}\left(\hat{\underline{n}}_{ij} \cdot \underline{x}, t\right)\big|_{t=t_0} &= \begin{cases} \underline{w}_i\,, & \hat{\underline{n}}_{ij} \cdot \underline{x} < 0 \\ \underline{w}_j\,, & \hat{\underline{n}}_{ij} \cdot \underline{x} > 0 \end{cases} \end{aligned}\right\}. \tag{3.31}$$

The numerical fluxes can now be computed from the evolution of this Riemann problem in time at the interface position. In the original Godunov method [58], this Riemann problem is solved exactly. However, this exact solution necessitates the very involved integration of the Riemann invariants along isentropes [181] and all modern Flux Difference Splitting methods rely therefore on approximate solutions to eq. (3.31), like, e.g., the approximate

Riemann solver of Roe [148]. Other approximate Riemann solvers for ideal gas can be found in [181]. Since the mid 1980s, the topic of adapting Godunov's method to real gas flows, including the exact solution of the Riemann problem for non-ideal gases, has been addressed by several authors [23, 109, 140, 154]. In this work, the approximate Riemann solver of Roe [148] is generalized for real gas flows in section 3.1.3.5, as the original Roe-type linearization for ideal gas is not uniquely determined for a real gas.

For technical applications, first order schemes are regarded as overly dissipative. For the FVM solver, Flux Vector Splitting and Flux Difference Splitting methods are extended to 2nd order accuracy by replacing the piecewise constant approximations with a first order linear reconstruction of both interface states prior to the numerical flux calculation, called MUSCL [183] approach. For detailed insight into the construction of higher order schemes, see [67, 69, 181]. The slopes in this work are limited with the van Albada limiter as presented in [12]. The MUSCL approach is directly applicable to real gas flows; only the choice of the reconstructed variable set is adopted for the respective real gas equation of state: for ideal gas, the standard primitive variables $(\varrho, \underline{u}, p)$ are used, for the tabulation method $(\varrho, \underline{u}, e)$ and for all other implemented EoS $(\varrho, \underline{u}, T)$ are used. Higher order flux computations in this framework are possible in principle on the employed structured meshes, however, the overall accuracy of the FDM formulation remains 2nd order accurate, as the midpoint rule is used, and the scheme does not provide a compact support. For the FDM solver, a 5th order WENO scheme is employed, as presented in section 3.1.3.6.

3.1.3.3 Hybrid flux

As mentioned in the introduction to this section, accurate scale resolving computations like LES and DNS require essentially non-dissipative schemes to prevent the depletion of especially the small scale motion. As long as no shock waves are present in the domain, the flux functions described in section 3.1.3.1 can be employed. Whenever both, shock waves and turbulence, are present in the flow, a hybrid flux treatment is adopted in this work, as described in the following.

The hybrid numerical flux is based on the idea of distinguishing regions of "smooth" turbulence from regions dominated by shock waves based on a shock sensor and applying appropriate numerical fluxes to the respective regions [79, 90]. In this way, the numerical treatment reflects the diverse physical nature of turbulence and shocks and is mathematically formulated as a linear combination of a non-dissipative central flux $\underline{\Phi}^c$ and a shock-capturing

upwind flux $\underline{\Phi}^u$

$$\underline{\Phi}_{i+1/2} = \underline{\Phi}^c_{i+1/2} + \psi_{i+1/2}\left(\underline{\Phi}^u_{i+1/2} - \underline{\Phi}^c_{i+1/2}\right). \tag{3.32}$$

Such a hybrid scheme also guarantees optimal performance, as the computationally elaborate upwind flux is only used when necessary. The quality of a hybrid discretization is largely dependent on the formulation of the shock sensor ψ, which is difficult to design for universal application [79].

In this work, a Ducros et al. [29] type dilatation-vorticity-sensor is used, as presented in [79, 90]

$$\chi_i = \frac{-\theta_i}{|\theta_i| + \sqrt{\underline{\omega}_i \cdot \underline{\omega}_i} + \varepsilon}, \tag{3.33}$$

with dilatation $\theta_i = \mathrm{div}\underline{u}_i$, vorticity $\underline{\omega}_i = \mathrm{curl}\,\underline{u}_i$ and a small real number $\varepsilon = 10^{-30}$ to prevent numerical divergence in regions where both, dilatation and vorticity, are zero. On this basis, the fluxes at the interface are switched checking all neighboring points that are used in the central flux stencil to ensure that central differencing is not done across any shocks, i.e. for the FDM solver with a 6th order baseline central scheme

$$\psi_{i+1/2} = \begin{cases} 1 & \text{if } \max\limits_{p=-2}^{3} \chi_{i+p} > 0.65 \\ 0 & \text{otherwise} \end{cases}. \tag{3.34}$$

For the 2nd order FVM solver, only the cells adjacent to the interface need to be checked. This formulation works well for traditional STI, but does not find contact discontinuities [90], fails entirely, whenever vorticity is not present (degenerating in this case to a sensor of flow compression regions [79]) and behaves inferior on very coarse grids, where the vorticity is poorly captured [79]. To remedy, [79] suggest averaging the denominator of the shock sensor (3.33) in some sense (locally, or in homogeneous directions) in order to prevent unnecessary switching in random regions of small vorticity; this is, however, not employed in this work. A further analysis of shock sensors is also given in [79]. For one-dimensional validation problems, the simple shock sensor formulation of Visbal and Gaitonde [186] is implemented and used.

3.1.3.4 Flux Jacobian for real gas flows

The extensions to real gas flows of the Roe scheme in section 3.1.3.5 and of the WENO schemes in section 3.1.3.6 rely on the construction of the Jacobian matrix of the advective fluxes (2.4) and its Eigendecomposition, as presented in this section. This is also important for the construction of other

schemes and for the derivation of boundary conditions for application in real gas flows.

For convenience, the conservative variables are defined as follows in this section

$$\underline{w} := \left(\varrho, \underline{\varpi}, \epsilon\right) = \left(\varrho, \varrho\underline{u}, \varrho E\right). \tag{3.35}$$

The Jacobian matrix of the advective fluxes in $\hat{\underline{n}}$ direction

$$\underline{\underline{A}}\left(\underline{w}, \hat{\underline{n}}\right) := \partial_{\underline{w}}\left(\hat{\underline{n}} \cdot \underline{\underline{F}}^{a}\right) \tag{3.36}$$

is derived here under the assumption of the general equation of state (2.10). Therefore, the derivation is much more involved as for the ideal gas case (2.27), which is contained as one special case. The interface normal projection of the advective flux vector (2.4), introducing the conservative variables as defined in eq. (3.35), is given by

$$\hat{\underline{n}} \cdot \underline{\underline{F}}^{a}\left(\underline{w}\right) = \left(\hat{\underline{n}} \cdot \underline{\varpi}, \varrho^{-1}\, \hat{\underline{n}} \cdot \underline{\varpi}\, \underline{\varpi} + p\left(\underline{w}\right) \hat{\underline{n}}, \varrho^{-1}\, \hat{\underline{n}} \cdot \underline{\varpi}\, \left(\epsilon + p\left(\underline{w}\right)\right)\right)^{\mathsf{T}}. \tag{3.37}$$

Derivation with respect to the conservative variables yields the Jacobian matrix (3.36)

$$\underline{\underline{A}}\left(\underline{w}, \hat{\underline{n}}\right) = \begin{pmatrix} 0 & \hat{\underline{n}}^{\mathsf{T}} & 0 \\ -\hat{\underline{n}} \cdot \underline{u}\, \underline{u} + \partial_{\varrho}\Pi\, \hat{\underline{n}} & \underline{u} \otimes \hat{\underline{n}} + \hat{\underline{n}} \otimes \partial_{\underline{\varpi}}\Pi + \hat{\underline{n}} \cdot \underline{u}\, \underline{\underline{I}} & \partial_{\epsilon}\Pi\, \hat{\underline{n}} \\ -\hat{\underline{n}} \cdot \underline{u}\, \left(H - \partial_{\varrho}\Pi\right) & \left(H\, \hat{\underline{n}} + \hat{\underline{n}} \cdot \underline{u}\, \partial_{\underline{\varpi}}\Pi\right)^{\mathsf{T}} & \left(1 + \partial_{\epsilon}\Pi\right) \hat{\underline{n}} \cdot \underline{u} \end{pmatrix}. \tag{3.38}$$

The partial derivatives of the pressure function can be evaluated applying the chain rule

$$\partial_{\underline{w}}\Pi =: \partial_{\underline{w}}\, p(\underline{w}) = \partial_{\underline{w}}\, p\left(\varrho\left(\underline{w}\right), e\left(\underline{w}\right)\right), \tag{3.39}$$

where

$$e\left(\underline{w}\right) = \varrho^{-1}\, \epsilon - \left(2\, \varrho^{2}\right)^{-1}\, \underline{\varpi} \cdot \underline{\varpi}. \tag{3.40}$$

This finally yields

$$\begin{aligned} \partial_{\varrho}\, p\left(\underline{w}\right) &= \partial_{\varrho}\, p\left(\varrho, e\right) - \varrho^{-1}\, \partial_{e}\, p\left(\varrho, e\right) \left(E - \underline{u} \cdot \underline{u}\right) \\ \partial_{\underline{\varpi}}\, p\left(\underline{w}\right) &= -\varrho^{-1}\, \underline{u}\, \partial_{e}\, p\left(\varrho, e\right) \\ \partial_{\epsilon}\, p\left(\underline{w}\right) &= \varrho^{-1}\, \partial_{e}\, p\left(\varrho, e\right). \end{aligned} \tag{3.41}$$

For the Eigendecomposition of the Jacobian matrix (3.38), let $\underline{\underline{\Lambda}}$ denote the matrix of the Eigenvalues and $\underline{\underline{R}}$ the matrix of the right Eigenvectors, such that

$$\underline{\underline{A}}\left(\underline{w}, \hat{\underline{n}}\right) = \left(\underline{\underline{R}}\, \underline{\underline{\Lambda}}\, \underline{\underline{R}}^{-1}\right)\left(\underline{w}, \hat{\underline{n}}\right). \tag{3.42}$$

The equilibrium speed of sound is expressed in terms of the state variables (ϱ, e) utilizing Gibbs' fundamental equation

$$a\,(\varrho, e)^2 = \partial_\varrho\, p\,(\varrho, s) = \partial_\varrho\, p\,(\varrho, e) + \varrho^{-2}\, p\,(\varrho, e)\;\; \partial_e\, p\,(\varrho, e)\,. \tag{3.43}$$

Then, the eigenvector matrix results in

$$\underline{\underline{\Lambda}}\,(\underline{w}, \hat{\underline{n}}) = \begin{pmatrix} \hat{\underline{n}} \cdot \underline{u}\, \underline{\underline{I}} & 0 & 0 \\ 0 & \hat{\underline{n}} \cdot \underline{u} + a & 0 \\ 0 & 0 & \hat{\underline{n}} \cdot \underline{u} - a \end{pmatrix}, \tag{3.44}$$

the corresponding matrix of the right Eigenvectors reads

$$\underline{\underline{R}}\,(\underline{w}, \hat{\underline{n}}) = \begin{pmatrix} \hat{\underline{n}}^{\mathsf{T}} & \alpha & \alpha \\ \underline{u} \otimes \hat{\underline{n}} + \varrho\,[\hat{\underline{n}}]_\times & \alpha\,(\underline{u} + a\hat{\underline{n}}) & \alpha\,(\underline{u} - a\hat{\underline{n}}) \\ \varphi\,\hat{\underline{n}}^{\mathsf{T}} - \varrho\,(\hat{\underline{n}} \times \underline{u})^{\mathsf{T}} & \alpha\,(H + a\,\hat{\underline{n}} \cdot \underline{u}) & \alpha\,(H - a\,\hat{\underline{n}} \cdot \underline{u}) \end{pmatrix}, \tag{3.45}$$

where

$$\begin{aligned} \alpha &:= (2\,\varrho)^{-1} \\ \varphi &:= H - (\partial_e\, p\,(\varrho, e))^{-1}\, a^2 \varrho \end{aligned} \tag{3.46}$$

and with the cross-product matrix of the unit normal vector $\hat{\underline{n}} \in \mathbb{R}^3$ defined by

$$[\hat{\underline{n}}]_\times := \begin{pmatrix} 0 & -n_3 & n_2 \\ n_3 & 0 & -n_1 \\ -n_2 & n_1 & 0 \end{pmatrix}. \tag{3.47}$$

The inverse is given by

$$\underline{\underline{R}}^{-1} := \begin{pmatrix} \sigma\,\hat{\underline{n}} + \varrho^{-1}\,\hat{\underline{n}} \times \underline{u} & a^{-2}\,\phi\,\hat{\underline{n}} \otimes \underline{u} - \varrho^{-1}\,[\hat{\underline{n}}]_\times & -a^{-2}\,\phi\,\underline{u} \\ \beta\left(a^2\,(1-\sigma) - a\,\hat{\underline{n}} \cdot \underline{u}\right) & -\beta\left(\phi\,\underline{u}^{\mathsf{T}} - a\,\hat{\underline{n}}^{\mathsf{T}}\right) & \beta\,\phi \\ \beta\left(a^2\,(1-\sigma) + a\,\hat{\underline{n}} \cdot \underline{u}\right) & -\beta\left(\phi\,\underline{u}^{\mathsf{T}} + a\,\hat{\underline{n}}^{\mathsf{T}}\right) & \beta\,\phi \end{pmatrix}, \tag{3.48}$$

with

$$\begin{aligned} \beta &:= \left(\sqrt{2}\,a\,\varrho\right)^{-1} \\ \phi &:= \varrho^{-1}\,\partial_e\, p\,(\varrho, e) \\ \sigma &:= a^{-2}\,\phi\,(H - \underline{u} \cdot \underline{u})\,. \end{aligned} \tag{3.49}$$

In the ideal gas case, with

$$\partial_e\, p^{\mathrm{IG}}\,(\varrho, e) = (\gamma - 1)\,\varrho, \tag{3.50}$$

such that

$$\begin{aligned}\varphi^{\mathrm{IG}} &= \frac{1}{2}\,\underline{u}\cdot\underline{u}\\ \phi^{\mathrm{IG}} &= (\gamma-1)\\ \sigma^{\mathrm{IG}} &= 1-\frac{1}{2}\,a^{-2}\,(\gamma-1)\,\underline{u}\cdot\underline{u},\end{aligned} \tag{3.51}$$

it can be easily verified that the given Eigendecomposition reduces to the decomposition in [139] (it appears that in eq. A.11 a sign error occurs for element (2,4) of the matrix).

3.1.3.5 Real gas Roe-type scheme

In this section, a Roe-type scheme for real gas flows is presented as implemented in the FVM solver. As will be shown, the Roe scheme cannot directly be applied to real gas flows, as it is not uniquely defined for the more general system. The basic idea of the Roe scheme is to linearize the PDE of the interface Riemann problem (3.31). Therefore, the PDE is written in quasi linear form

$$\partial_t\,\underline{w} + \underline{\underline{A}}\,(\underline{w},\underline{\hat{n}}_{ij})\cdot\frac{\partial\underline{w}}{\partial\,(\underline{\hat{n}}_{ij}\cdot\underline{x})} = \underline{0}, \tag{3.52}$$

which introduces the Jacobian matrix, as derived in section 3.1.3.4 for a general real gas flow.

We denote by $\breve{\underline{\underline{A}}}\,(\underline{w}_i,\underline{w}_j,\underline{\hat{n}}_{ij})$ the Roe-type linearization in $\underline{\hat{n}}_{ij}$ direction, when $\breve{\underline{\underline{A}}}$ meets following requirements defined by Roe [148]:

i. $\breve{\underline{\underline{A}}}$ constitutes a linear mapping from $\underline{w}$ to $\hat{n}\cdot\underline{\underline{F}}^a$,

ii. conservation:

$$\underline{\hat{n}}_{ij}\cdot\left(\underline{\underline{F}}^a\,(\underline{w}_i)-\underline{\underline{F}}^a\,(\underline{w}_j)\right) = \breve{\underline{\underline{A}}}\,(\underline{w}_i,\underline{w}_j,\underline{\hat{n}}_{ij})\cdot(\underline{w}_i-\underline{w}_j)\,, \tag{3.53}$$

iii. hyperbolicity: $\breve{\underline{\underline{A}}}\,(\underline{w}_i,\underline{w}_j,\underline{\hat{n}}_{ij})$ has real eigenvalues and a complete set of eigenvectors,

iv. consistency:

$$\breve{\underline{\underline{A}}}\,(\underline{w}_i,\underline{w}_i,\underline{\hat{n}}_{ij}) = \underline{\underline{A}}\,(\underline{w}_i,\underline{\hat{n}}_{ij})\,. \tag{3.54}$$

With this Roe-type linearization, instead of the exact Riemann problem (3.31), the linearized Riemann problem

$$\left.\begin{aligned} \partial_t \underline{w} + \breve{\underline{\underline{A}}}\left(\underline{w}_i, \underline{w}_j, \hat{\underline{n}}_{ij}\right) \cdot \frac{\partial \underline{w}}{\partial \left(\hat{\underline{n}}_{ij} \cdot \underline{x}\right)} &= \underline{0} \\ \underline{w}\left(\hat{\underline{n}}_{ij} \cdot \underline{x}, t\right)\big|_{t=t_0} &= \begin{cases} \underline{w}_i\,, & \hat{\underline{n}}_{ij} \cdot \underline{x} < 0 \\ \underline{w}_j\,, & \hat{\underline{n}}_{ij} \cdot \underline{x} > 0 \end{cases} \end{aligned}\right\} \tag{3.55}$$

is solved with considerably less effort.

It is left to find the Roe-type linearization $\breve{\underline{\underline{A}}}$ of the general EoS Jacobian introduced in section 3.1.3.4. For the discussion it is convenient to define an auxiliary vector $\underline{q}$ containing all explicitly occurring terms of the Jacobian matrix (3.38)

$$\underline{q}\left(\underline{w}\right) \coloneqq \left(\underline{u}, H, \partial_{\underline{w}}\, \Pi\right). \tag{3.56}$$

With this definitions, the Jacobian matrix may be equally given by

$$\underline{\underline{A}}\left(\underline{q}\left(\underline{w}_i\right), \underline{q}\left(\underline{w}_j\right), \hat{\underline{n}}_{ij}\right). \tag{3.57}$$

For an ideal gas, $\underline{q}$ reduces to

$$\underline{q}^{\mathrm{IG}}\left(\underline{w}\right) \coloneqq \left(\underline{u}, H\right). \tag{3.58}$$

For this simplified ideal gas system, Roe [148] constructs $\breve{\underline{\underline{A}}}^{\mathrm{IG}}$ utilizing a parameter vector, of which both, the flux vector $\hat{\underline{n}} \cdot \underline{\underline{F}}^{a,\mathrm{IG}}$ and the vector of the conservative variables $\underline{w}$, are homogeneous quadratic functions; see also [57, 97, 181]. With the parameter vector (3.58) a Roe-averaged, intermediate state $\breve{\underline{w}}^{\mathrm{IG}}$ is found, at which the exact Jacobian matrix is evaluated to yield the Roe-type linearization

$$\breve{\underline{\underline{A}}}^{\mathrm{IG}}\left(\underline{w}_i, \underline{w}_j, \hat{\underline{n}}_{ij}\right) = \underline{\underline{A}}^{\mathrm{IG}}\left(\underline{q}^{\mathrm{IG}}\left(\breve{\underline{w}}^{\mathrm{IG}}\left(\underline{w}_i, \underline{w}_j\right)\right), \hat{\underline{n}}_{ij}\right), \tag{3.59}$$

with

$$\underline{q}^{\mathrm{IG}}\left(\breve{\underline{w}}^{IG}\left(\underline{w}_i, \underline{w}_j\right)\right) = \left(\breve{\underline{u}}^{IG}\left(\underline{w}_i, \underline{w}_j\right), \breve{H}^{IG}\left(\underline{w}_i, \underline{w}_j\right)\right). \tag{3.60}$$

I.e., in the ideal gas case, it is sufficient to find Roe-averaged velocity and total enthalpy

$$\breve{\underline{u}}^{\mathrm{IG}}\left(\underline{w}_i, \underline{w}_j\right) \coloneqq \alpha\, \underline{u}_i + (1-\alpha)\, \underline{u}_j \tag{3.61}$$

$$\breve{H}^{IG}\left(\underline{w}_i, \underline{w}_j\right) \coloneqq \alpha\, H_i + (1-\alpha)\, H_j, \tag{3.62}$$

where

$$\alpha := \left(\sqrt{\underline{\varrho}_i} + \sqrt{\underline{\varrho}_j}\right)^{-1} \sqrt{\underline{\varrho}_i}. \tag{3.63}$$

For the general Jacobian (3.38) considered here, the Roe-type linearization is no longer uniquely determined, as the number of explicitly occurring quantities exceeds the number of conditions defining the Roe-type linearization, see eq. (3.56). Furthermore, the construction by a parameter vector is no longer possible, since there generally exists no parameter vector, of which flux vector $\hat{\underline{n}} \cdot \underline{\underline{F}}^a$ and the vector of the conservative variables $\underline{w}$ are homogeneous quadratic functions. Several approaches to generalize the Roe-type linearization to the real gas case have been proposed, see [20, 118] for an overview. Instead of a Roe-averaged state, most approaches define Roe-averaged quantities

$$\breve{\underline{q}}\left(\underline{w}_i, \underline{w}_j\right) := \left(\breve{\underline{u}}, \breve{H}, \partial_{\underline{w}} \breve{\Pi}\right), \tag{3.64}$$

needed to construct the Roe-type linearization $\breve{\underline{\underline{A}}}$. I.e., the averaged quantities $\partial_{\underline{w}} \breve{\Pi}\left(\underline{w}_i, \underline{w}_j\right)$ are no longer the partial derivatives of the pressure function $\Pi\left(\underline{w}\right)$ evaluated at some intermediate state, but additional independent unknowns of the linearization process [20]. The schemes based on that approach have been proven successful in the computation of chemically reacting hypersonic flows [60] and in different real gas applications. However, a drawback lies in the fact that the intermediate quantities $\breve{\underline{q}}$ are artificial unknowns without thermodynamic significance. This may lead to inconsistencies whenever these quantities are employed to derive other thermodynamic variables such as the speed of sound. Especially in two-phase flows, these approaches may lead to a non-hyperbolic Roe-type linearization [182].

To overcome this shortcoming, the approach due to [20] that is based on the idea presented in [60] is followed here. In analogy to the ideal gas case (3.59), a Roe-averaged state is searched such that the partial derivatives are now considered to be dependent unknowns evaluated at the intermediate state

$$\underline{q}\left(\breve{\underline{w}}\left(\underline{w}_i, \underline{w}_j\right)\right) := \left(\breve{\underline{u}}, \breve{H}, \partial_{\underline{w}} \Pi\left(\breve{\underline{w}}\right)\right). \tag{3.65}$$

The Roe-averaged state is constructed by direct substitution into eq. (3.53). Defining $\Delta\left(\bullet\right) := \left(\bullet\right)_j - \left(\bullet\right)_i$ and $\underline{\underline{F}}^a{}_i := \underline{\underline{F}}^a\left(\underline{w}_i\right)$ and introducing eq. (3.65) yields following underdetermined system of equations

$$\hat{\underline{n}}_{ij} \cdot \Delta \underline{\underline{F}}^a = \underline{\underline{A}}\left(\underline{q}\left(\breve{\underline{w}}\left(\underline{w}_i, \underline{w}_j\right)\right), \hat{\underline{n}}_{ij}\right) \cdot \Delta \underline{w}, \tag{3.66}$$

defining the Roe-averaged state. As the mass conservation equation reduces to unity, we are left with only two equations. To construct a Roe-averaged

state, additional constrains must be defined to close the system. As it is desired that the Roe-average for the general system reduces naturally to the ideal gas case, the obvious choice is to require

$$\begin{aligned} \breve{\underline{u}} &\coloneqq \breve{\underline{u}}^{\mathrm{IG}} \\ \breve{H} &\coloneqq \breve{H}^{IG}, \end{aligned} \tag{3.67}$$

which yields the additional pressure constraint

$$\Delta p = \partial_{\underline{w}} \Pi \left(\breve{\underline{w}} \right) \cdot \Delta \underline{w}. \tag{3.68}$$

The actual number of constraints that have to be defined additionally in order to satisfy eq. (3.68) depends on the choice of the pressure equation of state. As expected, eq. (3.68) reduces to unity in the ideal gas case.

For the EoS $p = p\left(\varrho, e\right)$, the additional pressure constraint (3.68) yields

$$\Delta p = \partial_{\varrho} p \left(\breve{\varrho}, \breve{e} \right) \, \Delta \varrho - \breve{\varrho}^{-1} \, \partial_{e} p \left(\breve{\varrho}, \breve{e} \right) \left(\Delta \left(\varrho e \right) - \breve{e} \Delta \varrho \right). \tag{3.69}$$

Further assuming

$$\Delta \left(\varrho \, e \right) \coloneqq \breve{\varrho} \, \Delta e + \breve{e} \, \Delta \varrho, \tag{3.70}$$

as in [102], satisfied by

$$\breve{\varrho} \left(\underline{w}_i, \underline{w}_j \right) \coloneqq \sqrt{\varrho_i \, \varrho_j} \tag{3.71}$$

$$\breve{e} \left(\underline{w}_i, \underline{w}_j \right) \coloneqq \alpha \, e_i + \left(1 - \alpha \right) e_j, \tag{3.72}$$

the additional pressure constraint (3.68) holds if the pressure equation of state satisfies

$$\Delta p = \partial_{\varrho} p \left(\breve{\varrho}, \breve{e} \right) \, \Delta \varrho - \partial_{e} p \left(\breve{\varrho}, \breve{e} \right) \Delta e. \tag{3.73}$$

However, a Taylor series expansion reveals that the general equation of state $p = p\left(\varrho, e\right)$ satisfies eq. (3.73) only to within $\mathcal{O}\left(\left\| \Delta \underline{w} \right\|^2 \right)$ [20]. In order to satisfy eq. (3.73), [102] proposes a projection step over the straight line, which, however, might not yield a physically consistent state for a two-phase flow [102]. This further motivates following the procedure suggested in [20] that proposes to omit this projection step. This enhances the overall performance and, in a 2nd order scheme, the introduced error reduces to $\mathcal{O}\left(\delta x^6 \right)$ with the mesh size δx. Furthermore, this ensures that the Roe-type like linearization reduces naturally to the ideal gas case.

The described linearization is not truly a Roe-type linearization as condition (3.53) is generally not satisfied, but the results in [20] indicate that the accepted error does not significantly affect the computational results. To prevent the resolution of nonphysical solutions, the entropy fix due to Harten

and Hyman [62] is implemented. Finally, the numerical flux vector of the presented Roe-type scheme is given by

$$\underline{\Phi}^{\mathrm{Roe}}\left(\underline{w}_i, \underline{w}_j, \underline{\hat{n}}_{ij}\right) = \frac{1}{2}\left(\underline{\hat{n}}_{ij} \cdot \left(\underline{\underline{F}}^a\left(\underline{w}_i\right) + \underline{\underline{F}}^a\left(\underline{w}_j\right)\right) - \left|\breve{\underline{\underline{A}}}\left(\underline{w}_i, \underline{w}_j, \underline{\hat{n}}_{ij}\right)\right| \cdot \Delta\underline{w}\right), \quad (3.74)$$

where

$$\left|\breve{\underline{\underline{A}}}\right| := \breve{\underline{\underline{R}}}\left|\breve{\underline{\underline{\Lambda}}}\right|\breve{\underline{\underline{R}}}^{-1}, \quad (3.75)$$

with corrected Eigenvalues, see [12, 69, 181]. The Roe-averaged speed of sound is for consistency and in difference to [20] calculated with the Roe-averaged pressure $\breve{p} := p\left(\breve{\varrho}, \breve{e}\right)$, evaluated directly through the equation of state

$$\breve{a}^2 := a^2\left(\breve{\varrho}, \breve{e}\right) = \partial_\varrho\, p\left(\breve{\varrho}, \breve{e}\right) + \breve{\varrho}^{-2}\, p\left(\breve{\varrho}, \breve{e}\right)\, \partial_e\, p\left(\breve{\varrho}, \breve{e}\right). \quad (3.76)$$

The presented Roe-type scheme for real gas flows is implemented in the FVM solver. Applying the MUSCL reconstruction, the presented flux can be extended to 2nd order accuracy. For the FDM solver, WENO schemes are applied to achieve even higher order, as presented in the next section.

3.1.3.6 WENO schemes

For the FDM solver, different 5th order accurate conservative finite difference WENO (standard WENO-JS [77]) schemes are implemented to provide a high order upwind flux. Used by default is the characteristic-wise Roe-type implementation with entropy and carbuncle fixes for minimal numerical dissipation, as described in detail in [161].

The used implementation follows the derivation in [78], shown here initially for the characteristic-wise flux splitting version in $\hat{n}$ direction

$$\begin{aligned}\underline{\Phi}^{\mathrm{WENO}}_{i+1/2}\left(\underline{\hat{n}}, \dots\right) = 1/12\left(-\underline{f}_{i-1,\underline{\hat{n}}} + 7\underline{f}_{i,\underline{\hat{n}}} + 7\underline{f}_{i+1,\underline{\hat{n}}} - \underline{f}_{i+2,\underline{\hat{n}}}\right) \\ + \underline{\underline{R}}_{i+1/2,\underline{\hat{n}}} \cdot \left(-\varphi_N\left(\Delta\underline{g}^+_{i-3/2,\underline{\hat{n}}}, \Delta\underline{g}^+_{i-1/2,\underline{\hat{n}}}, \Delta\underline{g}^+_{i+1/2,\underline{\hat{n}}}, \Delta\underline{g}^+_{i+3/2,\underline{\hat{n}}}\right)\right. \\ \left. + \varphi_N\left(\Delta\underline{g}^-_{i+5/2,\underline{\hat{n}}}, \Delta\underline{g}^-_{i+3/2,\underline{\hat{n}}}, \Delta\underline{g}^-_{i+1/2,\underline{\hat{n}}}, \Delta\underline{g}^-_{i-1/2,\underline{\hat{n}}}\right)\right), \end{aligned} \quad (3.77)$$

with

$$\underline{f}_{i,\underline{\hat{n}}} := \underline{\hat{n}} \cdot \underline{\underline{F}}^a\left(\underline{w}_i\right), \quad (3.78)$$

$$\varphi_N\left(a, b, c, d\right) := 1/3\omega_0\left(a - 2b + c\right) = 1/6\left(\omega_2 - 1/2\right)\left(b - 2c + d\right) \quad (3.79)$$

and the weights ω_0 and ω_2 given in [78]. The splitted flux differences in characteristic space

$$\Delta \underline{g}^{\pm}_{i+1/2,\underline{\hat{n}}} = \underline{\underline{R}}^{-1}_{i+1/2,\underline{\hat{n}}} \cdot \left(\underline{f}^{\pm}_{i+1,\underline{\hat{n}}} - \underline{f}^{\pm}_{i-1,\underline{\hat{n}}} \right) \tag{3.80}$$

are projected based on the left eigenvectors $\underline{\underline{R}}^{-1}_{i+1/2,\underline{\hat{n}}} = \underline{\underline{R}}^{-1}\left(\underline{w}_{i+1/2}, \underline{\hat{n}}\right)$, evaluated at the Roe-averaged face state $\underline{w}_{i+1/2}$ (using a simple mean is also possible and currently used for real gas). The derivation of the Eigendecompositon of the real gas Jacobian matrix is presented in section 3.1.3.4. The split-fluxes

$$\underline{f}^{\pm}_{i,\underline{\hat{n}}} = 1/2 \left(\underline{f}_{i,\underline{\hat{n}}} \pm \underline{\hat{\lambda}}_{i,\underline{\hat{n}}} \cdot \underline{w}_i \right), \quad \underline{\hat{\lambda}}_{i,\underline{\hat{n}}} = \hat{\lambda}^{(s)}_{i,\underline{\hat{n}}} \delta_{sj} \tag{3.81}$$

are either computed by the global Lax-Friedrichs flux splitting (LF)

$$\hat{\lambda}^{(s)}_{i,\underline{\hat{n}}} = \max_{0 \leq \alpha \leq N} \left| \lambda^{(s)}_{\alpha,\underline{\hat{n}}} \right|, \tag{3.82}$$

with the s-th eigenvalue $\lambda^{(s)}_{\underline{\hat{n}}}$ of the flux Jacobian, or the local Lax-Friedrichs flux splitting (LLF)

$$\hat{\lambda}^{(s)}_{i,\underline{\hat{n}}} = \max_{i-2 \leq \alpha \leq i+3} \left| \lambda^{(s)}_{\alpha,\underline{\hat{n}}} \right|. \tag{3.83}$$

The Roe-type implementation does not use splitted fluxes but selects the upwind stencil based on the respective eigenvalue

$$\begin{aligned} &\underline{\Phi}^{\mathrm{WENO-Roe}}_{i+1/2}\left(\underline{\hat{n}}, \dots\right) = \\ &\qquad 1/12 \left(-\underline{f}_{i-1,\underline{\hat{n}}} + 7\underline{f}_{i,\underline{\hat{n}}} + 7\underline{f}_{i+1,\underline{\hat{n}}} - \underline{f}_{i+2,\underline{\hat{n}}} \right) + \sum_{s=1}^{5} \underline{r}^{(s)}_{i+1/2,\underline{\hat{n}}} \\ &\begin{cases} -\varphi_N \left(\Delta g^{(s)}_{i-3/2,\underline{\hat{n}}}, \Delta g^{(s)}_{i-1/2,\underline{\hat{n}}}, \Delta g^{(s)}_{i+1/2,\underline{\hat{n}}}, \Delta g^{(s)}_{i+3/2,\underline{\hat{n}}} \right) & \text{if } \lambda^{(s)}_{i+1/2,\underline{\hat{n}}} < 0 \\ \varphi_N \left(\Delta g^{(s)}_{i+5/2,\underline{\hat{n}}}, \Delta g^{(s)}_{i+3/2,\underline{\hat{n}}}, \Delta g^{(s)}_{i+1/2,\underline{\hat{n}}}, \Delta g^{(s)}_{i-1/2,\underline{\hat{n}}} \right) & \text{otherwise} \end{cases}. \end{aligned} \tag{3.84}$$

To avoid an entropy violation, the entropy fix due to [162] (algorithm 2.3) is employed, reverting to the local Lax-Friedrichs flux splitting implementation if Eigenvalues change signs at the evaluated interface for the respective component s. Furthermore, the H-correction carbuncle fix of [152] is implemented as described in [142]. The numerical viscosity of the LF splitting is larger than that of the LLF, which is in turn larger than that of the Roe-type leading to increasingly less shock smearing and better overall accuracy [162].

3.2 Time integration

The method of lines approach is adopted in this work, where the spatial discretization and subsequent integration in time are separated. Introducing the spatial discretization into the continuously defined PDE of the underlying IBVP yields semidiscrete equations, eq. (3.7) for the FVM solver and eq. (3.15) for the FDM solver, which are ODEs in time. There are many numerical solution techniques available for solving ODEs, see, e.g., [67]. Generally, explicit and implicit methods can be distinguishing. Explicit methods are only conditionally stable and are thus limited in the allowable time step size, which is for advection dominated compressible flows quite small with the Courant–Friedrichs–Lewy number (CFL number) in $\mathcal{O}(1)$ [67]. The computational costs per iteration is low, since no matrices have to be inverted and the efficient parallelization on GPUs is straightforward. However, the low stability limit will require a large number of time steps compared to implicit methods [67].

For scale resolving simulations like LES and DNS, the acceptable time step sizes to resolve the small scale motion are generally within the stability limit of explicit methods. At the same time, explicit Runge-Kutta schemes allow to achieve arbitrary high order accuracy in time. Therefore, an explicit classic 4^{th} order Runge-Kutta scheme is employ for DNS or LES computations in both solvers, as presented in [67]. A global or a fixed time step is implemented, where the pure Euler time step is always used for real gas flows. For steady state RANS computations, a low-storage Runge-Kutta scheme as presented in [12] is available with local time-stepping. Further speedups are possible with residual smoothing or multi-grid cycles [12], which are not yet implemented, as implicit methods for time integration are also available. However, for the GPU mode, especially the multi-grid approach seems promising for future implementation. URANS computations are conducted based on a dual time-stepping as given in [12]. Dual time-stepping with explicit inner iterations can be efficient, as long as the physical time step does not become too large.

For larger physical time steps in URANS and steady state RANS computations, the implicit Lower-Upper Symmetric-Gauss-Seidel Method (LUSGS) scheme, as presented in [12], is also available for real gas flows. Such implicit methods are generally unconditionally stable and allow thus large time steps. However, the computational costs per iteration is significantly higher compared to explicit methods, since matrices have to be inverted at each time step. This inversion of matrices makes efficient parallelization on multi-thread architectures hard to achieve. The implemented LUSGS scheme offers a comparable low numerical complexity and modest memory requirements com-

pared to other implicit methods. A parallel treatment of the conducted swipes is possible and implemented. However, the performance at block boundaries and other boundary conditions is inferior to the implemented explicit schemes at the moment, as no implicit contributions of the boundary conditions are currently considered. This will be subject of future work; the focus of this work is rather on highly accurate scale resolving computations based on explicit time integration schemes.

Having introduced the full discretization of the governing equations as part of the IBVP to be solved, the last part of the solution scheme is concerned with the treatment of the boundaries, confining the computational domain. This is the subject of the next section.

3.3 Boundary conditions

In this section, the numerical treatment of boundary conditions for real gas flows is described. Here, the focus is on the FVM solver, as the FDM solver currently only contains treatment for periodic and symmetry boundaries. The implementation is based on ghost cells, which are only allocated in memory for the flux computation, as only limited memory is available on the GPU architecture. The boundary treatment for the FVM solver is also based on ghost cells, which are, however, allocated permanently. Solid wall and symmetry treatments are implemented as described in [12] and are only adapted to real gas flows in terms of the choice of variables for the extrapolation to the ghost cells. In the following, a set of simple in- and outlet boundary conditions as well as more sophisticated steady state non-reflecting in- and outlet boundaries for real gas flows are presented. Non-reflecting boundary conditions for transient simulations based on an extension of the Navier-Stokes characteristic boundary conditions (NSCBC) methodology [128, 129] are already implemented in the solver. Details about this development will be published in the future. Specific boundary conditions for turbomachinery computations, like the frozen rotor or mixing plane interface for steady state and the sliding interface for unsteady computations are also implemented.

Only the inversion of flux averages (also called “mixed-out average” [55]) has to be adopted to real gas flows. It denotes the computation of the flux averaged primitive variables $\left(\bar{\varrho}, \bar{u}, \bar{p}\right)$, which represent the fully mixed-out

state, from the flux average

$$\underline{\bar{f}} := \frac{\sum_{i=1}^{N} \left(\hat{\underline{n}} \cdot \underline{\underline{F}}^{a}\left(\underline{w}_i\right) A_i\right)}{\sum_{i=1}^{N} A_i} = \left(\bar{f}_{\varrho}, \underline{\bar{f}}_{\varpi}, \bar{f}_{\epsilon}\right), \tag{3.85}$$

where N is the number of cell faces on the considered surface. This flux average is the theoretically most rigorous averaging method [55] and the only one that guarantees conservativity of the numerical scheme at the respective interface. For a general EoS, the primitive variables may be given in terms of

$$\bar{\varrho} = \frac{\bar{f}_{\varrho}}{\underline{\bar{u}} \cdot \hat{\underline{n}}} \tag{3.86}$$

$$\underline{\bar{u}} = \frac{\underline{\bar{f}}_{\varpi} - \bar{p}\hat{\underline{n}}}{\bar{f}_{\varrho}} \tag{3.87}$$

and the implicit function

$$0 = \bar{f}_{\epsilon} - \bar{\varrho}\underline{\bar{u}} \cdot \hat{\underline{n}}\left(h\left(\bar{\varrho}, \bar{p}\right) + \underline{\bar{u}} \cdot \underline{\bar{u}}/2\right). \tag{3.88}$$

These equations can be combined to following implicit function of the flux averaged pressure

$$0 = \bar{p}^2 - 2\underline{\bar{f}}_{\varpi} \cdot \hat{\underline{n}}\bar{p} + 2\bar{f}_{\varrho}{}^2 h\left(\frac{\bar{f}_{\varrho}{}^2}{\underline{\bar{f}}_{\varpi} \cdot \hat{\underline{n}} - \bar{p}}, \bar{p}\right) + \underline{\bar{f}}_{\varpi} \cdot \underline{\bar{f}}_{\varpi} - 2\bar{f}_{\epsilon}\bar{f}_{\varrho}, \tag{3.89}$$

which generally contains multiple roots. To locate all real valued roots, a complex global root finding algorithm is required; subsequently the correct solution in the thermodynamic sense must be chosen based on the corresponding entropy change with respect to a reference state. This represents a very cumbersome process and the stable and efficient inversion for complex EoS is subject of current research. For an ideal gas, eq. (3.89) reduces to a quadratic function with a subsonic and a supersonic solution

$$\bar{p}_{1,2} = \frac{1}{\gamma + 1}\left(\underline{\bar{f}}_{\varpi} \cdot \hat{\underline{n}} \pm \sqrt{\left(\underline{\bar{f}}_{\varpi} \cdot \hat{\underline{n}}\right)^2 + \left(\gamma^2 - 1\right)\left(\underline{\bar{f}}_{\varpi} \cdot \underline{\bar{f}}_{\varpi}\right) - 2\bar{f}_{\epsilon}\bar{f}_{\varrho}}\right). \tag{3.90}$$

I.e., the flux inversion is only simple for an ideal gas EoS and a robust area average is used for the presented real gas computations at turbomachinery interfaces in this work.

3.3.1 Simple in- and outlet treatment for real gas flows

In order to solve an IBVP for the Navier-Stokes equations with a generalized EoS described in chapter 2, a simple ghost-cell based boundary treatment for in- and outflow boundaries is proposed here. More sophisticated non-reflecting boundary conditions will be described in section 3.3.2.

Objective of the boundary treatment is to determine the ghost-cells' flow states $(\bullet)^o$, such that a certain, user prescribed state on the boundary face $(\bullet)^f$ is maintained. This boundary face state is computed for the cell centered FVM approach by a simple average of the first inner cell's state $(\bullet)^i$ and that of the first ghost cell. I.e., having determined the state on the face $\underline{w_p}^f$, the ghost cell state is computed by a first order extrapolation

$$\underline{w_p}^o := 2\underline{w_p}^f - \underline{w_p}^i,$$

shown here in primitive variables. As for the reconstruction of the MUSCL scheme, instead of the primitive variables, the set $(\varrho, \underline{u}, e)$ or $(\varrho, \underline{u}, T)$ are used for non-ideal gas flows, depending on the underlying state equation. For every characteristic entering the domain a user-defined condition must be imposed on in- and outlet boundary faces [69]. Thus, the in- and outlet boundary treatment depends in the Mach-number regime of the flow through the boundary face, that is determined by an appropriate face-average.

For a subsonic inlet boundary, total pressure ${p_t}^f$, total temperature ${T_t}^f$ and the flow angles

$$\begin{aligned} \tan\alpha &:= \left(\underline{u}^f \cdot \underline{\hat{n}}^f\right)^{-1} \underline{u}^f \cdot \underline{\hat{e}}_\phi \\ \tan\beta &:= \left(\underline{u}^f \cdot \underline{\hat{n}}^f\right)^{-1} \underline{u}^f \cdot \underline{\hat{t}}^f \end{aligned} \tag{3.91}$$

are imposed on the face, with the face-normal $\underline{\hat{n}}^f$, face-tangential $\underline{\hat{t}}^f$ and face-azimuthal $\underline{\hat{e}}_\phi$ unit vectors. Assuming

$$\underline{u}^f \cdot \underline{u}^f \cong \underline{u}^i \cdot \underline{u}^i, \tag{3.92}$$

together with the flow angles (3.91), the velocity on the boundary face $\underline{u}^f$ is determined. Further assuming

$$s^f = s\left({p_t}^f, {T_t}^f\right) \cong s^i, \tag{3.93}$$

the thermodynamic state on the face is determined by

$$\left(h^f, s^f\right), \tag{3.94}$$

where

$$h^f = h\left({p_t}^f, {T_t}^f\right) - \frac{1}{2}\underline{u}^f \cdot \underline{u}^f. \tag{3.95}$$

In the supersonic regime, corresponding to the additional upstream running characteristic, the static pressure p^f is imposed supplementary. Assuming (3.93) holds, the thermodynamic state is determined by

$$\left(p^f, s^f\right). \tag{3.96}$$

With

$$\underline{u}^f \cdot \underline{u}^f = 2\left(h\left({p_t}^f, {T_t}^f\right) - h\left(p^f, s^f\right)\right) \tag{3.97}$$

and the imposed flow angles (3.91), the boundary face velocity $\underline{u}^f$ is determined.

For an outlet boundary in the subsonic regime, the static pressure p^f is prescribed. Assuming

$$s^f \cong s^i, \tag{3.98}$$

the static state on the face is determined by

$$\left(p^f, s^f\right). \tag{3.99}$$

Further assuming

$$H^f \cong H^i, \tag{3.100}$$

the kinetic energy on the boundary face can be computed

$$\underline{u}^f \cdot \underline{u}^f = 2\left(H^f - h\left(p^f, s^f\right)\right). \tag{3.101}$$

To determine the face velocity, the same flow angles as in the internal cell are imposed.

As no characteristics enter the domain through an outlet in the supersonic regime, no condition has to be prescribed and, only in this case, the state is zero-order extrapolated from the interior.

3.3.2 Steady state non-reflecting in- and outlet treatment for real gas flows

In turbomachines, computations must generally be performed on compact domains such that, in contrast to external aerodynamics, generally no undisturbed flow states exist at the boundaries. Therefore, application of standard reflecting boundary conditions may cause spurious, non-physical reflections at the boundaries, which may not only invalidate the calculated flow field but

also result in its dependence on the position of the boundaries. To prevent this, non-reflecting boundary conditions can be applied.

In this work, the steady state non-reflecting boundary treatment of Giles [55, 56], extended by a quasi 3D treatment [155] and with a one-dimensional characteristic reconstruction of boundary face values for cell-centered methods proposed in [147], is adapted to real gas flows. For the general equation of state approach, the inflow boundary treatment must be extended, as presented in the following; the general theory is not repeated here for brevity and can be found in the previously mentioned literature.

The changes of the circumferentially averaged characteristic values are determined by a one-step Newton-Raphson procedure

$$\Delta \underline{c} = - \, \partial \underline{c} / \partial \underline{r} \cdot \underline{r} \, , \tag{3.102}$$

with the residual defined as

$$\underline{r} \coloneqq \begin{pmatrix} p \left(s \left(\varrho, p \right) - s^f \right) \\ \varrho a \left(\underline{u} \cdot \underline{\hat{e}}_y - \underline{u} \cdot \underline{\hat{e}}_x \tan \alpha_\theta^f \right) \\ \varrho a \left(\underline{u} \cdot \underline{\hat{e}}_y - \tan \alpha_r^f \right) \\ \varrho \left(H \left(\varrho, p \right) - H^f \right) \\ \Delta c_5 \end{pmatrix} , \tag{3.103}$$

considering a Cartesian coordinate system and the tangential α_θ and radial α_r flow angles. The boundary face values $(\bullet)^f$ are prescribed. In contrast to the ideal gas case, the entropy $s = s \left(\varrho, p \right)$ is used instead of some entropy related function and the total enthalpy is also treated by means of a general equation of state $H = H \left(\varrho, p \right)$.

Neglecting several terms which are zero in the converged limit [55], the Jacobian matrix in eq. (3.102) reads

$$\frac{\partial \underline{c}}{\partial \underline{r}} = Q^{-1} \begin{pmatrix} -\Gamma_1 Q & 0 & 0 & 0 \\ -\Gamma_1 \Gamma_2 \tan \alpha_\theta^f & -M_y \tan \alpha_\theta^f + Q & -M_z \tan \alpha_\theta^f & \tan \alpha_\theta^f & (\Gamma_3 - \Gamma_2) \tan \alpha_\theta^f \\ -\Gamma_1 \Gamma_2 \tan \alpha_r^f & -M_y \tan \alpha_r^f & -M_z \tan \alpha_r^f + Q & \tan \alpha_r^f & (\Gamma_3 - \Gamma_2) \tan \alpha_r^f \\ -2 \Gamma_1 \Gamma_2 & -2 M_y & -2 M_z & 2 & 2 \left(\Gamma_3 - \Gamma_2 \right) + Q \\ 0 & 0 & 0 & 0 & Q \end{pmatrix} \tag{3.104}$$

where

$$
\begin{aligned}
\Gamma_1 &\coloneqq a^2 \left(p\, \partial_\varrho\, s\left(\varrho, p\right)\big|_p \right)^{-1} \\
\Gamma_2 &\coloneqq \varrho a^{-2}\, \partial_\varrho\, h\left(\varrho, p\right)\big|_p \\
\Gamma_3 &\coloneqq -\varrho\, \partial_p\, h\left(\varrho, p\right)\big|_\varrho \\
Q &\coloneqq \varrho\, \partial_p\, h\left(\varrho, p\right)\big|_\varrho + \Gamma_2 + M_x + M_y \tan\alpha_\theta^f + M_z \tan\alpha_r^f \\
M_{\underline{x}} &\coloneqq \underline{u}/a.
\end{aligned}
\tag{3.105}
$$

For the correction of entropy and enthalpy related perturbations, a similar Newton-Raphson method is applied. The corresponding matrix can be constructed analogously to eq. (3.104) and is omitted here for brevity. The first validation of the presented real gas adaption of the non-reflecting boundary treatment of Giles is presented in [133].

3.4 Validation for scale resolving computations

In the following, the hybrid flux treatment of both solvers, i.e., the 2nd order FV solver and the high order FD solver, is validated for the use in scale resolving computations using test cases as described in [79]. This allows a direct comparison of the results and is efficient due to the coarse grids used. Since the aspired application of the solvers is the investigation of STI, most of the test cases simultaneously involve smooth turbulence as well as sharp discontinuities. The first test case is the one-dimensional Shu-Osher problem containing a well-defined shock wave disturbing a smooth field. Next, essentially incompressible problems with purely smooth broadband turbulence features are considered, with the inviscid Taylor-Green vortex test case for the FD solver and the Comte-Bellot and Corrsin [26] (CBC) experiment of decay of homogeneous isotropic turbulence (DHIT) for the FV solver. Finally, a compressible DHIT with broadband turbulence permeated with eddy shocklets (weak shock waves) is presented for both solvers. The initial validation for real gas applications of the high order FD solver based on adaptions of the presented test cases in the ideal gas limit is given in [134].

3.4.1 Shu-Osher problem

The first test case is the Shu-Osher problem [162], a one-dimensional STI idealization in which a normal shock front propagates into an artificially perturbed density field with $M = 3$. With this test case, the capability of

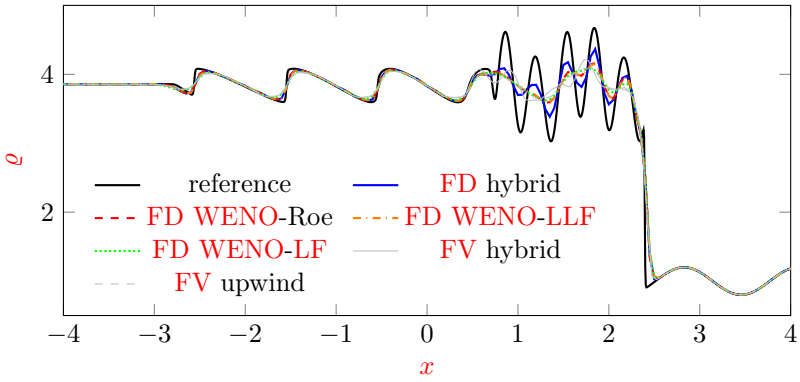

(a) density

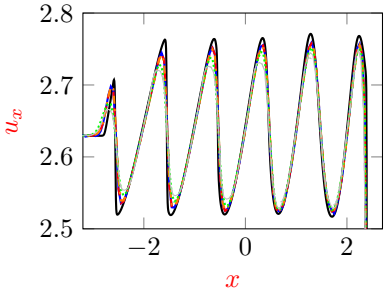

(b) velocity

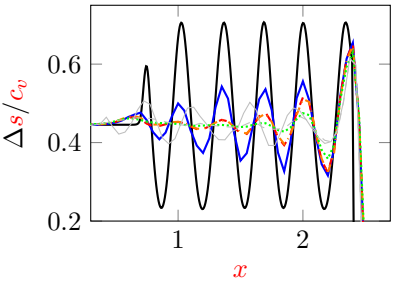

(c) entropy

Figure 3.1: Evaluation for the Shu-Osher problem after $\Delta t = 1.8$ (see also [134])

a solution method to accurately capture a shock wave, its interaction with an unsteady density field and the waves propagating downstream of the shock is tested [79]. The Euler-equations are solved within a domain $x \in [-5, 5]$ with a mesh resolution of $\Delta x = 0.05$ for an ideal gas with $\gamma = 1.4$. The initial state is given by

$$(\varrho, u_x, p) = \begin{cases} (3.857143, 2.629369, 10.33333) & \text{if } x < -4 \\ (1 + 0.2\sin(5x), 0, 1) & \text{otherwise} \end{cases} . \tag{3.106}$$

Figure 3.1 shows the evaluation of density, velocity and entropy change $\Delta s/c_v = \ln(p/\varrho^\gamma)$ after $\Delta t = 1.8$ for hybrid and upwind fluxes within the high order FD and the 2nd order FV solvers. For the FD solver, the WENO im-

plementations with global Lax-Friedrichs (LF) and local Lax-Friedrichs (LLF) flux-splitting and the WENO-Roe implementation with entropy and carbuncle fixes are shown in addition to the hybrid flux, combining the Kennedy and Gruber split form with the WENO-Roe implementation. For the FV solver, hybrid and MUSCL upwind flux results are evaluated. Because this test case is one-dimensional, the default shock sensor is replaced by the shock sensor of Visbal and Gaitonde [186] in both solvers. The reference solution is computed with the FD hybrid flux on a mesh containing 1600 cells and validated against the results given in the original paper [162]. The interaction between the shock wave and the entropy disturbance, as consequence of the disturbed density field, generates acoustic and entropy waves downstream of the moving shock front. This complicates the interpretation of the density plot, which is typically shown for this test case [79]. Therefore, as in [79], entropy and velocity are also shown separately to isolate each family of waves.

All flux formulations in both solvers predict the correct shock position at $x \approx 2.39$ and capture the shock reasonably well. Equally, the location of the contact discontinuity at the leading entropy wave $x \approx 0.69$ and the location of the leading acoustic wave $x \approx -2.75$ [79] are captured in all reported results. Between the contact discontinuity and the shock front, the interpretation of the density distribution is difficult. All upwind methods of FD and FV solvers show similar results. For the hybrid fluxes, in addition to higher dissipation, the FV solver shows signs of dispersion, which is not evident from the FD solver. All results are similar regarding the velocity distribution in this area. The most prominent differences between the results are evident from the entropy wave evaluation. Downstream of the shock, the amplitudes of the entropy waves decrease as they propagate downstream due to the numerical dissipation. For the FD solver, the WENO-LF is more dissipative than WENO-LLF, which nearly matches WENO-Roe. The FD hybrid method is much less dissipative; even better results are reported in [79] using a more elaborate shock sensor. In addition to increased dissipation, the 2^{nd} order FV solver shows for both flux formulation dispersion with respect to the FD solver results. Already this simple one-dimensional test case demonstrates that in addition to an accurate treatment of the shock the properties of the numerical scheme away from the shock matter in order to achieve accurate results in the entire domain [79].

3.4.2 Inviscid Taylor-Green vortex

To assess the effect of dissipation on purely smooth broadband turbulence in absence of shock waves, the inviscid Taylor-Green vortex test case [179] is considered for the FD solver. A similar test case for the FV solver is pre-

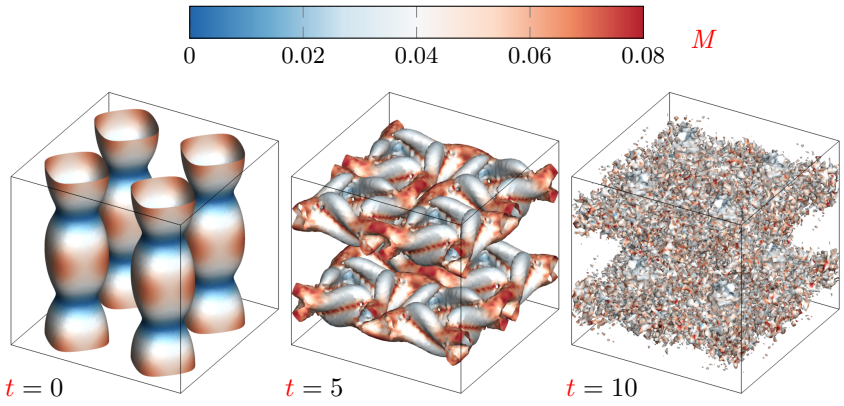

Figure 3.2: Isosurfaces of $p = 99.8$ colored by Mach number for the FD hybrid computation of the inviscid Taylor-Green vortex test case (see also [134])

sented in the next section. The Taylor-Green vortex test case constitutes a non-regularized problem with no lower bound on the length scale [79, 90], where the inviscid vortex begins stretching and producing ever smaller scales, starting from a well-resolved initial condition (see also fig. 3.2). The test case is solved without any regularization other than the numerical method and allows to test the preservation of kinetic energy, enstrophy growth and stability in presence of under-resolved motions [79].

The Euler-equations are solved for an ideal gas with $\gamma = 5/3$ and the periodic domain $[0, 2\pi)^3$ is discretized by a uniform 64^3 grid. The initial condition

$$\begin{aligned} \varrho &= 1 \\ \underline{u} &= \left(\sin x \cos y \cos z, -\cos x \sin y \cos z, 0\right) \\ p &= 100 + \frac{\left(\cos 2z + 2\right)\left(\cos 2x + \cos 2y\right) - 2}{16} \end{aligned} \tag{3.107}$$

is specified with a sufficiently high mean pressure to make the problem essentially incompressible. This allows a comparison to the semi-analytical results for the enstrophy growth of Brachet et al. [14]. As consequence of the incompressibility, the kinetic energy must remain constant, while the enstropy grows rapidly [79].

The process of vortex breakdown is illustrated in fig. 3.2 showing isosurfaces of pressure colored by the Mach number after $t = (0, 5, 10)$ for the FD solver with hybrid flux treatment. The general regimes through which

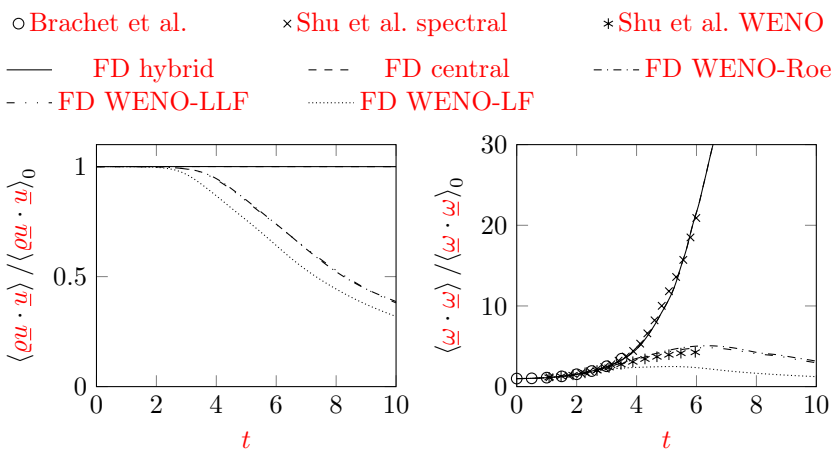

(a) kinetic energy (b) enstrophy

Figure 3.3: Temporal evolution of space averaged quantities for the inviscid Taylor-Green vortex on a 64^3 grid (see also [134])

the flow evolves in time are visible. From the smooth initial conditions at $t = 0$, the structures begin to interact. At $t = 5$ the flow is still laminar-like and dominated by large-scale structures. By $t = 10$, the flow has transitioned to turbulence-like, in which smaller scale structures form due to nonlinear interactions producing a range of length scales in the flow.

The temporal evolution of space averaged kinetic energy and enstrophy is evaluated in fig. 3.3, allowing to assess the influence of the numerical dissipation of the different FD flux treatments for this problem. For the dilatation-based shock sensor of the hybrid scheme to work, the grid for this test case must be chosen carefully, as, e.g., with a grid point located at point $\underline{x} = (0, 0, 0)$ the vorticity in this point is 0 and the shock sensor fails. Therefore, the grid is equally shifted by $\Delta \underline{x}/2$ (alternatively, the shock sensor definition can also be enhanced as proposed in [79]). On this grid, the dilatation-based shock sensor of the FD hybrid scheme never activates the WENO flux, allowing the non-dissipative central scheme to preserve the kinetic energy. The same is evident from the temporal evaluation of the enstrophy, where FD hybrid and central schemes show an identical rapid growth, very similar to the results of Brachet et al. [14]. Furthermore, these schemes also match the spectral (F-SF-23N) results of Shu et al. [163] on the same 64^3 grid. Also, the WENO5 results of [163] are similar to those of the FD WENO-LLF and

WENO-Roe implementations.

All presented FD WENO schemes are certainly stable, but at the expense of a large dissipation that causes depletion of both kinetic energy and enstrophy for $t \gtrsim 2$. At this point, the FD WENO schemes begin to adapt their stencils, which leads to a drastic increase of numerical dissipation [79], where the FD WENO-LF is more dissipative than FD WENO-LLF, which nearly matches the dissipation of the FD WENO-Roe implementation. All FD WENO schemes agree reasonably with the semi-analytical results for the enstrophy growth until $t \approx 3$, where the influence of the numerical dissipation is starting to become evident.

3.4.3 LES of the Comte-Bellot and Corrsin experiment

In this section, the Comte-Bellot and Corrsin (CBC) [26] experiment of decaying homogeneous isotropic turbulence (DHIT) is used as a benchmark test case for the validation of the FV solver for scale resolving computations of smooth turbulence. The spatial decay of relatively large scale isotropic turbulence generated by a mesh of spacing $M = 5.08\,\mathrm{cm}$ at a mean flow velocity $U_0 = 10\,\mathrm{ms}^{-1}$ with a resulting Reynolds number $Re_M = 34\,000$ is studied at three different downstream positions $tU_0/M = 42, 98, 171$. The measurements clearly show the classical integral scales, inertial range and dissipative scales in the spectra of the turbulent kinetic energy [184]. The Taylor-scale Reynolds number decays from $Re_\lambda = 71.6$ to 60.6 between the first and last measurement location.

For the computation, the Taylor hypothesis of frozen turbulence [178] is invoked and the frame of reference is changed to move with the mean flow speed

$$t = \int_0^x \frac{\mathrm{d}x'}{\overline{U}\,(x')}, \tag{3.108}$$

with the downstream grid distance x and the mean flow velocity over the cross-section of the tunnel $\overline{U}\,(x)$. This allows to compare the spatial decay of the experiment to a temporal decay in a stationary computational domain. I.e., it is possible to initialize the problem with the spectrum from the first available upstream location and compare the temporal decay directly to the available spectra at the two downstream positions. Furthermore, for computational convenience, the standard non-dimensionalization [47, 112] for the test case is adopted, scaling velocity $U_\mathrm{ref} = \sqrt{3U'^2_o/2}$, length $L_\mathrm{ref} = L/(2\pi)$ and time $t_\mathrm{ref} = L_\mathrm{ref}/U_\mathrm{ref}$, where $\sqrt{U'^2_o} = 22.2\,\mathrm{cms}^{-1}$ represents the velocity fluctuations at the first measurement position. With $L = 11M$, the numer-

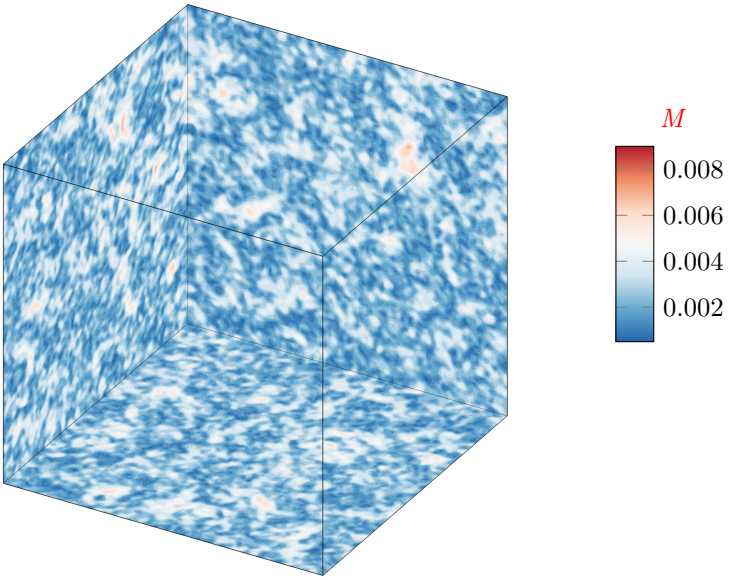

Figure 3.4: Contours of the Mach number after $\Delta t = 2\,\mathrm{s}$ for the CBC test case solved by the FV hybrid scheme on the 128^3 grid

ical domain contains approximately four integral scales [184]. With the first measurement location corresponding to $t_0/t_{\mathrm{ref}} = 0$ the non-dimensional times at second and third measurement locations are $t_1/t_{\mathrm{ref}} = 0.87$ and $t_2/t_{\mathrm{ref}} = 2.0$.

For the CBC test case, the filtered Navier-Stokes equations are solved employing the hybrid flux treatment of the FV solver in a periodic cubic computational domain of equal side length 2π discretized by an equidistant mesh of resolutions 64^3 and 128^3, respectively. Time is integrated with a constant time step of $5 \times 10^{-5}\,\mathrm{s}$, which corresponds to a CFL number below 0.5. The initial divergence free velocity field is generated employing Rogallo's method [149], the Mach number in each cell does not exceed a value of 0.009. All thermodynamic fields are constantly initialized. In addition to an ideal gas, overheated steam is considered. As the test case is essentially incompressible, velocity and thermodynamic fields are not strongly coupled and results should be independent of the underlying state equation in the considered range. The contours of the resulting Mach number after $\Delta t = 2\,\mathrm{s}$ for the 128^3 test case are shown in fig. 3.4.

The evaluation of the energy spectrum for the 64^3 setup is shown in fig. 3.5.

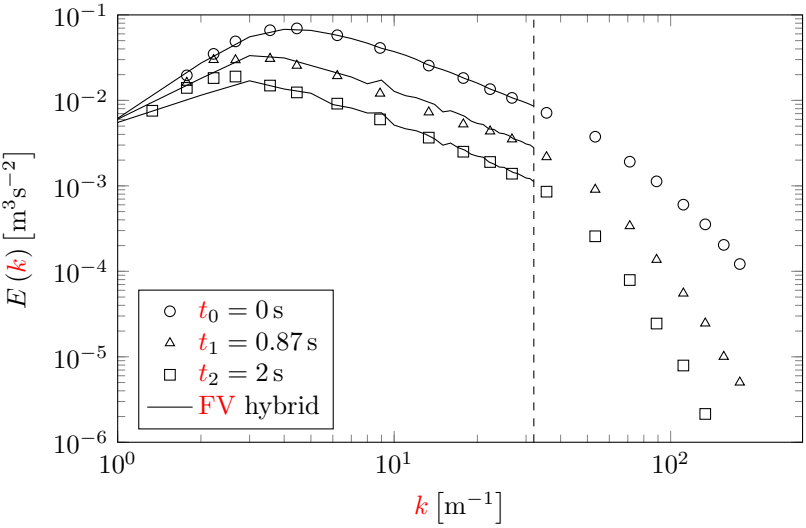

Figure 3.5: Evaluation of the energy spectrum for the CBC test case with 64^3 cells (see also [136])

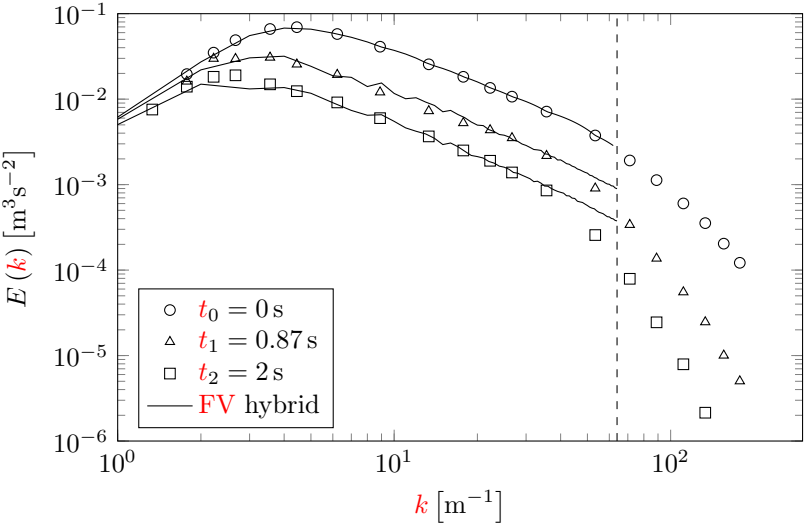

Figure 3.6: Evaluation of the energy spectrum for the CBC test case with 128^3 cells (see also [136])

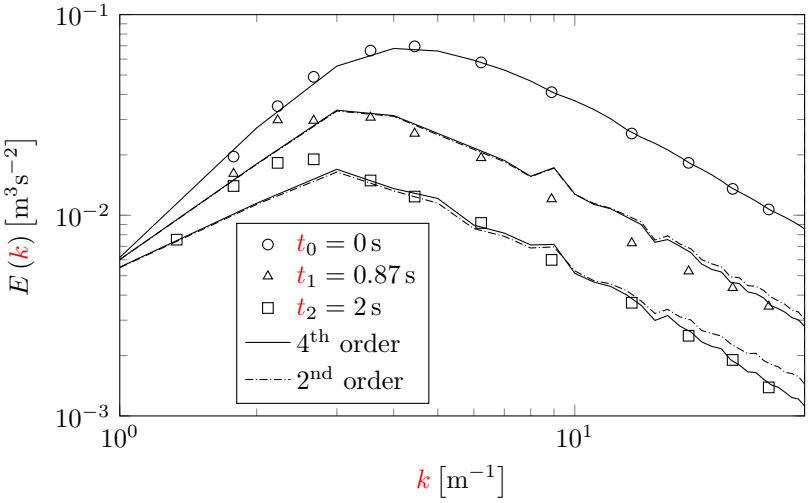

Figure 3.7: Influence of the time integration scheme on the computed energy spectrum of the CBC test case with 64^3 cells for the FV hybrid solution scheme (see also [136])

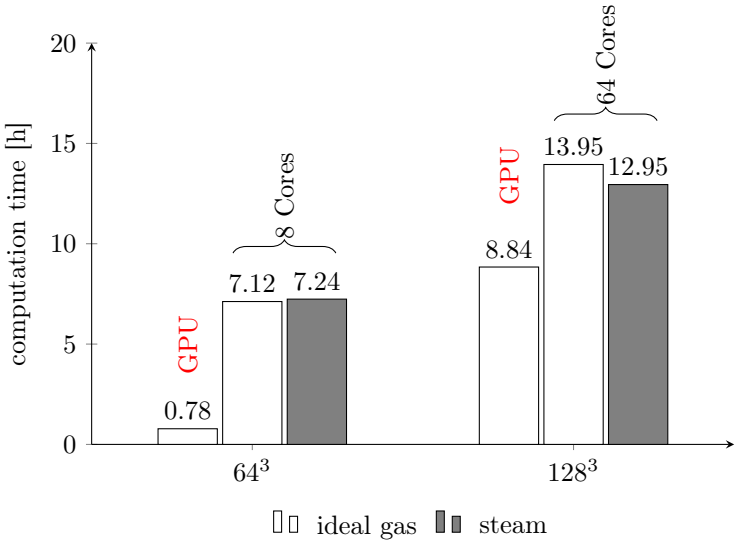

Figure 3.8: Evaluation of the computational speed of the CBC LES computations with the FV hybrid scheme (see also [136])

On this grid, the spectrum until wave number 32 can be resolved, as indicated by the dashed line. Ideal gas and steam computations give identical results, matching the experimental data over the whole inertial range. This demonstrates that the FV hybrid flux implementation does not suffer from excessive numerical damping like standard upwind schemes, rendering the FV implementation applicable for scale resolving LES computations of smooth turbulence. The same evaluation for the 128^3 grid is presented in fig. 3.6, where the cutoff is already resided in the dissipation range. Thus, the highest resolved wave numbers of the computations cannot match the measurements accurately (cf. [131]). The influence of the time integration scheme is evaluated in fig. 3.7, comparing results of 4th and 2nd order Runge-Kutta implementations for the FV solver. The measurements are much better matched with the higher order Runge-Kutta scheme, while the 2nd order implementation shows the result of numerical dispersion.

Finally, an evaluation of the computational speed for the conducted LES computations with the FV solver and the hybrid scheme on a workstation GPU and a standard CPU based cluster is presented in fig. 3.8. The 64^3 test case takes about 47 minutes on the GPU compared to over 7 hours on 8 CPU cores. For the 128^3 grid about 14 hours on 64 CPU cores is matched by only 9 hours on the workstation GPU. This reveals the great potential of the GPU architecture for high performance computing. Comparing steam and ideal gas computations, it can bee seen that for the hybrid flux treatment the overhead of the real gas equation of state is even further reduced, as no extra thermodynamic evaluation is necessary in the flux computation. For the 128^3 setup the SBTL steam computation even appears to be faster, however this might be due to operating conditions of the cluster.

3.4.4 Decay of homogeneous isotropic turbulence with shocklets

The final test case is the compressible DHIT setup of [79]. The turbulent Mach number

$$M_t = \sqrt{\langle \underline{u} \cdot \underline{u} \rangle} / \langle a \rangle \tag{3.109}$$

is chosen sufficiently high that eddy shocklets [92] (weak shock waves) develop spontaneously from the turbulent motions. In this way, the test case represents a combination of the previously considered tests, as it contains smooth turbulent regions permeated with randomly distributed shocks.

The periodic domain $[0, 2\pi)^3$ is discretized by a uniform 64^3 grid. The Navier-Stokes equations are solved for an ideal gas with $\gamma = 1.4$ and $Pr = 0.71$. The viscosity is assumed to follow a power-law (2.37) with $n = 3/4$,

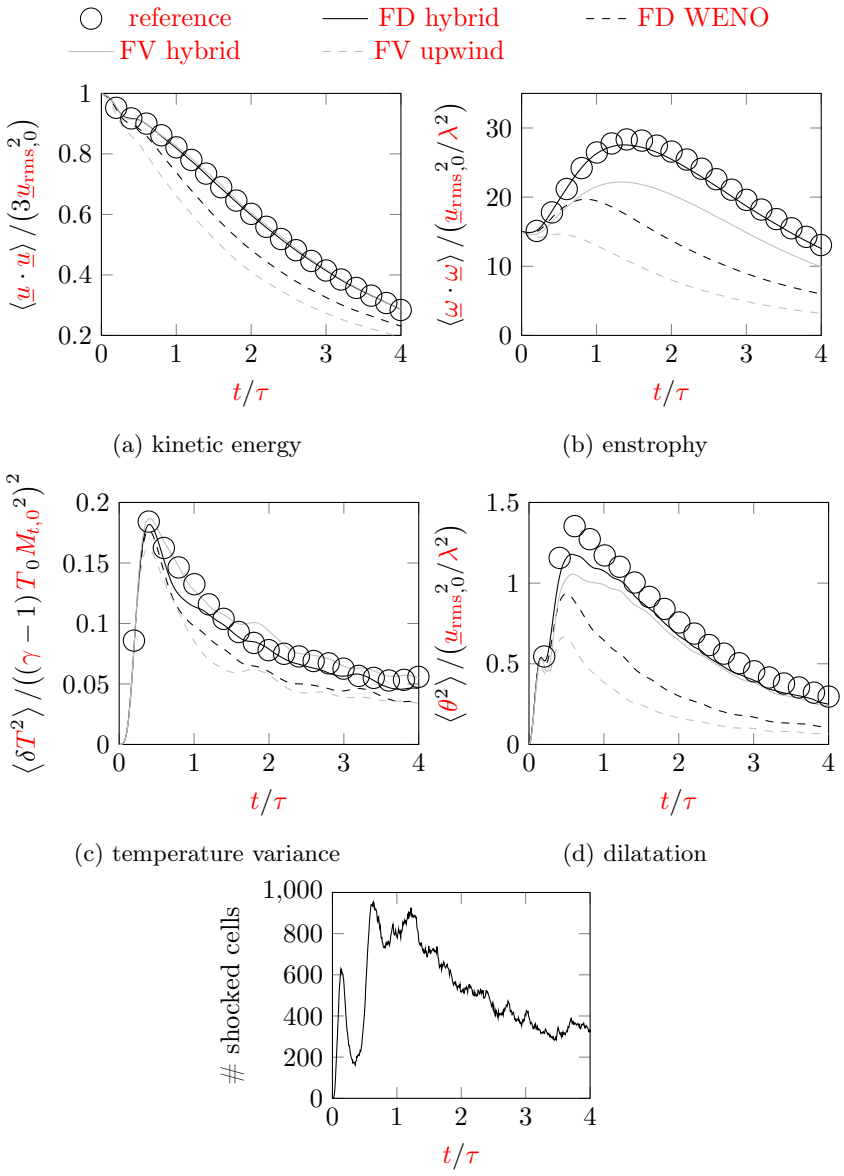

(a) kinetic energy

(b) enstrophy

(c) temperature variance

(d) dilatation

(e) number of cells with $\chi > 0.65$

Figure 3.9: Temporal evolution of mean quantities for the compressible DHIT test case on a 64^3 grid; reference are DNS results of [79] (see also [134, 137])

where the reference state is specified to yield an initial turbulent Mach number $M_{t,0} = 0.6$ and an initial Taylor-scale Reynolds number $Re_{\lambda,0} = 100$. The Taylor-scale Reynolds number

$$Re_\lambda = \langle \varrho \rangle \, \underline{u}_{\mathrm{rms}} \lambda / \langle \mu \rangle \tag{3.110}$$

is based on Taylor microscale

$$\lambda^2 = \left\langle {u_x}^2 \right\rangle / \left\langle \left(\partial u_x / \partial x \right)^2 \right\rangle \tag{3.111}$$

and root mean square (RMS) velocity

$$\underline{u}_{\mathrm{rms}} = \sqrt{\langle \underline{u} \cdot \underline{u} \rangle / 3}. \tag{3.112}$$

The initial velocity field is purely solenoidal and generated with the algorithm detailed in the appendix of [79], randomizing velocity components in the frequency domain to match the prescribed energy spectrum

$$E(k) \sim k^4 \exp\left(-2 \left(k/k_0 \right)^2 \right), \tag{3.113}$$

with the most energetic wave number $k_0 = 4$, which yields $\lambda_0 = 2/k_0$. Initial density and pressure fields are constant so that the initial conditions are not in acoustic equilibrium. Consequently, a field of background acoustic waves and entropy modes develop and persist throughout the simulation [79]. These large acoustic and entropy modes are desirable for testing the robustness of numerical schemes.

The temporal evolution of different mean quantities in reference to a DNS result on a 256^3 grid of [79] is evaluated in fig. 3.9 for hybrid and upwind fluxes of FV and FD solvers. The time is non-dimensionalized by the eddy turn-over time

$$\tau = \lambda_0 / \underline{u}_{\mathrm{rms},0}. \tag{3.114}$$

The minimally dissipative hybrid high order FD method agrees reasonably well with the reference solution for all quantities; slight deviations are only found in temperature variance and dilatation and may be a result of deviating initial velocity fields, which cannot be reproduced exactly due to the random nature of the generation process. The 2nd order FV solver matches the decay in kinetic energy and the temporal evolution of temperature variance and dilatation in similar quality. The evolution of the enstrophy cannot be matched by the FV solver as accurately as by the high order FD solver, which is typical for lower order solution schemes. Overall, both hybrid flux implementations show low dissipation properties and reproduce the DNS results reasonably, qualifying their use in scale resolving computations.

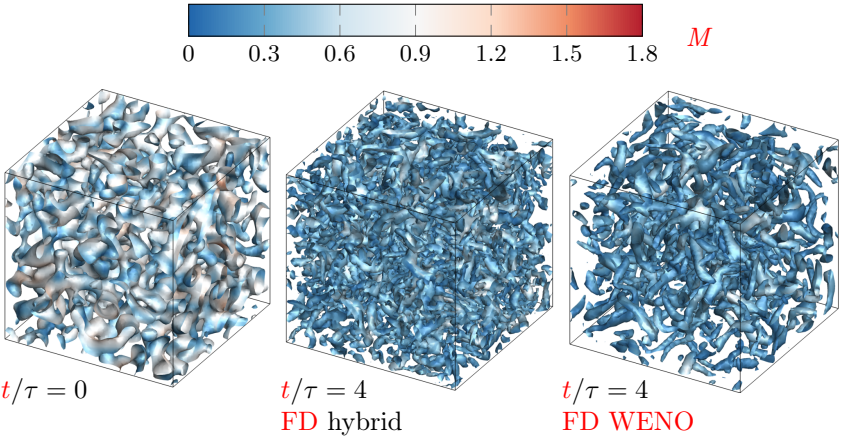

Figure 3.10: Isosurfaces of Q-criteria with 1×10^5 colored by the Mach number for the compressible DHIT test case (see also [134])

This is not the case for upwind schemes. Even the high order FD WENO implementation underpredicts all quantities compared to the reference, revealing its dissipative nature for broadband motions in smooth turbulence. It particularly underpredicts enstrophy and dilatation, which is consistent with the fact that the WENO procedure damps the small-scale motions [79]. This effect is also evident from fig. 3.10 showing Q-criteria isosurfaces colored by the Mach number of the initial field as well as FD hybrid and FD WENO scheme results after $t/\lambda = 4$ in comparison, where the smallest scales are only present in the hybrid results. The 2$^{\text{nd}}$ order FV MUSCL upwind scheme is even more dissipative for all evaluated quantities, as expected. Still, the presented upwind results are reasonable and reproduce the results reported in [79, 90]. The dissipative character of upwind schemes regardless of their order is well known [47], rendering standard shock-capturing schemes even of high order inappropriate for scale resolving computations.

4 Wet Steam Applications

I wish to God these calculations had been executed by steam.

Charles Babbage, English mathematician, 1821
(checking calculations for improving tables
for a navigational book, and disappointed
by numerous errors in these calculations)

Most of the world's power is generated by steam-driven turbines. The steam is typically expanded in three stages, from high to intermediate to low pressure turbines. During this expansion process, the steam cools down and at some point, typically in the low pressure turbine stages, condensation takes place with severe negative effects on the machine. Despite the importance of the steam turbine, very little attention is paid to understanding and accurately predicting the very complex flow behavior inside the low pressure stages in comparison with other prime movers [63]. In gas turbines, considerable progress in investigation and understanding of flow pattern has been made driven by their application in the aeronautical field. These findings, though, are only applicable to the dry stages in steam turbines [63]. In steam turbines, however, the wet low pressure stages are of particular interest, as the largest portion of power along the machine is transformed here, while additional losses occur due to the condensation process and the resulting presence of the second phase. It is well acknowledged that the nucleating and wet stages in steam turbines are less efficient compared to the dry stages running with superheated steam [63].

In recent years, work in wet steam research has gained interest with the advent of high performance computing machines and enhanced measurement techniques [63]. The interest is fueled by the need for more efficient steam turbines, to reduce, e.g., CO_2 emissions, and due to increasingly stringent requirements regarding their flexible operation in modern power grids. The modeling of non-equilibrium condensing steam flows has been ongoing for several decades [51] and allowed some progress in understanding the influences of the phase change on the steam turbine's flow field, where especially flow angles and shock wave structures are altered and a variety of

complex, unsteady phenomena can occur. However, the recent International Wet Steam Modeling Project [171] has revealed that yet no common modeling standard has emerged and it is currently not possible to achieve reasonable agreement with experimental data over the entire range of available test cases and possible operating conditions. I.e., no method is currently available for accurately predicting wetness losses within steam turbines and, because the condensation related phenomena are not yet well understood, improved designs with reduced security margins are prevented.

The formation and behavior of the condensing droplets have important thermodynamic and aerodynamic consequences lowering the performance of the wet steam stages. However, the scatter in results of modern wet steam codes is remarkable [171] and consequence of a multitude of modeling approaches to the description of wet steam flows, described in section 2.3. As indicated in fig. 2.4, the wet steam flow model consists of different submodels and their interaction, modeling the condensation process, the condensed second phase and turbulence. The wide spread behavior of different state equations in the metastable region [159] adds another uncertainty, rendering it especially difficult to operate a clear distinction among the effects of physical approximations and numerical implementations. In this work, the influence of turbulence modeling approach on the quality of the overall wet steam modeling is investigated for the first time employing scale resolving simulation techniques in the field of wet steam flows.

These high quality numerical techniques are highly relevant for modern machine design, as the technological relevance of steam flows renders the ability of accurately forecasting their flow behavior in technical devices of paramount importance. This holds especially in off-design operation, where changes in the operating point are known to have a very substantial impact on wetness losses. In some turbine stages, dramatic reductions in efficiency under certain conditions are exhibited. The reason for this appears to stem from the impact of the heat release, caused by the condensation process, upon blade aerodynamics, which might be reduced with appropriate numerical tools.

A very efficient approach to real gas thermodynamics, as only provided by accurate tabulation techniques, is a basic condition to very involved scale resolving computations. In this work, this is achieved by computing the thermodynamic properties of H_2O using the SBTL [87, 89] method, see section 2.1.1.2 and section 2.3.2. This tabulation approach is optimized for the employed density-based solution methods and its potential for conspicuous savings in CPU time is shown for standard 3D RANS as well as LES computations in this chapter.

After a brief literature review, the implemented wet steam models are cal-

ibrated and validated showing results for typical nozzle test cases. On this basis, the numerical method is applied to a steam turbine cascade flow, showing conventional RANS results. Finally, the first scale resolving LES computation in the field of wet steam flows is presented. The quality of the LES results are assessed in comparison to RANS and URANS results. The influence of the turbulence modeling approach onto the overall wet steam model is also analyzed.

4.1 Literature review

First experimental investigations in the thermodynamics of the condensation process date back to the 1880s. In 1881, Aitken [2] observed that dust or salt particles present during the expansion of saturated air promote the condensation process as "centers of condensation". A similar study was carried out by von Helmholtz in 1886 [64]. In 1897, Wilson [199] made a detailed study of spontaneous condensation. He found that the absence of ions or foreign particles during the expansion of saturated air caused a delay of the condensation process and introduced the supersaturation S as a measure of the departure from thermodynamic equilibrium during the condensation process.

In 1913, Henderson [65] confirmed this observation in steam nozzle experiments, with an approximately $5\,\%$ greater wet steam region in the Mollier diagram compared to equilibrium. In 1915, Steam nozzle experiments were also conducted by Stodola [174] and a thorough discussion of supersaturation effects in nozzles was first given by Callender [17]; this included a prediction of the nucleated droplet sizes based on the Kelvin-Helmholtz equation. On this basis, Martin [105] calculated in 1918 the limiting supersaturation line at varying pressures on the assumption that condensation produces always droplets of similar size and plotted this line in a Mollier chart. Such a limiting supersaturation line is termed Wilson line. In the next decade, much research on spontaneous condensation was conducted by Stodola, summarized in his book [173] (in its English translation, this book was a basic reference for engineers working on the first generation of jet propulsion engines in the United States [27]).

Even though the development of the nucleation theory started almost at the same time as the study of condensation [63], significant results where only attained in the late 1930s. Focus was to define the position of the Wilson line more precisely [143, 205, 206] and its dependence on nozzle shape and experimental conditions was revealed. Further accurate measurements of the axial pressure distribution of nucleating flows in Laval nozzles were

conducted by Binnie & Woods [9] and Binnie & Green [10].

The first to combine the nucleation theory with gas dynamics equations was Oswatitsch [121] in 1942, reporting a good agreement with experimental observations. Overall, the development of steam turbines was progressing with remarkable speed and the problems associated with condensation and the resulting presence of liquid droplets were increasing [63]; especially blade erosion caused major problems. However, the introduction of reheat cycles after the Second World War mitigated this problem temporarily [63]. Development and design of larger steam turbines, though, led to much higher steam velocities increasing the impact of erosion and, thus, refueled the interest in wet steam research. A detailed review of the following developments regarding the classical nucleation theory are given in [6].

First numerical models were targeted at one-dimensional computations of condensation processes in Laval nozzles, e.g., [66]. Later, more sophisticated time-accurate numerical solver were presented [61, 164], in which the Eulerian solver of Denton [28] accounts for the droplet growth along the streamlines based on a Lagrangian particle tracking. The polydispersed droplet spectrum was discretized into a certain number of classes, called Spectrum Pruning [70]. The first two-dimensional numerical treatments of condensing flows in turbine cascades based on a steady, inviscid model were presented in the early 1980s, e.g., the Euler-Lagrange approach in [7]. Time-accurate numerical solver were published by [197, 209]. Euler-Euler solver were also developed by several authors, e.g. [172]. The first three-dimensional steady state inviscid computational method was presented in [98], showing already a good agreement with experimental results of a steady, homogeneous condensing turbine cascade.

In a commercial pressure-based solver, [50, 83] present a 3D Euler-Lagrange method for wet steam flows utilizing a virial equation of state for the properties of water and steam. The same authors [51] develop also an Euler-Euler solver capable of homogeneous nucleation employing a single fluid model, used to study a series of Laval nozzles. This method is later extended to QMOM [52]. This Euler-Euler solver is implemented in the commercial flow solver [53], where an extension to a two fluid model is also available [49]. Results of this implementation for condensing nozzle and cascade flows and a simulation of a low-pressure steam turbine are presented in [59].

A density-based wet steam solver is presented in [31] utilizing a local virial equation of state based on IAPWS-IF97. Results of a condensing 2D flow and a 3D flow through the stator of the last stage of a low-pressure turbine are shown. This solver is compared to a commercial solver in [33] and extended to heterogenous condensation in [203] and to a two-fluid model in [202]. Results for a low-pressure turbine stage are presented in [32] and in [34] for

experiments of a nozzle and a cascade. A density-based Euler-Lagrange approach is also published in [36, 37].

The current wet steam modeling standard is reviewed in the International Wet Steam Modeling project [171], showing results for a number of wet steam solution methods currently under development and in use. Results of this work also serve as basis for the following validation of the developed wet steam solution method.

4.2 Nozzle test cases

In this section, the source term model, described in section 2.3.3.2, is validated showing results for prominent nozzle test cases. The source term model is also compared to the mixture model, which is presented in section 2.3.3.1. The initial validation of wet steam methods relies heavily on experimental data obtained from condensing nozzle flows [171], as the flow in nozzles is much simpler than a complex turbine flow whilst providing rates of cooling comparable to condensation in steam turbines. Therefore, nozzles provide the best laboratory simulation of condensation in steam turbines [6]. The general structure of typical nozzle test cases for condensing wet steam flows is described, e.g., in [6, 171].

The ideal nozzle design provides realistic expansion rates, Mach numbers and subcooling conditions as in real turbines in a steady one-dimensional setting, which is easy to use for validation of a numerical method. Even though a vast number of nozzle test cases is provided in literature [6, 170, 208], all have certain deficiencies [171]. In this work, the focus is on low pressure Wilson points as encountered in the low pressure steam turbine test case presented at the and of this chapter. Due to such well-known deficiencies [135, 170, 171], all presented nozzles test cases are affected by boundary layer growth. Therefore, full three-dimensional computations of the original setups need to be conducted, where the boundary layer state in the experiments is also unknown [170, 171]. In order to achieve a direct comparison to the results of various wet steam solver implementations presented in [171], the validation in the present work is based on 3D laminar computations and the same medium meshes (details given in table A1 of [171]), measurement data and scaling of the plots are used. Results of quasi three-dimensional (q3D) calculations are also presented as in [135] to compare both implemented wet steam models. Furthermore, it is important to keep in mind that the accuracy of the radius distribution measurements lies within about $\pm 20\,\%$ [171] as indicated by error bars in the plots if no more detailed information is given in the original sources. All computations are conducted applying the AUSM+

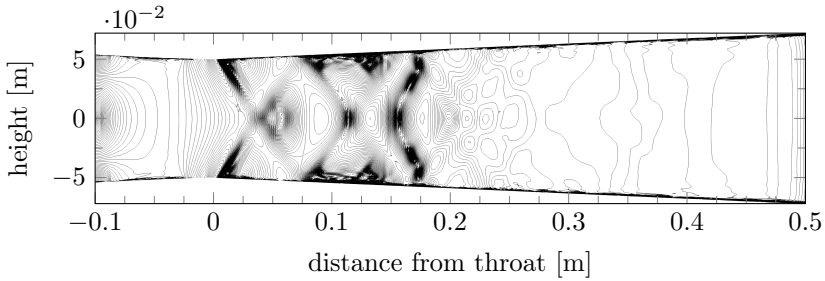

Figure 4.1: Isolines of the density gradient magnitude for the Moore et al. nozzle B based on a 3D laminar calculation

and implicit LUSGS schemes. More details are given in [135, 136].

4.2.1 Moore et al. nozzle B

Moore et al. [116] presented pressure and Sauter mean droplet radius measurements for a series of four different nozzle geometries at very low Wilson point pressures of about 0.1 bar. The pressure was measured at the plane side walls using taps, the Sauter radius at one location on the center line near the outlet with the light extinction method. Even though these radius measurements are of high quality [208], the accuracy can be estimated to be within $\pm 20\,\%$ [171]. All nozzle geometries contain a curvature discontinuity in the throat due to blending between different profiles for the convergent and divergent parts. This generates a series of expansion waves in the throat that are reflected at the opposite wall as "compression waves", as can bee seen for the nozzle B configuration in fig. 4.1. The resulting pattern of waves are visible in center plane data and potentially interfere with the condensation zone. Despite this significant drawback, the nozzle B configuration is the most commonly used validation test case for wet steam computations and is considered in the following.

The geometry of the nozzle B is shown in fig. 4.1, inlet conditions are given by $p_t = 0.25\,\mathrm{bar}$ and $T_t = 358.1\,\mathrm{K}$. Despite relatively large throat dimensions $(0.1 \times 0.152)\,\mathrm{m}^2$, the flow is significantly affected by boundary layer growth and thus sensitive to boundary layer modeling [170]: boundary layers on the profiled walls influence the wave pattern and thus the pressure fluctuations, while the boundary layers on the plane side wall affect the measured wall pressure. This necessitates involved three-dimensional, boundary resolving computations (demonstrated in the following), not the ideal sce-

nario for validation and tuning of model parameters. Furthermore, due to this fact, the results are also sensitive to the boundary layer states, which are unknown from the available measurement data. The Reynolds number at the throat $Re \approx 4 \times 10^5$ suggests that transition to turbulence is likely to occur [170]; however, standard RANS computations cannot account for transitional effects. Here, wall resolving LES computations provide the potential to shed light, though, computationally very involved due to the high Reynolds numbers and the interaction of strong compressible effects in the high Mach number region and condensation. In principle, the method presented in this work is capable of doing this, and due to the continuously increasing computational power this might be subject of future research.

In the following, a suitable general modeling approach for the wet steam computations presented in this work is determined based on q3D results. On this basis, the influence of the boundary layers and the need for full 3D computations is demonstrated. Finally, the computational method is validated and the computational speed is evaluated. All viscous computations use the medium meshes of [171], for which mesh independent results of all quantities are to be expected. The domain is discretized in the q3D computation by $400 \times 2 \times 101$ points in the full 3D computations by $400 \times 101 \times 101$ points. The inviscid computations are run on the coarse q3D mesh with $250 \times 2 \times 71$ points.

4.2.1.1 Modeling approach selection

To determine, which general modeling approach for wet steam computations is pursued in this work, this section presents q3D Euler results, as presented in [135] based on density-based solver implementations of source term model (SM) and mixture model (MM) in OpenFOAM. In fact, the final implementation of the source term model in the new in-house code was based on the findings presented in this section and further optimized. Furthermore, results based on the spline based table lookup method [87, 89] (SBTL) are compared to Young's 1988 state equation [207] (Y88) in terms of accuracy and computational speed. Generally, the influence of different EoS has not yet been extensively studied [171], the connected uncertainties especially in the metastable region are discussed in section 2.3. The additionally needed properties surface tension, molecular viscosity and thermal conductivity are computed based on IAPWS formulations [190]. All computations are integrated in time with an explicit local time stepping and a fixed CFL number of 1. Convergence is reached well within the conducted 6000 iterations.

Figure 4.2 shows the q3D Euler result for all available combinations of two-phase flow models and state equations in comparison to the experimen-

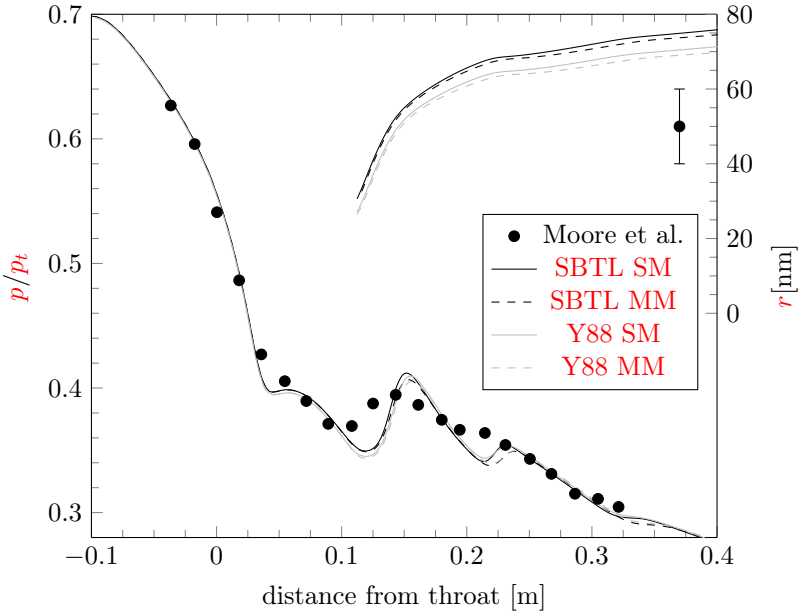

Figure 4.2: q3D Euler results of pressure and droplet radius on the center line for the Moore et al. nozzle B in comparison to measurement data (see also [135])

tal data. Pressure and mean droplet size distributions are evaluated along the center line. Upstream of the throat, the measured pressure distribution is matched by all computations, which yield indistinguishable results. About 0.03 m downstream of the throat, the first pressure fluctuation due to the expansion fan is visible, see also fig. 4.1, and first slight deviations of SBTL and Y88 based results are visible. At circa 0.1 m, the typical pressure rise due to heat release by condensation takes place, however, this pressure rise is predicted by all computations only after another 0.02 m further downstream compared to the measurement. Here, the maximum deviation in pressure due to distinct state equations occurs with a deviation below 200 Pa. Then, the pressure gradient is predicted too steep and the pressure at about 0.15 m is overpredicted by 500 Pa. At about 0.21 m the next pressure fluctuation due to the nozzle discontinuity is present and much more pronounced in the inviscid computations. Here, the pressure is locally underpredicted by about the same 500 Pa as previously overpredicted. Downstream, after about

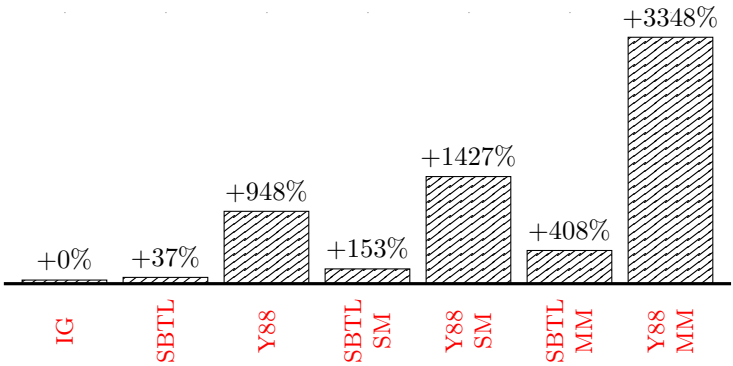

Figure 4.3: Evaluation of the computational speed of q3D Euler computations of the Moore et al. nozzle B, referenced to a corresponding ideal gas (IG) computation (see also [135])

0.25 m distance of throat, the pressure distribution is matched well by all computations. The most notable difference between the two-phase models is evident in the downstream pressure fluctuation at 0.21 m, where the MM predicts the pressure rise slightly more downstream compared to the SM, but the difference is below 0.01 m and are result of the inviscid assumption as will be demonstrated in the next section.

The droplet size is overpredicted by all computations compared to the measurements. The Y88 based results are about 10 nm outside of the measured uncertainty range, while the SBTL based results overpredict the droplet radius by additional 5 nm compared to the Y88 results. The maximum deviations between the two-phase models are about 1.5 nm, where the SM predicts slightly larger droplets. Overall, all combinations of two-phase models and equations of state yield a comparable quality of results, where the deviations to the experimental data are caused by the inviscid assumption (see next section).

To get further insight into the differences between the methods and to judge their possible application in involved high performance computations, the computational speed is evaluated in fig. 4.3 in reference to a corresponding ideal gas (IG) computation. SBTL and Y88 are also evaluated without condensation modeling allowing a further assessment of EoS and condensation model independently. For real gas computations without condensation modeling, the SBTL results in an overhead of only 37 % compared to the IG computation, while the use of Y88, despite its relatively simple structure

compared to IAPWS-IF97, already yields an overhead of 948 % and is thus one order of magnitude slower than the efficient tabulation method. Full condensation computations based on SM are connected with overheads of 120 % when used in combination with the SBTL and 479 % together with Y88. The additional overhead of Y88 is caused by additionally needed thermodynamic evaluations in the condensation model for subcooling, nucleation rate and droplet growth revealing again the big advantage of the SBTL. For both EoS, the SM is over twice as fast as the MM and is consequence of having only passive scalars instead of an active scalar, necessitating an iteration process in the computation of the thermodynamic state from the conservative quantities.

Overall, SM and MM yield results of comparable quality, while the SM is not only more easily implemented containing only passive scalars (see section 2.3) but also more than twice as fast. SBTL and Y88 based results are similar, with noticeable differences in the metastable region only, manifested in different droplet sizes. However, their quality cannot finally be assessed based on the presented q3D inviscid computations that do not account for boundary layer effects. The quality of the SBTL in the metastable region should be superior (see section 2.3), while providing an order of magnitude higher computational speeds compared to the comparably simple Y88 formulation. Therefore, all further considerations are based on SM and SBTL, apart from analogous comparisons in two other nozzles in the following sections, which further prove these conclusions. The influence of the boundary layers on the results is analyzed next. Then, improved accuracy and computational speed of SM and SBTL based solver in the final in-house implementation are demonstrated.

4.2.1.2 Boundary layer influence

The influence of boundary layer effects is analyzed by means of the results shown in fig. 4.4. For the chosen approach based on SM and SBTL q3D Euler, laminar and turbulent SA results are compared. Figure 4.4 shows also 3D laminar results, where the pressure is not evaluated on the center line but on the plane side walls as in the experiment.

The upstream pressure distribution is matched by all calculations. Deviations appear as soon as the first pressure fluctuation due to the discontinuous nozzle shape is encountered at about 0.03 m downstream of the throat. The damping effect of the curved walls, as difference between the q3D inviscid and viscid computations, lead to a reduction of about 300 Pa in magnitude of the pressure fluctuation. The additional damping effect of the boundary layer on the plane side wall in the 3D computation gives a further reduction

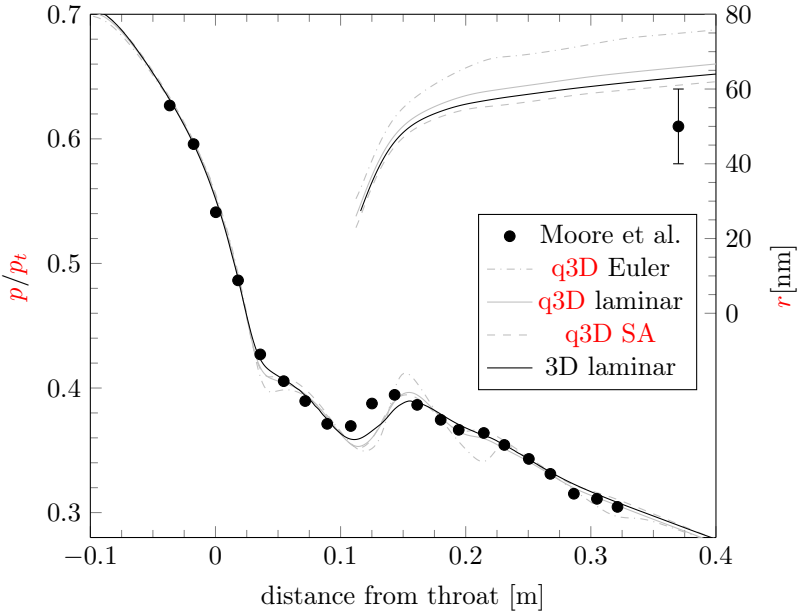

Figure 4.4: SM and SBTL based results of pressure and droplet radius on the center line for the Moore et al. nozzle B in comparison to measurement data; the pressure for the 3D case is evaluated at the plane side walls (see also [135])

by another 150 Pa compared to the q3D viscid computations. This already reveals that due to the pressure measurements on the side walls, full 3D viscid computations are needed to accurately reproduce the experimental data, as the q3D computations cannot account for the presence of the side walls.

During this pressure fluctuation, differences between laminar and turbulent computations are also visible, where the turbulent computation shows a 150 Pa higher pressure rise. This effect can also be seen further downstream and the turbulent computations therefore seems more "sensitive" regarding the influence of the evolving wave pattern. Interestingly, upstream of the condensation zone, the laminar results seem to reproduce the measurement better, while downstream of this zone the turbulent results might be superior. This suggests, that laminar turbulent transition occurs inside or close to the condensation zone, as also supported by the findings in [170]. As mentioned at the beginning of the section, the exact boundary layer states inside

the nozzle are unknown and LES computations would be very interesting to investigate this in the future.

All computations predict the pressure rise due to condensation too far downstream compared to the measurement; however, moving from inviscid to viscid to the 3D computation, the pressure rise moves upstream. At the same time, the gradient of the pressure rise decreases and shows the best agreement with the experiment for the 3D laminar computation. Downstream of the pressure rise, the pressure distribution is matched much better by all viscid computations compared to the inviscid computation, which shows deviations nearly as large as $500\,\mathrm{Pa}$. Here, the agreement of the laminar computation might be best in terms of matching the pressure fluctuations, suggesting transition as discussed before.

Compared to the inviscid computation, the droplet size shows a reduction of $20\,\mathrm{nm}$ predicted by the q3D laminar computation and a further reduction of about $5\,\mathrm{nm}$ by the turbulent computation at the measurement location, where the letter is just outside the measurement uncertainty interval. The 3D laminar computation shows a reduction of about $2.5\,\mathrm{nm}$ compared to the q3D laminar computation; however, the droplet size is about the same amount larger compared to the q3D turbulent computation and outside the measurement uncertainty interval.

Based on these findings, accuracy and computational speed of SM and SBTL in the final implementation in the in-house code is further enhanced and calibrated based on 3D laminar computations. This is also suggested in [171] and allows a direct comparison to various results reported there. The final validation is presented next.

4.2.1.3 Final validation

To validate the final SM and SBTL solver implementation in the presented newly developed solver, fig. 4.5 shows the predicted 3D laminar results compared to the measurement data. These results are also presented in [136]. As the Kelvin-Helmholtz radius of newly nucleated droplets is computed without simplification based on the Clausius-Clapeyron relation, the surface tension is used without corrections here, i.e., $q_\sigma := 1$. For the droplet growth model, $\alpha := 8$ and $\beta := 0$ are prescribed. The setups used in this work are described in more detail in section 2.3.

On this basis, the upstream pressure distribution is matched. As already seen in previously presented results, the onset of nucleation is predicted slightly too far downstream, the gradient of the pressure rise due to the condensation is in reasonable agreement with the experiment. In difference to the previously presented results, the computed droplet radius lies inside

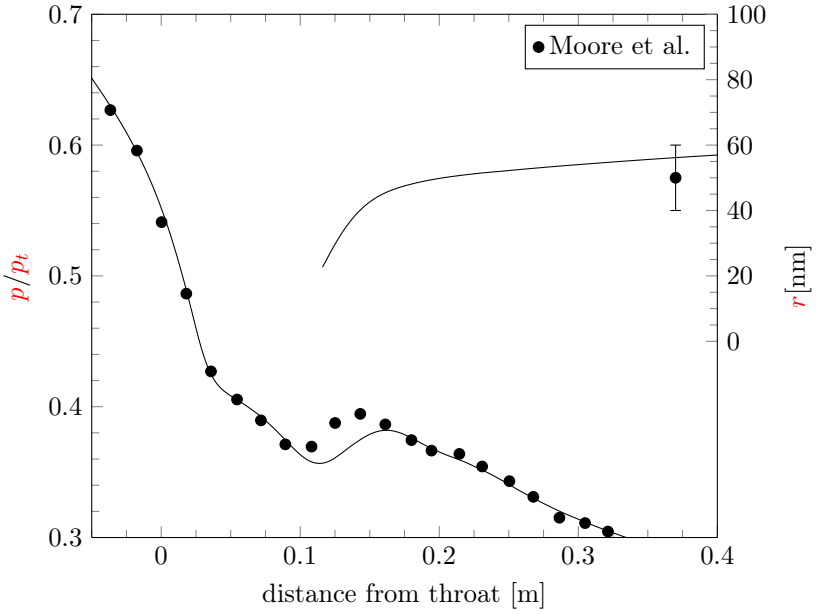

Figure 4.5: Plane side wall pressure along and droplet radius on the center line predicted by the final SM and SBTL solver implementation in a 3D laminar computation of the Moore et al. nozzle B in comparison to measurement data (see also [136])

the measurement uncertainty range. Upstream of the condensation zone, the pressure is matched (better agreement might be gained with turbulent boundary layers here, as discussed in the last section). Overall, the accuracy of the implementation is enhanced compared to the results reported in fig. 4.4. Finally, the computational speed of this optimized implementation is evaluated for this test case in fig. 4.6, referenced to a corresponding IG computation, analogously to the previous results shown in fig. 4.3. The application of the SBTL without condensation modeling is enhanced from an overhead of 37 % to only an overhead of 2 %. This is achieved by an optimized solver structure and the reduction of thermodynamic evaluations compared to a prior test OpenFOAM implementation presented in [135]. Full condensation computations result now in an overhead of only 26 % compared to the previous 153 %. These results show the great potential of the presented implementation for elaborate scale resolving computations. However, as it is not sufficient to validate the wet steam solver implementation for only one

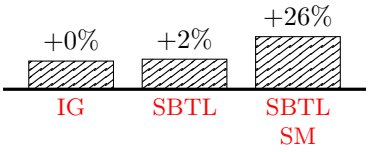

Figure 4.6: Evaluation of the computational speed of the final optimized implementation for the 3D laminar computation of the Moore et al. nozzle B, referenced to a corresponding ideal gas (IG) computation (see also [136])

operating point and expansion rate, further nozzle configurations are considered in the following, before presenting LES results of the properly validated method.

4.2.2 Moses and Stein nozzle

The only other tests with low Wilson point pressures of about $0.1\,\mathrm{bar}$ are reported by Moses and Stein [117]. Both, pressure and mean droplet size data are available along the center line, the letter measured by light scattering. Different operating conditions are investigated in one nozzle geometry, which is also shown in detail in [170]. As it consists of two arcs with different radii, the smoother wall profile does not generate expansion waves as in the case of the Moore et al. nozzle examined in the last section. However, due to the small throat dimensions of $(10 \times 10)\,\mathrm{mm}^2$, boundary layer blockage becomes significant [170, 171]. Here considered are test cases 252, with inlet condition $p_t = 40.05\,\mathrm{kPa}$ and $T_t = 374.3\,\mathrm{K}$ resulting in a Wilson point pressure of about $0.12\,\mathrm{bar}$, and 257, with $p_t = 67.66\,\mathrm{kPa}$ and $p_t = 376.7\,\mathrm{K}$ characterized by a higher Wilson point pressure of about $0.25\,\mathrm{bar}$. For case 252, an error bar for the droplet radius measurements is given in [208] for the last measured point in axial direction and used here. In absence of information about the droplet size measurement error of the 257 case, an error of $20\,\%$ as for the Moore et al. nozzle B is assumed, see [171]. First, q3D inviscid results are presented, followed by the final validation based on 3D laminar computations.

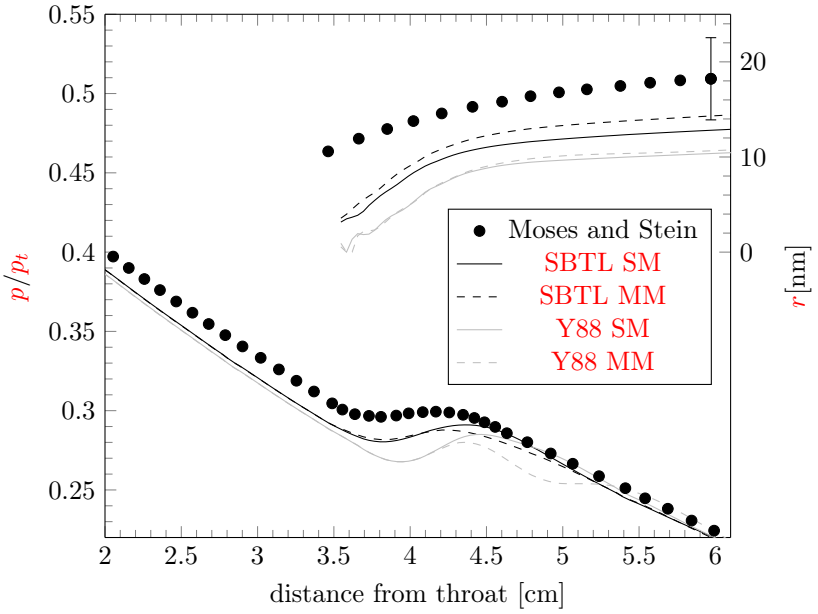

Figure 4.7: q3D Euler results of pressure and droplet radius on the center line for the Moses and Stein 252 test case in comparison to measurement data (see also [135])

4.2.2.1 q3D Euler results

As in section 4.2.1.1, q3D Euler results produced by the OpenFOAM implementations of SM and MM combined with SBTL and Y88 EoS are presented first for both operating conditions. Again, the coarse mesh of [171] containing $250 \times 2 \times 61$ points is used.

The results for case 252 are shown in fig. 4.7 in comparison to the measurement data. Upstream of the condensation zone, all calculations underpredict the pressure; the SBTL computation deviates by about 400 Pa, the Y88 computation by 600 Pa. This can be explained by the absence of the boundary layer in the inviscid computations, where the boundary layer reduces the effective throat area and thus the mass flow through the choked nozzle throat (compare with the full 3D viscid results in the following section 4.2.2.2). The typical pressure rise due to condensation is predicted at lower pressures compared to the measurement (predicted difference based on SBTL is about 500 Pa, based on Y88 1100 Pa) and also delayed by about

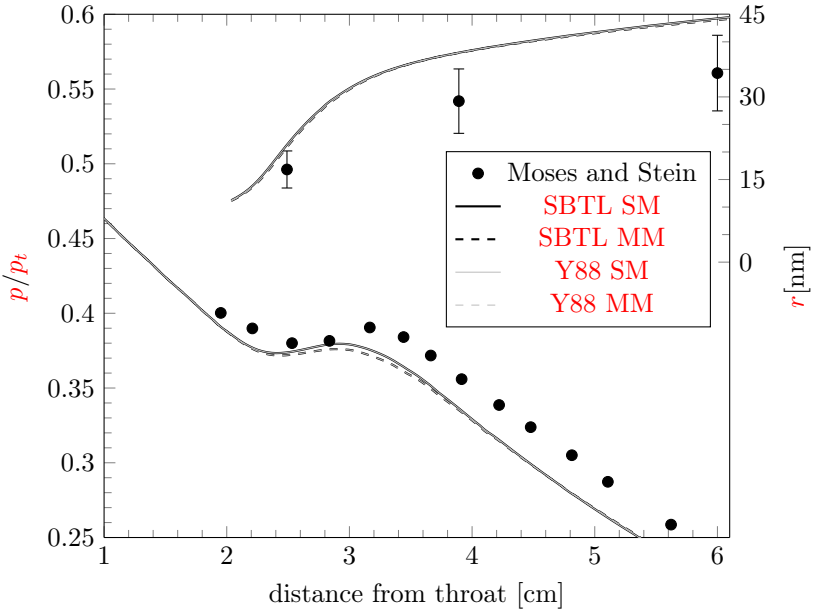

Figure 4.8: q3D Euler results of pressure and droplet radius on the center line for the Moses and Stein 257 test case in comparison to measurement data (see also [135])

1 mm for SBTL and 2.5 mm for Y88.

At about 4.1 cm downstream of the throat, SM and MM start to deviate noticeably for both EoS. While SM based results converge directly towards the measured downstream pressure, the MM based computations predict an oscillation in pressure, which is much more pronounced for the Y88 EoS with a maximum deviation of close to 800 Pa to the experiment. Downstream, all computations show about the same pressure level in accordance with the measurement. The first measured droplet sizes at about 3.5 cm throat distance are underpredicted by all computations. Downstream, the SBTL MM computation is within the measurement uncertainty interval, the SBTL SM just outside with a deviation of about 1.7 nm. The predicted radii by SM and MM based on the Y88 EoS are almost identical, with a deviation of about 3.8 nm at a throat distance of 6 cm, where the error range is known.

For the 257 case, all computations produce almost identical results, evaluated in fig. 4.8. The only noticeable difference are about 250 Pa lower pressures predicted by MM compared to SM for both EoS. The downstream pres-

sure distribution is underpredicted by about 1200 Pa by all computations. The quality of the upstream pressure distribution cannot be judged based on the given measurement data, the typical pressure rise seems to be matched by all computations. However, the gradient of the pressure rise seems to be underpredicted leading to the underestimation downstream. The droplet size is overestimated by all computations. At the last measurement point, 6 cm downstream of the throat, the 20 % measurement error region is missed by about 3 nm. This reproduces the overall quality of results reported in [171].

Overall, the SBTL based results show a better agreement to the Moses and Stein measurements compared to the Y88 EoS. The MM reproduces the droplet radii better shows, however, considerable deviations in the downstream pressure distribution. Thus, findings of section 4.2.1.1 with the choice of the SM formulation in combination with the SBTL EoS are confirmed. Again, due to the boundary blockage effects in the Moses and Stein nozzle, final validation of the solver is done based on full 3D laminar results, described in the next section.

4.2.2.2 Final validation

As in section 4.2.1.3, the final SM and SBTL solver implementation is validated showing results of 3D laminar computations of the Moses and Stein nozzle test cases. These results are presented in [136] and the condensation modeling parameters are also given in the referenced section 4.2.1.3. The medium grid of [171] is used, containing $350 \times 91 \times 91$ grid points. Computed pressure and droplet radius distributions along the center line in comparison to measurement data are shown in fig. 4.9 for both test cases.

For case 252, fig. 4.9a, the upstream pressure distribution is now matched accurately. The influence of the resolved boundary layer can be seen when comparing to the q3D Euler results presented in the previous section 4.2.2.1. The condensation process is reproduced reasonably within the known limitations, where the pressure is underestimated by a maximum of about 500 Pa and the pressure rise is delayed by about 3 mm compared to the measurements. Furthermore, the pressure rise gradient is predicted more pronounced; however, the downstream pressure after about 4.4 cm downstream of the throat is accurately matched. The droplet radius distribution shows similar results compared to the corresponding q3D computation. The droplet radii are underpredicted, with a deviation of about 1.1 nm from the measurement error interval.

The results of case 257 are shown in fig. 4.9b. The upstream pressure is matched better compared to the q3D Euler results. Also the pressure rise due to the heat release is not accurately predicted. However, the downstream

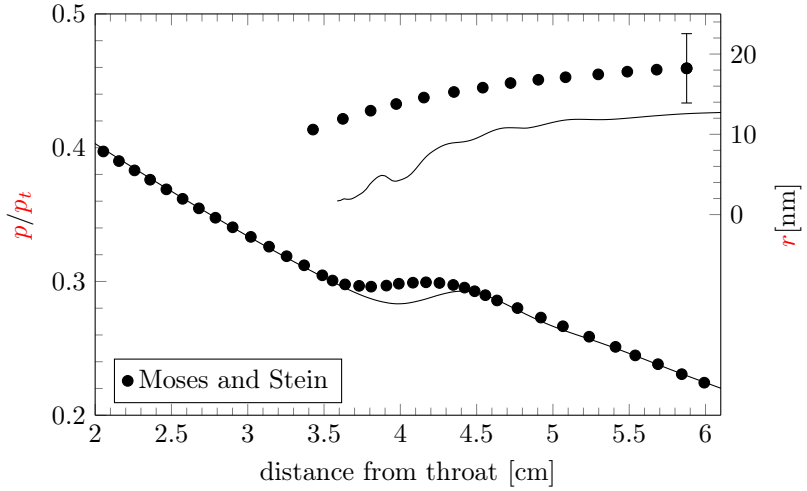

(a) case 252

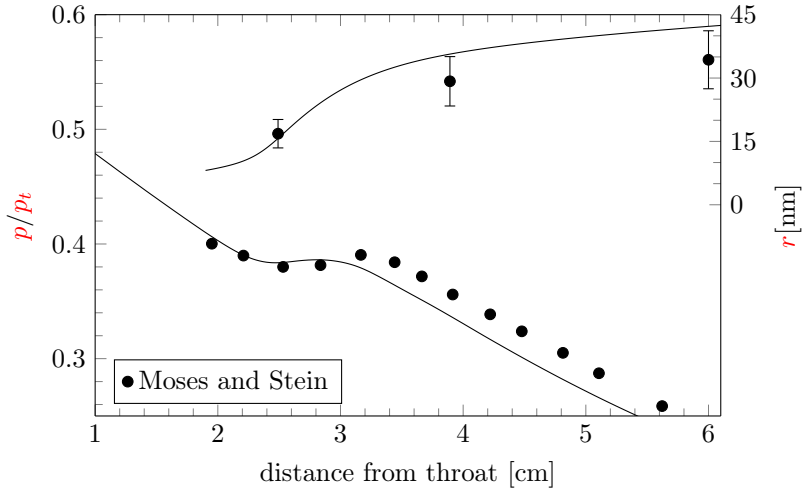

(b) case 257

Figure 4.9: Pressure and droplet radius along center line predicted by the final solver implementation in a 3D laminar computation for the Moses and Stein nozzle test cases in comparison to measurement data (see also [136])

pressure is again underpredicted, here by about 1500 Pa. This is in line with the quality of results reported in [171]. The droplet size is matched better compared to the q3D Euler results, where the deviation from the measurement error range is less than 1 nm at the last measurement position at about 6 cm throat distance. As for the Moore et al. nozzle B, the boundary layer state is unknown and the effective boundary layer blockage can only be determined based on wall resolving LES computations.

Overall, the quality of the presented results in the three nozzle geometries reflects the current state-of-the-art in modeling and prediction of wet steam flows, especially at these low Wilson point pressures. With this calibration, the solution method is in the following employed to the prediction of condensing wet steam flows in a steam turbine cascade.

4.3 White et al. Cascade

After its calibration and validation in classical nozzle geometries, the wet steam solution method is employed to compute a turbomachinery configuration, the well-known cascade test case of White et al. [197]. This is in fact the only freely accessible wet steam turbine configuration; however, many published studies do not use the exact geometry but simplified versions thereof. In this work, only the original blade profile, including a blunt trailing edge, is used. The geometry was provided by the authors and the given profile coordinates were interpolated to gain a higher resolution. The blade surface is modeled as an adiabatic, viscous wall. In pitchwise and spanwise directions periodic boundary conditions are imposed.

White et al. [197] provide detailed experimental results for a wide range of inlet steam conditions and exit Mach numbers. Properties of the considered operating points are listed in table 4.1, containing the total inlet quantities $p_{t,\mathrm{in}}$ and $T_{t,\mathrm{in}}$, the superheat of this inlet state $T_{t,\mathrm{in}} - T_s\,(p_{t,\mathrm{in}})$, imposed outlet pressure p_{out} and the resulting isentropic Mach number $M_{s,\mathrm{out}}$ at the exit.

Table 4.1: Considered operating points for the turbine configuration of White et al. [197]

OP	$p_{t,\mathrm{in}}$ [Pa]	$T_{t,\mathrm{in}}$ [K]	$T_{t,\mathrm{in}} - T_s\,(p_{t,\mathrm{in}})$ [K]	p_{out} [Pa]	$M_{s,\mathrm{out}}$
L1	40 300	354.0	4.5	16 300	1.24
L2	40 900	354.0	4.0	19 400	1.11
L3	41 700	357.5	7.5	20 600	1.08

For almost all experiments, the exit flow was constrained by two tailboards to adjust and provide steady operating conditions. Strong unsteadiness were observed for measurements with unconstrained flow. Therefore, in all OPs considered here, an porous upper tailboard was used and color Schlieren photographs of the shock wave structure, blade surface static pressure and the droplet radius at one point of a downstream pitchwise traverse are provided.

In the following, RANS results for all OPs listed in table 4.1 are shown first. On this basis, high quality LES results for the L1 OP are presented.

4.3.1 RANS results

In this section, RANS results for all OPs in table 4.1 are reported, as also presented in [136]. The RANS equations are solved implicitly employing a LUSGS scheme with a CFL number number of 100, ramped at startup. The flow field of all computations is initialized with constant pressure $40\,000\,\mathrm{Pa}$, temperature $550\,\mathrm{K}$ and velocity magnitude $5\,\mathrm{m/s}$, with adjusted flow angles along the blade from 0° at the inlet to 88° at the exit. In absence of any information from measurement data, the standard $\tilde{\mu}/\mu := 3$ is specified at the inlet for the employed SA turbulence model.

The mesh independence study is conducted for the L1 OP, for which highest velocities are expected. Mesh configurations with internal cell numbers ranging from 15 000 to 66 000 were evaluated regarding the computed mass flow, see fig. 4.10. A mesh independent configuration is reached with the mesh containing a total of 56 000 internal cells. All following computations are conducted on this mesh, shown in fig. 4.11. To allow the turbulence model to converge properly, 60 000 iterations are carried out for every calculation.

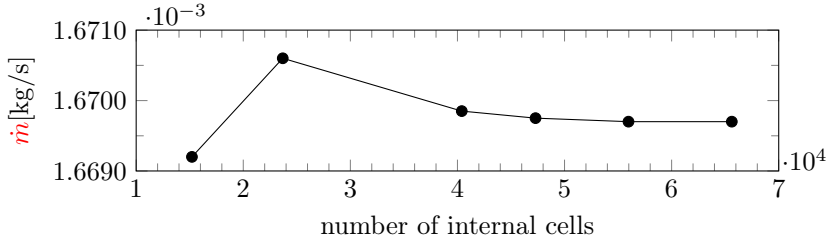

Figure 4.10: Mesh independence study considering the L1 operating point for RANS computations of the White et al. cascade (see also [136])

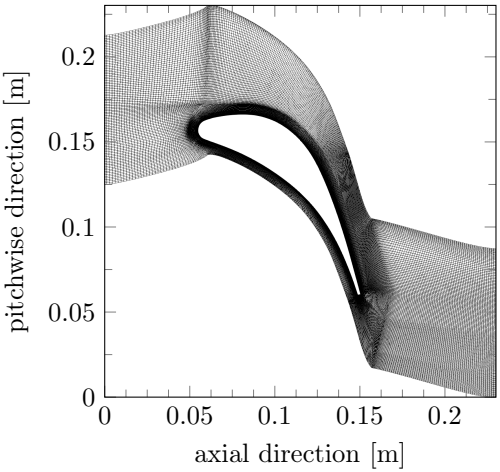

Figure 4.11: Final RANS mesh used for computations of the White et al. cascade (see also [136])

Inspection of the wall resolution reveals that the average y^+ values for all calculations are about 0.1 with a maximum below 0.2.

Figure 4.12 shows the evaluation of the surface pressure distributions on the blade for all considered OPs (the blunt trailing edge is not included in the calculation of the normalized arc length). All OPs show a reasonable agreement with the experimental data on the pressure side along the whole arc length. Due to higher pressure levels combined with low velocities, condensation rarely occurs on the pressure side. In contrast, the suction side pressure distribution shows the typical pressure rise due to the heat release in course of the condensation process, most prominent in the L1 case.

The suction side surface pressure distribution is matched remarkably well for the L3 case, where only a slight offset to the measurement can be observed close to the trailing edge. Also for the L2 OP, the results are in good agreement with the experiment along the suction side. The pressure rise and thus the onset of condensation is matched, its gradient is slightly underpredicted as is also the downstream pressure with a maximum difference of about 2000 Pa at 0.8 arc length. Here, a second small pressure rise is seen in the experimental data, which is not captured by the computation. However, the downstream pressure level is matched. The last measurement point adjacent to the blunt trailing edge shows again a deviation of about 2000 Pa from the measurement. Finally, the L1 OP shows the worst agreement to the mea-

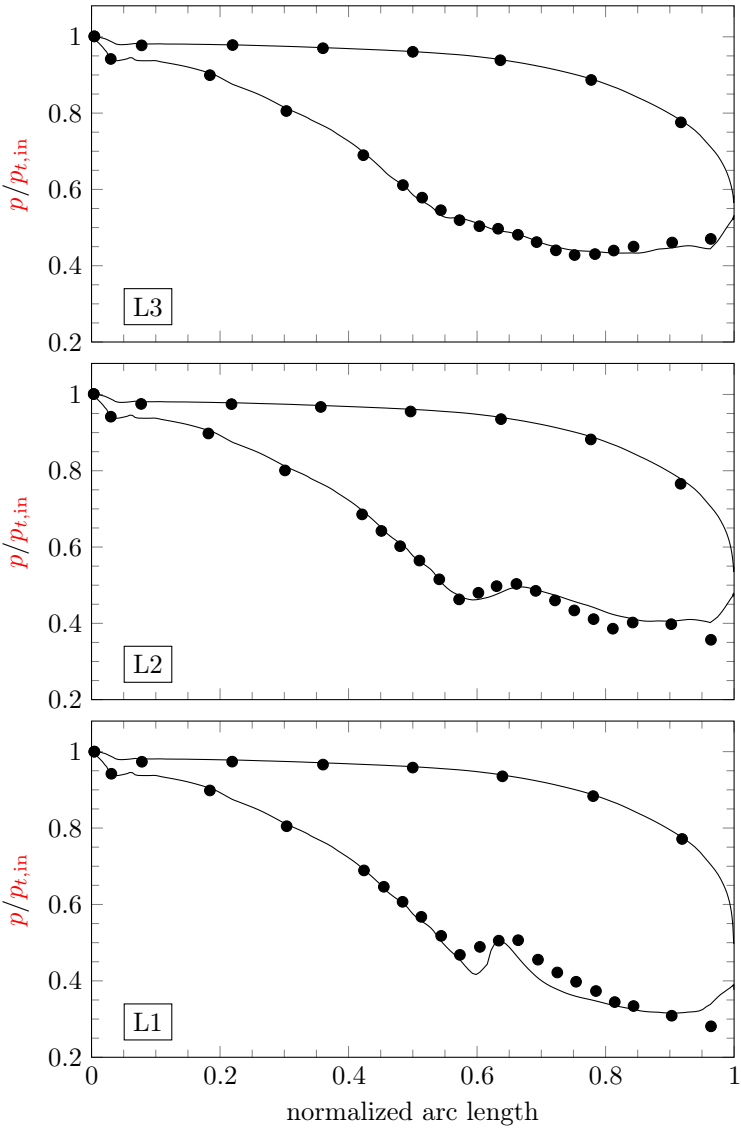

Figure 4.12: Evaluation of the blade pressure distributions for White et al. Cascade test cases (see also [136])

surement data. Upstream of the pressure rise, the pressure is matched accurately; however, the onset of condensation is predicted too far downstream by about 0.024 normalized arc length. This results in an underestimation of the pressure of about $2000\,\mathrm{Pa}$ at 0.6 arc length. At the same time, the gradient of the pressure rise is overpredicted; nevertheless the pressure level downstream of the condensation zone is not matched and underestimated until about 0.8 arc length. The last measurement point adjacent to the blunt trailing edge shows again a deviation of about $2000\,\mathrm{Pa}$ from the measurement, as also seen in the L2 OP.

Overall, the results are in reasonable agreement with the measurements, reflecting the current state-of-the-art in modeling and prediction of wet steam flows under low Wilson point pressures. With the validation in classical Laval nozzles (section 4.2) and the White at al. cascade based on RANS, the influence of the turbulence modeling approach on the prediction of wet steam turbine flows will be investigated by means of LES of the L1 OP in the next section. This will also include a more detailed analysis of the presented RANS results in comparison to URANS and LES.

4.3.2 LES of the L1 operating point

In this section, the developed FVM solution scheme is employed for a LES of the L1 OP of the White et al. cascade, as presented in [137]. This OP is chosen, as it is characterized by the strongest influence of condensation among the experiments, see section 4.3.1. The basis for this are the validation of the numerical method for LES application based on hybrid flux treatment and high order time integration presented in [137], the state-of-the-art wet steam capabilities demonstrated in this chapter and the achieved high computational speed, reported in section 4.2.1.3. To assess the influence of the turbulence modeling approach on the prediction of the wet steam turbine flow, the LES results are compared to those of RANS and URANS computations. To enhance robustness and computational speed, the Clausius-Clapeyron relation is used in the critical droplet radius calculation of all computations. This approximation strongly influences the results and necessitates the reduction of the flat film surface tension by a constant factor of $q_\sigma := 0.95$ to obtain a comparable quality of RANS results.

In the following, mesh and computational details are described first. Shock sensor and LES mesh quality are assessed next. Blade pressure distribution, Schlieren results and the droplet radius in a downstream pitchwise traverse of all computations are compared, also to the experimental data. Finally, the unsteadiness of pressure and wetness fields are evaluated.

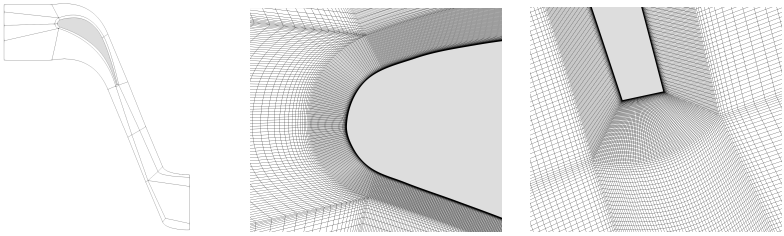

(a) Computational domain and blocking (b) Leading edge region (c) Trailing edge region

Figure 4.13: Details of the LES mesh for the White et al. cascade (see also [137])

4.3.2.1 Mesh and Computation

In difference to a standard RANS domain, as used in section 4.3.1, fig. 4.11, the computational domain of the LES mesh is designed to resolve wake, trailing edge shock wave system and condensation zone without the immediate influence of the outlet boundary condition. Therefore, the computational domain is extended with a high resolution of the wake region over at least one chord length. To ensure direct comparability, the same computational domain, shown in fig. 4.13a with the underlying block structure, is used for all computations. RANS and URANS meshes contain one cell layer in spanwise direction with about 100 000 cells, while the LES mesh contains 100 cell layers in spanwise direction with 48×10^6 cells.

To ensure appropriate near wall resolution for the wall resolved LES, the cell sizes at the blade wall are estimated based on RANS results to yield $y^+ < 1$ in normal and $x^+ \approx z^+ \lesssim 50$ in tangential and bi-tangential directions, respectively. The resulting mesh resolutions close to leading and trailing edges of the LES mesh are shown in figs. 4.13b and 4.13c. Furthermore, the actually achieved time averaged values of y^+, x^+ and z^+ are evaluated in fig. 4.14 (negative values of the arc length indicate the pressure side of the blade). The desired wall resolution is achieved with time averaged y^+ values below a maximum of 0.6, z^+ below 50 and x^+ below 30. At the same time, the expansion ratio of the cell layers away from the wall is chosen to be below 1.1.

The flow through time is estimated to be 2.3 ms based on free-stream velocity in the passage and approximated stream filament length through the computational domain. After initialization from a RANS result, two flow through times are computed before averaging in time is started for another 1.5 flow

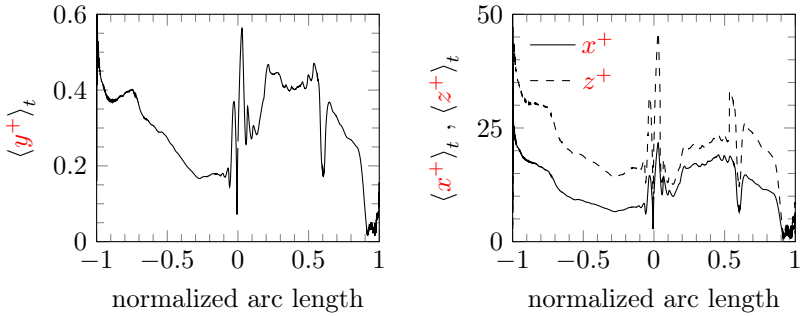

Figure 4.14: Time averaged near wall resolution of the LES mesh for the White et al. cascade (see also [137])

through times. On an in-house high-performance cluster equipped with Intel Xeon Gold 6132 CPUs, one flow through time takes about 1000 weeks total CPU time. In case of the LES computation, time is integrated employing the classical 4^{th} order Runge-Kutta scheme with a global time stepping and a CFL number number of 0.8 (resulting in time steps below 3.5 ns). The RANS computation relies on the 2^{nd} order low storage Runge-Kutta scheme with local time stepping and a CFL number number of 0.8. For URANS, a dual time stepping is employed with a constant physical time step of 1 µs and inner loops as in the RANS case. This computation is initialized from the RANS result and after a steady oscillating state is reached, time averaging is done for about one flow through time.

4.3.2.2 Shock sensor and LES quality assessment

As the Ducros-type shock sensor definition (see section 3.1.3.3) is employed here for the first time in the context of a condensing wet steam flow, with additional discontinuities due to the spontaneous condensation process, the time averaged shock sensor field on mid span is evaluated in fig. 4.15 for its assessment. The upwind flux is only used in detected shock regions with $\chi > 0.65$, indicated in red in fig. 4.15. This is the case for the trailing edge shock wave structures at pressure and suction side, which are sharply detected over the span of only a few cells. However, one region seems unnecessarily marked as shocked by the employed shock sensor definition, restricted to a small region close to the trailing edge on the suction side of the blade. Here, neither shock waves nor sharp discontinuities due to the condensation process are present and it thus seems to be a general deficit of the formu-

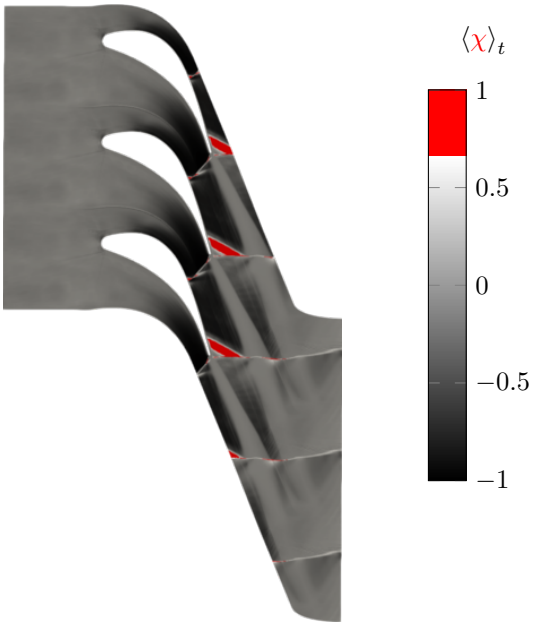

Figure 4.15: Time averaged shock sensor field on mid span of the White et al. cascade LES; in red are regions with $\chi > 0.65$ (see also [137])

lation. Therefore, the shock sensor appears suitable for application in LES of condensing wet steam flows, reducing the numerical diffusion to a minimum and providing the necessary robustness and low dissipation properties.

In addition to the shock sensor, the quality of the LES mesh is also assessed applying the single grid estimator of Celik et al. [18]. For this LES quality criterion, values above 0.8 indicate high quality LES and above 0.95 near DNS resolutions. Evaluation for the present LES computation reveals values in the range between 0.87 and 0.98, suggesting high quality results with values well above the 0.8 threshold. The lowest values of the quality criterion are encountered around the trailing edge shock waves, while the wake is resolved with values between 0.9 and 0.94. In major parts of the passage, a near DNS resolution is achieved.

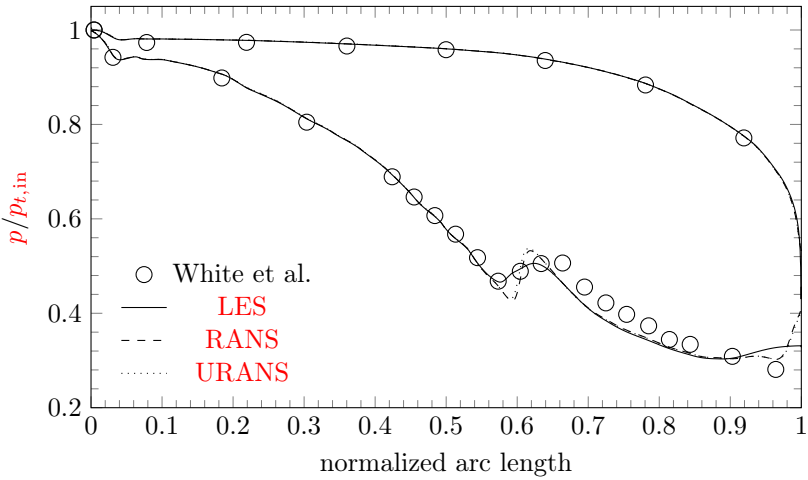

Figure 4.16: (Time averaged) blade pressure distributions of all computations for the L1 OP of the White et al. cascade (see also [137])

4.3.2.3 Blade pressure distribution

The (time average) blade pressure distribution predicted by all computations is presented in fig. 4.16 in comparison to the experimental data. On the pressure side, the measurement is matched by all computations over the whole arc length. The same holds for the suction side upstream of the condensation zone. Downstream, in the condensation zone and close to the trailing edge, differences between the computations are noticeable. Here, RANS and URANS yield almost identical results, where only a marginal difference can be located within the condensation zone. However, compared to the measurement, both computations predict the typical pressure rise too far downstream and subsequently overestimate its pressure gradient. Downstream of the pressure rise, the pressure distribution is underpredicted, while its trend is matched. As intended, these results reflect the same quality as the results reported in section 4.3.1, fig. 4.12.

Despite identical condensation modeling, the LES computation matches the condensation pressure rise perfectly in terms of onset and gradient in agreement with the experiment data. As the droplet growth model is calibrated based on RANS computations, the LES shows a similar behavior as RANS and URANS further downstream. This in consequence suggests

that the flow downstream of the core condensation zone is not governed by unsteadiness, as will be further analyzed in section 4.3.2.6. These findings reveal that condensation is underpredicted by the employed condensation model with the prescribed constants. In principle, the agreement with the downstream pressure distribution can be enhanced by recalibration based on these LES results. This in consequence will probably also enhance the agreement with the measurement close to the trailing edge. Overall, the condensation process is much better captured by the LES compared to standard RANS and URANS. This finding clearly indicates that the capabilities of the simulation method to accurately account for unsteady processes like turbulence, shock waves, spontaneous condensation and their interaction is of paramount importance for a predictive nature of wet steam computations.

4.3.2.4 Schlieren results

To analyze the mechanisms by which the LES computation is able to accurately reproduce the measurement in the condensation zone in contrast to RANS and URANS, the contours of the (time averaged) density gradient magnitude are shown in fig. 4.17 for comparison to the Schlieren photograph results (figure 10) of White et al. [197]. This allows to visualize and compare the shock structures and the heat release of condensation, here referred to as the "condensation shock" to follow the wording used in [197]. The authors mark pressure and suction side shock waves, which are also present in a single-phase flow, as S_p and S_s, respectively. The additional feature due to condensation, the "condensation shock", is referred to by S_c. The position of the latter is dependent upon the inlet superheat, while the trailing edge wave structure is influenced by the exit Mach number.

The considered OP is characterized by a curved main feature of the shock wave pattern propagating across the central blade passage without a reflection from the opposite suction side surface [197]. On closer analysis, two shock waves can be distinguished, the usual pressure side shock wave S_p and the feature S_c associated with condensation, where S_p extends only partway across the passage before merging with S_c [197].

All computations show these three main features S_p, S_s and S_c and overall a reasonable agreement with the measurement. On further inspection, RANS and URANS yield similar results with a rather weak pressure side shock wave, which seems to be branched into two distinct features. The LES resolves the pressure side shock wave sharply and predicts an interaction with the "condensation shock", which results in the curvature also present in the Schlieren measurement.

This interaction of S_p and S_c predicted by the LES in contrast to RANS and

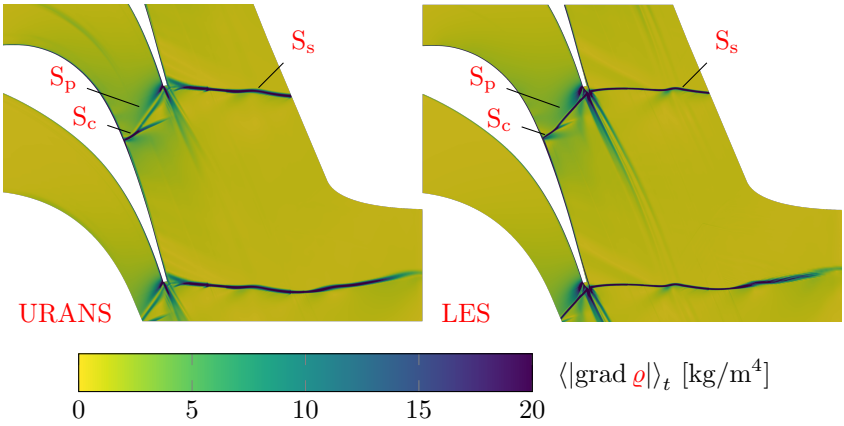

Figure 4.17: Contours of time averaged density gradient magnitude of URANS and LES results for comparison with the Schlieren measurement results of the White et al. for OP L1 (figure 10 in [197]) (see also [137])

URANS, seems to lead to a weakening of the "condensation shock" strength in comparison to the other computations. In the RANS and URANS results, the "condensation shock" seems to be a rather distinct feature reaching deeper into the domain without the damping influence of the pressure side shock wave compared to LES and measurement. In addition, the position of S_p seems to be predicted slightly more upstream by RANS and URANS, influencing the interaction with the condensation. These findings are in accordance with the evaluation of the blade pressure distribution discussed in the last subsection, where the pressure rise is predicted too far downstream with an increased intensity by RANS and URANS, while LES is able to match the measurement.

4.3.2.5 Droplet Radius

The (time averaged) droplet radius distribution evaluated on a downstream pitchwise traverse is shown in fig. 4.18 in comparison to the Sauter mean droplet radius at one position, as the only available measurement point from [197]. The large pitchwise variations of the mean droplet sizes predicted by the computations are due to large variations in nucleated droplet numbers and formation of wetness caused by local differences in expansion rate and the influence of the trailing edge wave system on the nucleation zone [197].

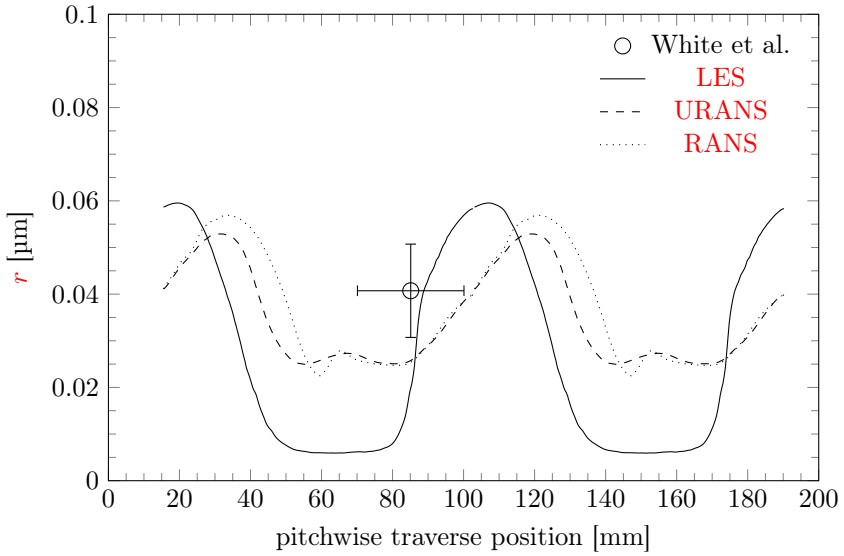

Figure 4.18: Downstream droplet radius distribution for the L1 OP of the White et al. cascade (see also [137])

While nucleation takes place in a region of rapid expansion close to the suction side surface leading to a large number of small droplets, the onset of condensation is delayed close to the pressure side surface through the temperature rise generated by the trailing edge shock [197]. This moves the nucleation locally into a region of lower expansion subsequently yielding, fewer but larger droplets [197].

The evaluation of the droplet radius distribution shows again similar results for RANS and URANS, for LES, however, noticeable differences, despite identical condensation modeling. The LES predicts smaller droplets in the wake region and larger droplet sizes within the blade passage with a steeper gradient between these regions compared to the other computations. While RANS and URANS results are just outside the measurement error interval of the single available experimental point, the LES reproduces the measured droplet size accurately within the experimental accuracy.

4.3.2.6 Pressure and wetness fields

To further analyze differences of LES and URANS based results, time averaged pressure and corresponding standard deviation fields are presented in

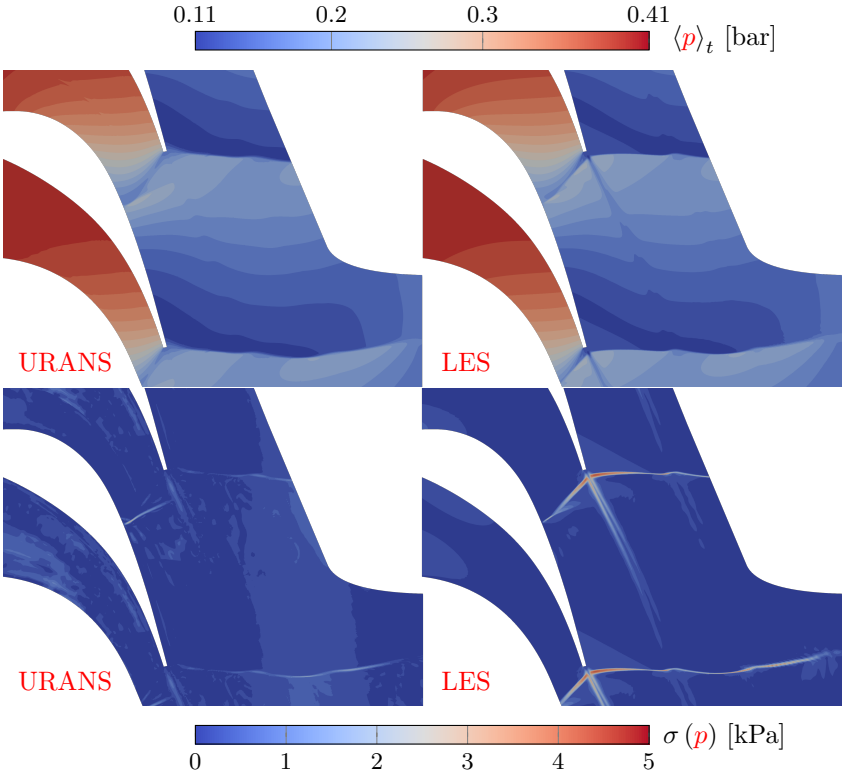

Figure 4.19: Time averaged pressure and corresponding standard deviation computed by LES and RANS for the L1 OP of the White et al. cascade (see also [137])

fig. 4.19. The time averaged pressure field of the URANS computation confirms the findings made based on the Schlieren results: compared to the LES results, "condensation shock" and pressure side shock wave are rather distinct features. In the condensation zone, the pressure rise on the suction surface is more pronounced in the URANS results, while the LES also predicts the maximum pressure slightly away from the wall. The URANS yields a rather distinguishable "condensation shock" reaching far into the blade passage. In contrast, the LES yields a sharply defined pressure side shock wave downstream of the trailing edge, which merges with the "condensation shock" within the domain. The standard deviation of the time averaged pressure clearly reveals that the LES based computation is much better able to

account for the unsteady nature of the shocks at the trailing edge and their interaction with the condensation zone. The URANS, on the other hand, shows only a small pressure variance in the condensation zone itself.

A clear difference in the blade's wake predicted by LES and URANS is found in the evaluation of the time averaged wetness fraction field, shown in fig. 4.20. While the URANS predicts a rather dry streak, the wake of the LES contains a noticeable amount of wetness, because condensation occurs in case of the LES also in the incipience region of the pressure side shock wave and the nucleated wetness subsequently forms part of the wake. At the same time, higher fractions of wetness are encountered close to the suction side blade wall. Also in accordance to the previously analyzed droplet radius results, the LES features a higher streak of wetness in the middle of the passage compared to URANS. Evaluation of the corresponding variances shows, that the URANS is only able to account for unsteadiness in the wake region, while the LES predicts also high level of unsteadiness throughout the whole condensation zone, including the near wall region. These results further prove that LES is much better able to account for the inherent unsteady nature of the spontaneous condensation process.

4.4 Conclusions and outlook

In this section, the work in the area of condensing wet steam flows is presented. First, q3D inviscid computations of classical nozzle test cases are used to compare mixture model and source term model implementations and different commonly used wet steam EoS. SBTL and source term model show overall the highest potential for the application in more complex flows. While the accuracy of source term model and mixture model are comparable, the source term model is twice as fast, because the pressure does not have to be iterated. At the same time, the speed potential of the SBTL method is revealed.

On this basis, the computational speed of source term model in combination with the SBTL EoS is further enhanced. The validation of this implementation is conducted showing full 3D laminar computations of nozzle flows with low Wilson point pressures. These laminar results show a good agreement with the experimental data, as boundary layer effects are accounted for in difference to inviscid computations. The overall agreement with the calibrated nucleation theory is within the known limitations of the current wet steam modeling standard as presented in [171]. At the same time, a considerable speedup is reported, where the SBTL method shows only an overhead of 2 % compared to a baseline IG computation, while a full condensation

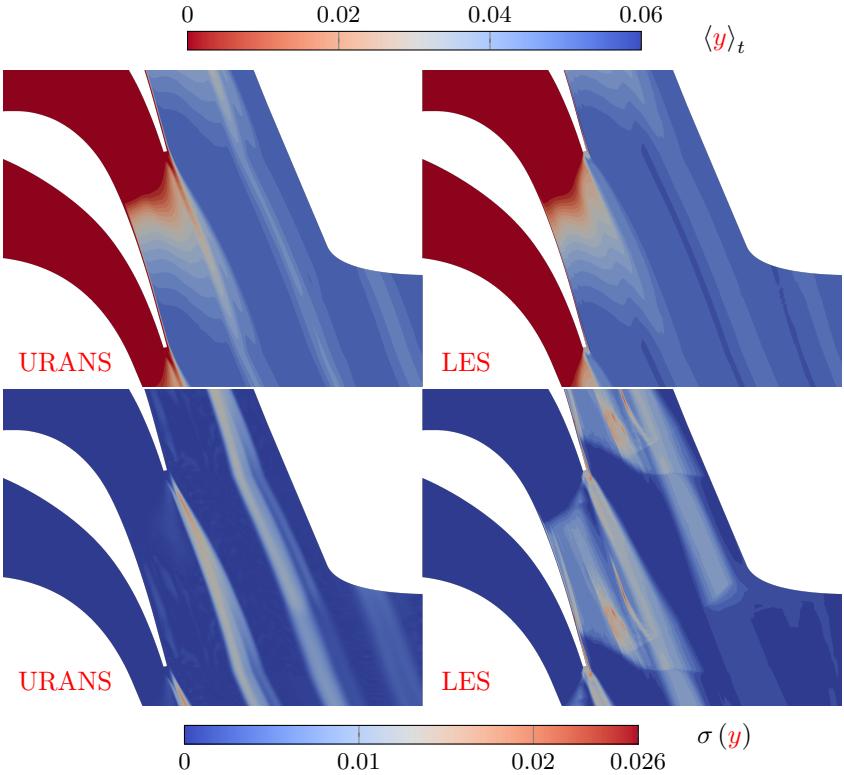

Figure 4.20: Time averaged wetness fraction and corresponding standard deviation computed by LES and RANS for the L1 OP of the White et al. cascade (see also [137])

computations is only connected to an overhead of 26 %.

Having achieved validation and speedup, the solver is applied to a turbomachinery configuration. For the White et al. [197] cascade test case, a reasonable agreement is reached. First extensions of the solution method to incompressible LES based on a central scheme in energy consistent form are reported in [136], showing also results for the real gas implementation. The first scale resolving LES computation in the field of wet steam flows is presented in this work and in [137]. The results within the condensing wet steam cascade are thoroughly compared to RANS and URANS computations as well as the available experimental data. As explained in section 3.1.3.3, a highly accurate numerical treatment is adapted for the LES computation to

provide an accurate treatment of turbulent scales of any size in presence of shock waves, as appearing in the cascade flow. The discontinuities of the condensation process pose an additional challenge. In this work, the hybrid flux switches between a baseline non-dissipative central flux in energy consistent split form and a shock-capturing upwind flux in shocked regions based on a shock sensor. This hybrid scheme is validated showing results of a decay of homogeneous isotropic turbulence test case containing eddy shocklets in section 3.4 (see also [137]) and then employed in condensing wet steam flows for the first time.

The shock sensor definition is proven to be appropriate for application in condensing wet steam flows and the high quality of the LES results is demonstrated based on LES quality criteria and near wall resolution analysis. Overall, the LES results are much better able to reproduce the experimental data compared to RANS and URANS computations. Despite identical condensation modeling, the onset of nucleation and the shape of the pressure rise due to the condensation are only matched by LES. The Schlieren results reveal that the LES is able to account for the interaction of "condensation shock" and pressure side shock wave, while RANS and URANS yield rather distinct features. At the same time, the LES matches accurately the only available measurement point of the downstream droplet size distribution and shows more pronounced differences between droplet sizes in wake and passage region compared to RANS and URANS computations. Further analysis of differences in URANS and LES reveals that only LES is able to account for the inherently unsteady nature of the spontaneous condensation process and the interaction with the trailing edge shock wave structure, while URANS captures only unsteadiness in the blade's wake region. These findings prove that the inherently unsteady nature of the condensation process and its interaction with other unsteady flow phenomena, which still lack understanding today, cannot be investigated properly based on simple steady state computations. However, at the relatively moderate Reynolds numbers in the low-pressure turbine and in light of the continuously increasing computational power, high-fidelity, unsteady, scale-resolving simulation techniques such as LES hold the potential to address this research need and to improve future designs.

For the detailed understanding of the interaction of turbulence and wet steam model in the description of turbulent condensing steam turbine flows, additional LES at different operating conditions will be conducted in the future. To further increase the overall quality of the modeling, a more sophisticated two-phase treatment seems promising, though computationally very challenging. Due to the small time steps in LES, a Euler-Lagrange treatment appears feasible and would provide the best description of the droplet

size spectrum, but efficient parallelization remains one of the main challenges. For this task, advantage will be taken of the hybrid CPU/GPU solver parallelization, only the porting of the SBTL tabulation remains and is in progress. For steady state computations, quadrature based moment methods like QMOM will be implemented. The SMOM method is already implemented and will be compared with the presented monodispersed method in the future.

As indicated in [171], a detailed comparison of EoS has not yet been conducted. The presented comparison of Y88 and SBTL is the first step, but a direct implementation of IAPWS-IF97 and other steam EoS will be done in the future. These state equations can also serve as benchmarks on the GPU. The largest obstacle connected with wet steam flows, however, remains the uncertainty connected to the classical nucleation theory. Research in this area will be conducted. Furthermore, an extension into the high pressure region is to be considered, as especially interesting for supercritical flows, not only for steam but also for CO_2, as presented in chapter 6.

5 ORC Application

The path towards sustainable energy sources will be long and sometimes difficult ... We cannot cede ... the technology that will power new jobs and new industries, we must claim its promise. That's how we will maintain our economic vitality and our national treasure—our forests and waterways, our crop lands and snow-capped peaks. That is how we will preserve our planet, commanded to our care by God. That's what will lend meaning to the creed our fathers once declared.

Barack Obama, 44th U.S. President, 2013

One of the greatest challenges of the 21st century is the transition towards sustainable energy generation with reliable service and at affordable prices. The net-zero CO_2 emission target in the energy and transportation sector can only be reached with innovations in the field of power generation and energy efficiency. Here, a wide range of low temperature heat sources provide a large amount of energy, though, at such low temperatures that prevent their economical exploitation by traditional power generation techniques. Most prominent examples are waste heat from industry and transportation, solar thermal and geothermal energy and biomass. One technology with the potential for large-scale commercial deployment is the Organic Rankine Cycle (ORC), which is not only applicable to low temperature heat sources but can also be employed for cogeneration or as the bottoming cycle of a higher-temperature cycle, such as diesel engines, Brayton Cycles or other Rankine Cycles.

Overall, the ORC represents an emerging technology with a worldwide installed capacity increase from about 0.7 GW to 2.7 GW between 2005 and 2016 [177]. The rather new technology has already a wide application range in waste heat recovery and renewable power generation, ranging from micro-scales with a few kW to large multi GW power plants. The ORC follows the same principles as the traditional steam Rankine cycle used in most thermal power plants to produce electricity, but uses an organic fluid instead of H_2O. Using an organic fluid with lower evaporation temperatures compared to

H_2O allows for the effective use of low temperature heat sources and the selection of the best working fluid depending on the available heat source and the plant size. Overall, this results in higher performance compared to both steam Rankine cycles and gas Brayton cycles, especially for heat sources lower than 400 °C and a power output lower than 20 MW [177].

The working fluid can be selected from a long list of candidates, including hydrocarbons, hydrofluorocarbons, siloxanes and mixtures of these components. Typically, ORC turbines are very compact with one or only a few number of stages [125]. However, the design of efficient ORC turbines is very challenging. The compact design leads to high expansion ratios with transonic or supersonic flow conditions in the turbine. To minimize shock losses in the rotor, the degree of reaction of ORC stages is generally kept as small as possible and the stator section is often designed as a convergent-divergent nozzle [122, 125]. At the same time, strong real gas behavior is encountered in the relevant pressure and temperature ranges, at which ORC turbines operate. This results in low sound speeds and high pressure ratios, where real gas effects occur under supersonic conditions considerably affecting the turbine performance [25]. This necessitates an efficient and accurate approach to real gas thermodynamics in the design stage, which is described in this work.

ORC turbines typically operate in cycles driven by volatile heat sources, like heat recovery from residual energy of industrial processes or exhaust gases or volatile renewable energy sources like solar thermal energy. Hence, power control of ORC turbines must enable an efficient and economical operation at part load conditions. One technical solution is a design, which allows for partial admission. Such a partial admission design can also be the solution to another challenge in ORC turbines, where relatively small volume flow rates lead to small blade heights. This yields comparably high values of endwall and secondary flow losses, like tip leakage losses. These losses can be reduced increasing the blade heights and only admitting a part of the annulus. However, this causes other losses, referred to as partial admission and windage losses [85] and a careful design is necessary. For such a partially admitted design, single-stage axial impulse turbine stages appear to be well suited [196]. Such a turbine design will be numerically investigated in this chapter.

Overall, ORC turbines often represent the most reliable option for unconventional heat sources to date, where conventional power cycles cannot provide convenient solutions to exploit low-grade heat sources. The low driving temperature differentials pose several technological challenges and lead to low cycle efficiencies, where cycle optimization even for marginal gains are a worthwhile undertaking. Today, there is still a severe lack of suitable working fluids, which leads often to a choice of working medium not tailored for the

specific application. Furthermore, there is a severe lack of experimental validation for ORC applications, particularly for low temperature heat sources and low power outputs. For a more detailed overview of developments in the field of ORC application, a vast number of reviews have been published, see, e.g., [71, 91, 104, 115, 141].

5.1 Partial admission ORC turbine test case

In this section, numerical results of the partially admitted ORC turbine of Seume et al. [160] are presented. These results are published in a more comprehensive form in [210], where the computations were conducted by the first author on basis of the FVM solver presented in this work. The single stage impulse turbine is designed for the heat recovery form the exhaust gas of a $12.8\,\mathrm{L}$ diesel engine with a temperature of about $615\,\mathrm{K}$. The key feature of the design is the use of partial admission for high efficiency levels over a wide range of operating conditions. In particular, the flow through a maximum of 8 stator passages with a Laval nozzle design can be used to partially admit 33 rotor blades with a 2D impulse design, where 2 ($20\,\%$ admission), 4 ($40\,\%$ admission) or the whole 8 stator ($80\,\%$ admission) passages can be admitted.

The rotor blade height is $3.43\,\mathrm{mm}$ with a tip gap height in operation of about $0.13\,\mathrm{mm}$ to the shroud at a diameter of $63.1\,\mathrm{mm}$. The nominal design point is given by a partial admission of $40\,\%$ and a rotational speed of $1 \times 10^5\,\mathrm{min}^{-1}$ with a turbine output of $8\,\mathrm{kW}$. The maximum power output of $18.3\,\mathrm{kW}$ is given at a rotational speed of $1.1 \times 10^5\,\mathrm{min}^{-1}$ and $80\,\%$ admission. The investigated inlet conditions are in a range of $20\,\mathrm{bar}$ to $40\,\mathrm{bar}$ (0.23 to 0.46 in reduced pressures) and $505\,\mathrm{K}$ to $540\,\mathrm{K}$ (0.944 to 1.01 in reduced temperatures). The selected working medium is ethanol with $5\,\%$ mass fraction water added to prevent corrosion of the titanium rotor. Experimental data is available for $20\,\%$ and $40\,\%$ admission with 3 inlet operating points (OPs) at $20\,\mathrm{bar}$, $30\,\mathrm{bar}$ and $40\,\mathrm{bar}$, respectively. In each case, the rotor speed for a maximum efficiency is prescribed, where the measured maximum isentropic total-to-static efficiency reaches about $57\,\%$. The diffuser pressure is in all cases about $0.81\,\mathrm{bar}$.

The accurate prediction of partly admitted turbines is very challenging, since it causes a highly inhomogenous flow field in circumferential direction requiring full annulus computations [72]. The only alternative, though, far from being of predictive nature, are conventional fully admitted computations, exploiting periodicity for a single passage simulation, with subsequent corrections to account for partial admission losses based on empirical mod-

els. In the following, only full annulus computations are presented and compared to the measurements. Loss model based results of the present computational method are reported in [210], where their accuracy in real gas ORC applications is investigated.

5.1.1 Numerical setup

In the following, steady state RANS results, closed by the SA turbulence model, and solved implicitly in time employing the LUSGS scheme are presented. For the best trade-off between accuracy and computational speed, the thermodynamic properties of the working medium mixture of $95\,\%$ ethanol and $5\,\%$ water (in terms of mass fractions) are computed based on Peng-Robinson EoS and van der Waals mixture model. Due to the constant composition of the mixture, the mixture properties for the one-fluid treatment can be precomputed and are listed in table 5.1. For the highest possible accuracy, these mixture quantities are computed based on REFPROP [94]. The polynomial coefficients for the ideal gas part of the caloric quantities are given in table 5.2.

Critical temperatures $T_r \approx 1$ at low pressures $p_r < 0.5$ at all investigated OPs allow the usage of the low-pressure gas mixture variants of the corresponding state method of Chung et al. [19] for the computation of viscosity and thermal conductivity coefficient, as presented in [130]. This method allows also for a one-fluid treatment in the computation of the transport properties and the values used for both fluids in their respective mixing rule are listed in table 5.3. In this work, only the OPs with $20\,\%$ admission are considered, their details are given in table 5.4. The given outlet pressure is iterated to yield the averaged static pressure at the diffuser exit of about $0.81\,\mathrm{bar}$, which was measured at a radius of $40.78\,\mathrm{mm}$, as indicated in fig. 5.1b.

The full annulus geometry with 2 stator nozzles and 33 rotor blades is shown in fig. 5.1a. To have a realistic pressure distribution at the diffuser exit without the immediate influence of the outlet boundary condition, the outlet is prolonged in radial direction, as indicated in fig. 5.1. At the domain outlet, a constant static pressure is prescribed, at the domain inlet, the total state is prescribed with a boundary normal velocity vector. All walls are treated by adiabatic, viscous wall boundary conditions; between the stator and the rotor domain, a frozen rotor interface treatment is employed.

5.1.2 Computational mesh

The domain is discretized by a block structured grid with a low Reynolds wall resolution of $y^+ \approx 1$. Only in the nozzle's throat area, slightly higher

Table 5.1: Mixture properties of the working medium used in a one-fluid treatment with the Peng-Robinson EoS for the ORC test case

T_c	535.1	K
p_c	86.536	bar
ω	0.562 892	
M	42.741	kg kmol^{-1}

Table 5.2: Polynomial coefficients for the NASA 7 [106] description of the working fluid mixture used for the ideal gas part in the computation of caloric state values for the ORC test case

a_1	6.101 551	
a_2	$1.375\,337 \times 10^{-2}$	K^{-1}
a_3	$-4.842\,14 \times 10^{-6}$	K^{-2}
a_4	$7.711\,717 \times 10^{-10}$	K^{-3}
a_5	$-4.571\,218 \times 10^{-14}$	K^{-4}

Table 5.3: Fluid properties used in the evaluation of the low-pressure gas mixture variants of the corresponding state method of Chung et al. [19] for viscosity and thermal conductivity coefficient for the ORC test case

	ethanol	water	
critical temperatures	513.92	647.14	K
critical volume	167.0	55.95	cm^3/mol
acentric factor	0.649	0.344	
molar mass	46.069	18.015	kg kmol^{-1}
dipole moment	1.7	1.8	Debye
association factor	0.175	0.076	
mole fraction	0.881 38	0.118 62	

Table 5.4: Considered OPs for the partially admitted ORC turbine test case

admission [%]	$p_{t,\text{in}}$ [bar]	$T_{t,\text{in}}$ [K]	p_{out} [bar]	rotational speed [min^{-1}]
20	20	507.77	0.923	70 000
20	30	530.64	0.959	80 000
20	40	548.85	0.992	80 000

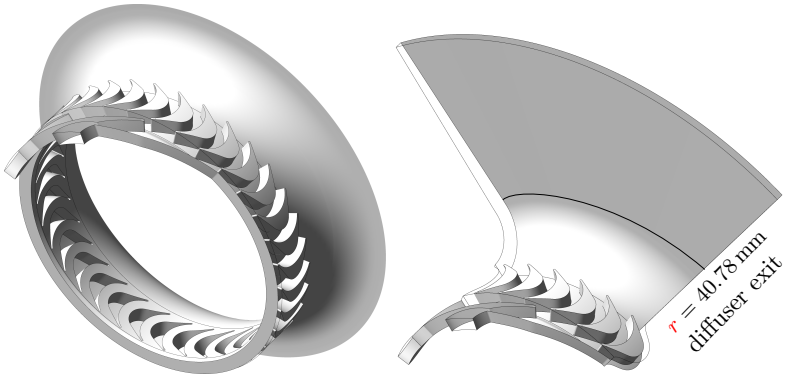

(a) full annulus (b) 72° sector

Figure 5.1: ORC turbine geometry for 20 % admission with 2 admitted stator nozzles and indication of the diffuser exit position (see also [210])

values of about 3 to 5 are encountered. For the final RANS mesh, a mesh independence study is conducted. To reduce the computational effort, only a 72° sector, as shown in fig. 5.1b, is considered based on ideal gas assumptions; see [210] for details. The number of nodes is uniformly increased in all directions, while maintaining the spacing at the walls and a constant expansion ratio of 1.1 in the boundary layer region. A total of 3 grids is considered regarding the isentropic total-to-static efficiency

$$\eta_{s,\mathrm{TS}} := \frac{H_{\mathrm{out}} - H_{\mathrm{in}}}{h_{s,\mathrm{out}} - H_{\mathrm{in}}}, \tag{5.1}$$

evaluated between domain inlet and averaged diffuser exit state, as shown in fig. 5.2. On this basis, the medium grid with about 4.3×10^6 internal cells for the 72° sector is selected as a good compromise between accuracy and computational effort. The final full annulus mesh contains 20.5×10^6 internal cells; mesh quality parameters are listed in table 5.5, an impression of the final mesh can be gained from fig. 5.3.

5.1.3 Results

Predicted mass flow rate and total-to-static isentropic efficiency for the three examined OPs with a 20 % admission are shown in fig. 5.4. The mass flow of the measurements are accurately matched for all three OPs. The mass flow

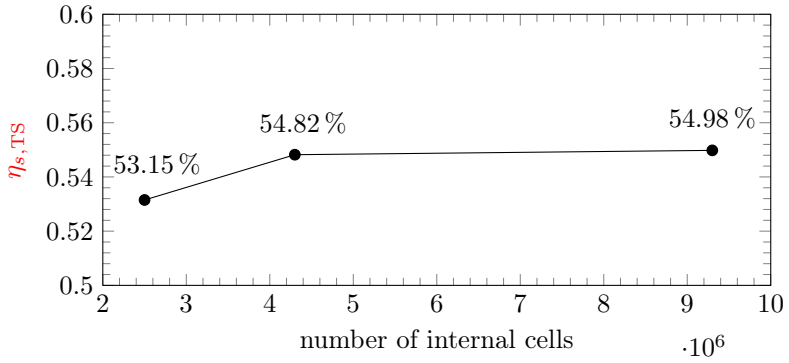

Figure 5.2: Mesh independence study on basis of a 72° sector of the ORC turbine test case (see also [210])

Table 5.5: Final grid statistics of the medium mesh used for the computation of the ORC turbine test case (see also [210])

	max. aspect ratio	max. expansion ratio	min. orthogonality [°]	internal cells [$\times 10^6$]
stator domain	598	2.8	29.4	1.0
rotor passage	473	2.0	21.0	0.6
72°				4.3
360°				20.5

is determined by the choked state in the stator nozzle throat and validates that this critical state is matched accurately by the implemented thermodynamic treatment. The efficiencies are also matched within the measurement accuracy, except for the OP with the highest pressure ratio, with a difference of about 5 p.p.. The same difference is also predicted by loss model based results in [160, 210] and might be the result of the boundary conditions being associated with relatively high degrees of uncertainty for this OP, especially regarding the total temperature [210]. This renders an investigation of unsteady effects based on URANS computations of this high pressure OP of particular relevance, to be conducted in the future on basis of the presented real gas solution method.

In the following, the predicted flow field characteristics of the medium pressure ratio OP are examined: Figure 5.5 shows the contours of the Mach number in the absolute frame of reference at mid span for the full annulus and a zoomed top view of about one third of the domain. The flow is acceler-

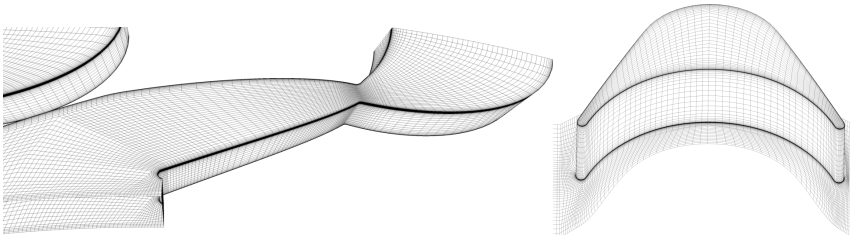

(a) stator nozzle (b) rotor passage

Figure 5.3: Details of the final ORC turbine mesh (see also [210])

ated in the stator section's Laval nozzle geometry, reaching about $M = 3.3$ at the exit. This leads to oblique shocks at the nozzle exit and in front of the rotor blades; however, the induced deceleration is not strong enough to bring the flow in the rotor passage to the subsonic regime. Within the rotor domain, the flow is further decelerated, reaching subsonic conditions towards the rotor exit plane. Due to the high pressure ratio, a trailing edge shock wave system emerges here. This pattern is only valid for directly admitted blades, as all other blades naturally show low flow velocities within the rotor passage.

To further assess the losses caused by the rotor's partial admission, a post-processing tool is created to allow direct access to the computation's thermodynamic setup. On this basis, the complete entropy field and the field of the entropy gradient norm are computed and shown in fig. 5.6 and fig. 5.7, respectively. To allow comparison to other equations of state, the entropy is presented with the reference state chosen as the total inlet state, rendering its presentation independent of the underlying reference state used in the thermodynamic description. Most notably, high levels of entropy are encountered within the rotor passages, which are not admitted. Here, energy is transferred from the rotor blades into the fluid, referred to as windage and rotor pumping losses. The mixing process between the stagnant flow and the flow through the admitted rotor passages at the rotor exit creates a high level of entropy, as evident from fig. 5.7. Further losses are associated with high wall frictions due to the very high velocities, the stator wakes, interacting with the rotor blades, and the strong oblique shock waves, especially in front of the admitted rotor leading edges. Of course, losses resulting from the tip gap also strongly contribute, are, however, not visible on the shown mid span planes. A more detailed analysis of losses and loss mechanisms and their association are given in [210].

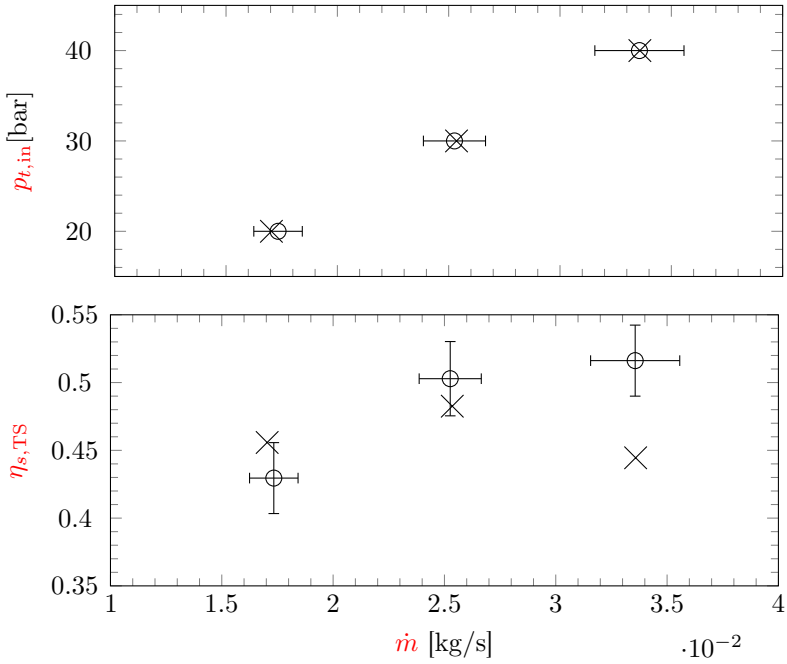

Figure 5.4: Comparison of computational results to measurement data for the ORC test case (see also [210])

5.2 Conclusion and outlook

In this chapter, the computational results of a partially admitted supersonic single stage ORC turbine test case are presented. The ethanol-water working medium is described by a real gas mixture based on the Peng-Robinson EoS and the van der Waals mixing rule. Steady state RANS results of the full annulus are computed by the FVM solver.

The mass flow is matched accurately in comparison to the measurement data given in [160]. At the same time, the efficiency is matched within the measurement uncertainty for two out of three considered operating points. For the OP with the highest pressure ratio the predicted efficiency is well outside the measurement uncertainty interval. This trend is also reported in the numerical results in [160] based on a passage computation with subsequent corrections due to the partial admission based on an empirical loss model. The discrepancy might be caused by a high degree of uncertainty related to

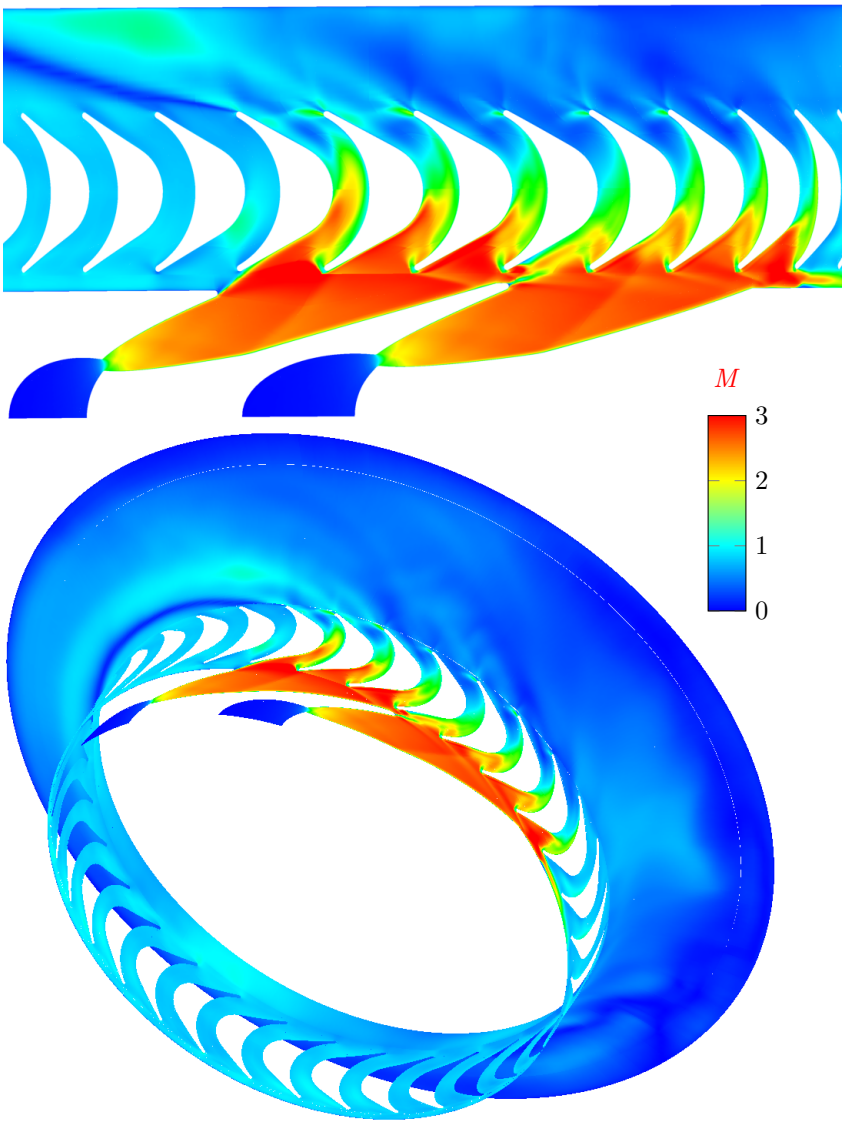

Figure 5.5: Contours of the Mach number in the absolute frame of reference at mid span for the medium pressure OP of the ORC test case

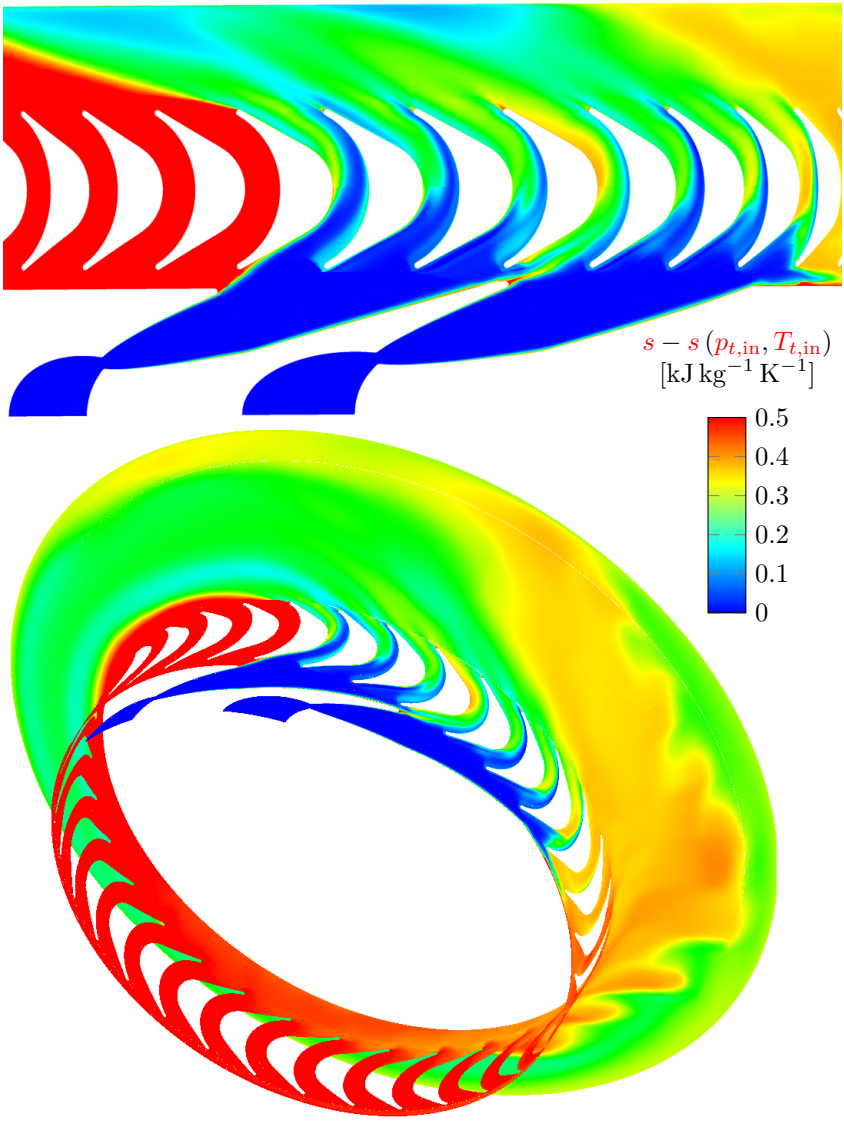

Figure 5.6: Contours of the entropy at mid span for the medium pressure OP of the ORC test case (see also [210])

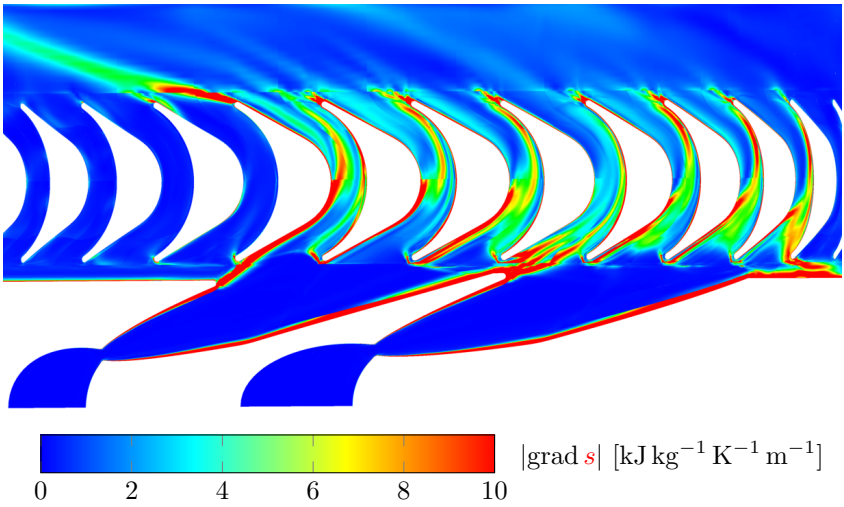

Figure 5.7: Contours of the entropy gradient norm at mid span for the medium pressure OP of the ORC test case (see also [210])

the inlet stagnation state. Based on the full annulus numerical results obtained by the presented FVM solver, a detailed description of the flow field is conducted. An analysis of loss mechanisms on basis of the presented results is presented in [210]. In this publication, a comparison to one-dimensional loss model based partial admission results is also reported.

In the presented computational results, unsteady effects have not yet been taken into account. These effects might play a very important role in the prediction of turbine performance. Therefore, transient full annulus computations, especially for the high pressure OP, will be conducted in the future. Furthermore, the OPs at 40 % admission are also still left to be investigated. The research in the field of ORC will also be expanded towards full real gas mixture computations and Bethe–Zel'dovich–Thompson (BZT) fluids. Real gas mixture capabilities are also important to other fields of fluid flows, as in rockets. Another example are humid air effects, which have also been investigated by the presented computational method in [76]. This field of research will further be perused.

6 Supercritical CO_2 Application

> *As the saying goes, the Stone Age did not end because we ran out of stones; we transitioned to better solutions. The same opportunity lies before us with energy efficiency and clean energy.*
>
> Steven Chu, American physicist and Nobel laureate, 2013

In this chapter, the application of the FVM solution method to the prediction of performance characteristics of a centrifugal supercritical CO_2 compressor are presented, based on the results published in [81], where the computations were conducted by the first author on basis of the FVM solver presented in this work. The compressor geometry is based on the main dimensions of the supercritical CO_2 compressor test loop operated and experimentally investigated at the Sandia National Laboratories (SNL) [201]. As the exact geometry is unavailable, only a qualitative comparison is possible. The thermodynamic data for the CO_2 working medium close to the critical point is provided by a special SBTL implementation, see [81] for details, where the tabulated data is based on the Span-Wagner EoS [168].

The operation of a Brayton cycle with CO_2 as working medium and a compression close to the critical point has seen a dramatic increase in interest over the last years. The big advantage of this cycle are high conversion efficiencies in the range $38\,\%$ to $50\,\%$ at relatively moderate maximum cycle temperatures at $450\,°C$ to $600\,°C$ [1]. This is realized by substantially reducing the compression work close to the critical point, i.e., in the area with the highest fluid densities, compared to a conventionally operated Brayton cycle with air. These high fluid densities also allow for a compact turbomachinery design with a small physical footprint. Detailed insight into this technology is, e.g., given in [15].

6.1 Supercritical CO_2 compressor test case

The main compressor of the supercritical CO_2 (sCO_2) test loop of the SNL [201] is designed with a backward swept impeller with splitter blades and

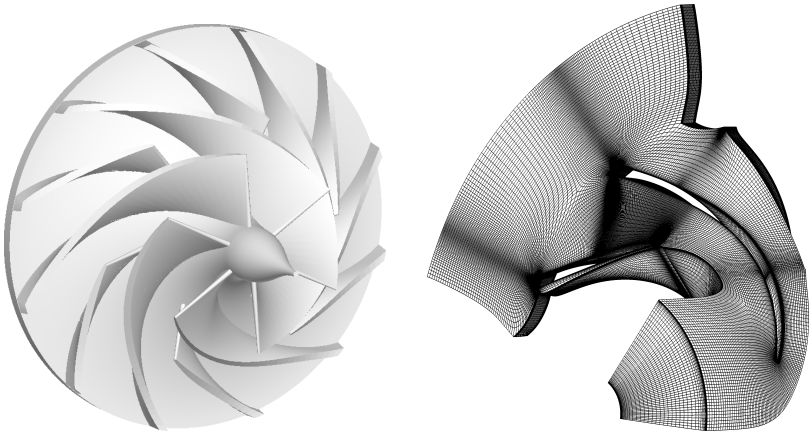

(a) (b)

Figure 6.1: Impeller wheel geometry and computational mesh for the supercritical CO_2 compressor test case (see also [81])

a channel type diffuser at the exit. The design point of the compressor is $T_{t,\mathrm{in}} = 305.3\,\mathrm{K}$ and $p_{t,\mathrm{in}} = 76.87\,\mathrm{bar}$, which equals to the reduced values $T_r = 1.004$ and $p_r = 1.042$. Obviously, the compressor is designed to be operated very close to the critical point. The rotational speed of the design point is $75\,000\,\mathrm{min}^{-1}$, the mass flow $3.5\,\mathrm{kg\,s}^{-1}$. Based on the total inlet state, flow coefficient and peripheral Mach number equal $\phi = 0.037$ and $M_u = 0.73$, respectively.

Results of performance tests are reported in [44, 201] for different operating conditions. According to information in [201], the compressor stage is equipped with resistance temperature detectors and total pressure transducers at the stage inlet and outlet; a static pressure tab is located at the impeller exit. The power is measured directly through the generated electrical power, mass flow and density by a Coriolis flow meter at the inlet of the compressor. Based on this equipment, the experimentally derived total-to-static isentropic efficiencies reported in [201] are interpreted as associated with the impeller exit

$$\eta_{s,\mathrm{TS}} := \frac{h_{s,\mathrm{out}} - H_{\mathrm{in}}}{H_{\mathrm{out}} - H_{\mathrm{in}}}. \tag{6.1}$$

As exact geometry data are unavailable, the geometry is generated based on the available data in literature, as described in [81]. In this work, only the impeller wheel shown in fig. 6.1a is considered, where the tip clearance is

neglected. The computational domain consists of a single, periodic passage with the main blade and a splitter blade, depicted in fig. 6.1b; the structured multi-block grid contains O-grid block topologies around the blades and H-grid blocks covering the upstream and downstream free-flow areas as well as the blade passages [81]. The total mesh comprises approximately 1.7 million cells with an appropriate near wall resolution.

For the conducted RANS computations, constant total pressure and total temperature are imposed at the inlet. For the used SA turbulence model, the turbulent viscosity ratio is prescribed. At the outlet, a constant static pressure is imposed; all walls are specified as adiabatic no-slip boundaries.

6.1.1 Results

The only experimental data available for this test case are performance maps. Wright et al. [201] provide a performance map for a state close to the critical point, including isentropic efficiency results. In addition to a similar near critical point, Fuller and Eisemann [44] report also performance maps for states close to saturated liquid, in the vapor range and for high temperature supercritical inlet conditions; however, all without efficiency data. These additional off design conditions are relevant for startup or for utilization of heat rejection temperatures [44]. In this work, two of these states are investigated:

- State A: $T_{t,\mathrm{in}} = 307\,\mathrm{K}$, $p_{t,\mathrm{in}} = 77.5\,\mathrm{bar}$
- State B: $T_{t,\mathrm{in}} = 301\,\mathrm{K}$, $p_{t,\mathrm{in}} = 67.9\,\mathrm{bar}$,

which are both illustrated in a Ts-chart in fig. 6.2. As indicated by the compressibility factor, both states are characterized by highly non-ideal gas behavior.

It must be noted that the experimental inlet conditions vary strongly during the measurements. For the near critical state (State A), [201] report a range of $p_{t,\mathrm{in}} = [77, 81.39]\,\mathrm{bar}$ and $T_{t,\mathrm{in}} = [304.3, 307]\,\mathrm{K}$, while [44] report $T_{t,\mathrm{in}} = [304, 306]\,\mathrm{K}$ and an approximated inlet density of $\varrho = 460\,\mathrm{kg/m^3}$. These ranges correspond to a significant change in fluid properties, shown here exemplary for the change in fluid density $\varrho = [344, 686]\,\mathrm{kg/m^3}$, which result obviously in drastic changes in terms of the mass flow rate. The chosen total inlet conditions for the computed state A are within the specified range.

Although being designed for a rotational speed of $75\,000\,\mathrm{min^{-1}}$, no data is reported for this design speed. Most data is given for $50\,000\,\mathrm{min^{-1}}$, for which all computations are performed.

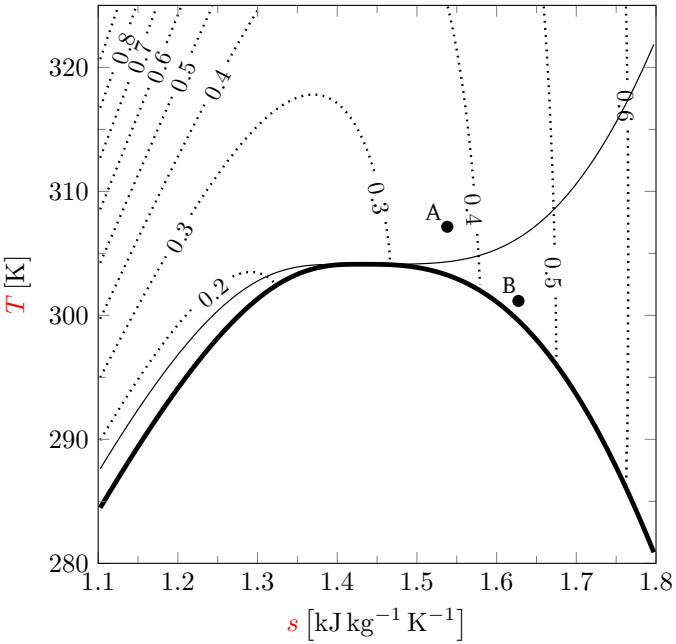

Figure 6.2: Ts-chart for CO_2 containing the two investigated states A and B; The contour lines illustrate the compressibility factor (see also [81])

6.1.1.1 Performance analysis

The numerically predicted performance curves for the near-critical operating point (state A) are shown in Figure 6.3. The performance characteristics are presented in non-dimensional form with the ideal head coefficient

$$\Psi := \left(h_{s,\mathrm{out}} - H_{\mathrm{in}}\right) / \underline{u}_{\mathrm{out}}^2 \tag{6.2}$$

and the flow coefficient

$$\phi := 4\dot{V}_{\mathrm{in}} / \left(\pi d_{\mathrm{out}}^2 \underline{u}_{\mathrm{out}}\right) . \tag{6.3}$$

The numerical data is compared to the experimental results of [44, 201], where the results in [201] are provided in dimensional form and converted on basis of the total inlet conditions, as the actual static state is unknown. Based on the RANS results, the difference between non-dimensionalization based on total quantities instead of the static state is estimated with about 1.1 % [81].

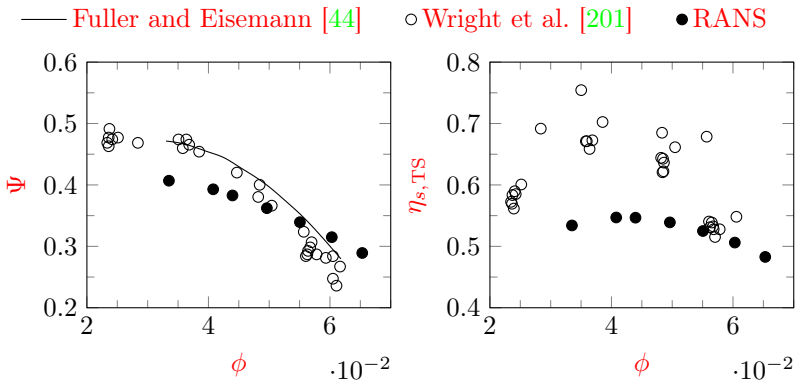

Figure 6.3: Impeller performance for state A compared to experimental data of [44, 201] (see also [81])

Both experimental data sets exhibit a similar qualitative shape, where the data of Wright et al. [201] reach the surge line at much lower flow coefficients. A very good quantitative agreement of the experimental data is found at about $\phi = 0.035$, moving towards higher flow coefficients an increasing deviation is visible. The RANS results predict a flatter characteristic curve compared to the experimental data; however, the numerical results are quantitatively reasonable and serve as a proof of concept. The differences compared to the experimental data can be explained with uncertainties regarding the exact geometry; the impeller geometry is modeled based on the main dimensions, but the detailed blade angle distribution is unknown, which can affect the head generation. Furthermore, the exact position of the static outlet pressure measurement is uncertain, where the position has a dramatic impact on the predicted static state. For the RANS computations, the impeller static outlet condition is obtained at a radial plane $r = 0.3\,\mathrm{mm}$, which is located in the real machine between impeller trailing and vaned diffuser leading edge. It also has to be noted that the operating range is not directly comparable, since the channel type diffuser is approximated by a vaneless diffuser in the computations. This is known to restrict the performance curve range; however, the surge point predicted by the RANS computation is comparable to that reported by Fuller and Eisemann [44].

The predicted impeller efficiency shows a maximum value of about $54.4\,\%$, which is more than ten percentage points lower compared to the peak values of the experiment. The scatter of the experimental data is obvious and is caused by transient behavior when the flow valve is closed. The predicted

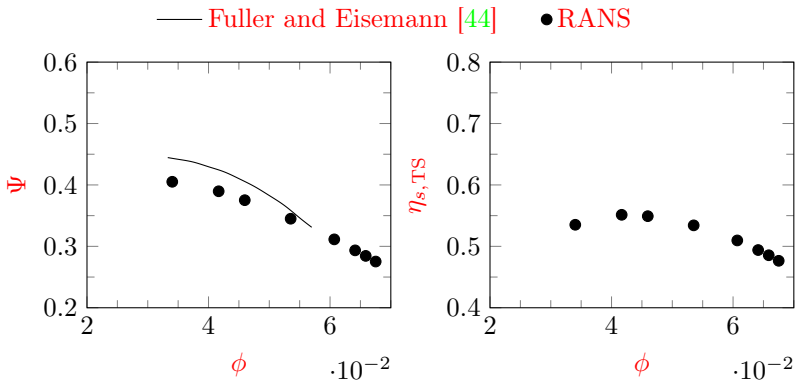

Figure 6.4: Impeller performance for state B compared to experimental data of [44] (see also [81])

efficiency curve shows an overall flatter shape compared to the experimental data. In addition to the previously mentioned limitations of the computation, it must be noted that the power measurements are corrected by loss factors, which might be associated with non-negligible uncertainties.

The evaluation of the performance curve for state B in the gas phase close to the saturation line is shown in fig. 6.4. Compared to the results for state A, no considerable differences can be identified for both, ideal head coefficient and isentropic efficiency. This indicates a high degree of machine similarity. However, the same degree of similarity is not found in the experimental data of Fuller and Eisemann [44], where the ideal head coefficient shows a flatter shape compared to the performance curve for the near-critical operating point (state A). This leads to a substantially better agreement between the numerical and experimental data for this operating point. Unfortunately, the efficiency curve has not been measured for this OP.

Overall, reasonable performance metrics are predicted by the computational method despite high uncertainties regarding geometry, instrumentation and operating conditions. The next section contains a more detailed analysis of the flow field.

6.1.1.2 Flow field analysis

Based on the previous findings, the flow field is further analyzed in this section. In all conducted homogeneous equilibrium mixture (HEM) computations for both operating points, flow regions with thermodynamic states in-

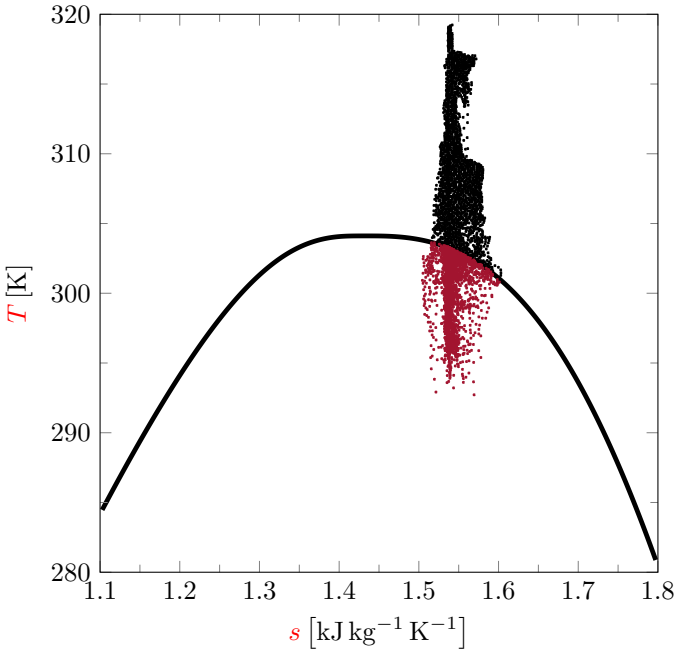

Figure 6.5: Ts-diagram containing the thermodynamic state of all control volumes of the computational domain for the near-critical computation with highest efficiency, where the red points lie within the two-phase region (see also [81])

side the two-phase region can be found. A scatter plot of the thermodynamic state within all cells for the computation with the highest efficiency for the near-critical operating point (state A) is shown in fig. 6.5. Obviously, for this computation, many cells encounter states inside the two-phase region during the compression in the impeller. These cells are primarily located at leading edge and suction side of the main blade and at the leading edge of the splitter blade, as can be seen from the isovolume representation in fig. 6.6. At these locations, the flow is accelerated to high Mach numbers (see fig. 6.7), which leads to a drop of static state values and to a penetration of the two-phase region. This observation is in line with the findings in [123, 144, 145].

To assess this behavior over the whole operating range for both inlet states, the volume fraction of cells with a state inside the two-phase region with respect to the total volume of the computational domain for both investigated

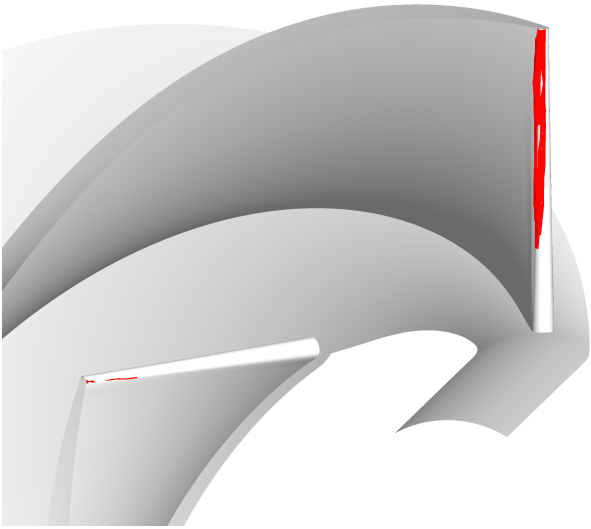

Figure 6.6: Isovolume of cells inside the two-phase region for the near-critical computation with highest efficiency (see also [81])

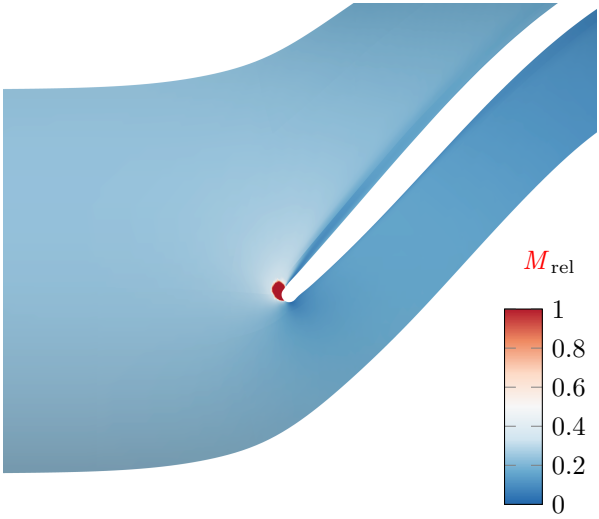

Figure 6.7: Contours of the relative Mach number at 75 % span of the impeller main blade for the near-critical computation and $\phi \approx 0.041$ (see also [81])

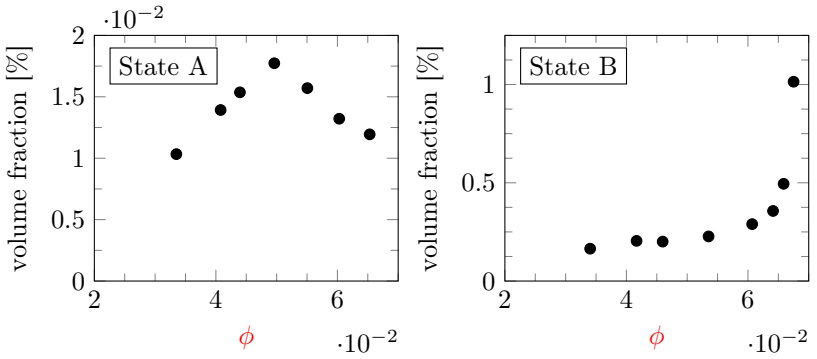

Figure 6.8: Evaluation of volume fraction of cells in the two-phase region for both considered operating conditions (see also [81])

operating points is evaluated in fig. 6.8. For the near-critical state A, this volume fraction is below $0.02\,\%$ for the investigated range. Despite higher flow coefficients connected with higher flow velocities, the volume fraction of cells inside the two-phase region peaks at about $\phi = 0.05$. This might be explained by increasing losses connected with an increase in temperature, which compensates the drop through higher flow velocities. For the subcritical state B, a different trend is observed. The evaluated volume fraction is overall larger compared to state A by more than an order of magnitude. In addition, an exponential increase in the volume fraction can be observed moving towards higher flow coefficients, with a maximum value as large as $1\,\%$ for the highest considered flow coefficient. Thus, the subcritical state B shows a higher potential for condensation, which is reasonable, as the inlet state is located closer to the saturation line compared to state A.

It has to be pointed out that the condensation process for this test case is not modeled accurately, as only a simple HEM is employed. In the real machine, a nucleation process takes place as explained in the wet steam chapter chapter 4. However, for its application to CO_2 in the reported range, the condensation modeling currently available in the solver has to be adapted and validated for the high pressure region close to the critical point. This will be subject of future research.

6.1.1.3 Evaluation of the computational speed

The assessment of the computational speed for the presented compressor test case at the near-critical operating point (state A) is presented in fig. 6.9.

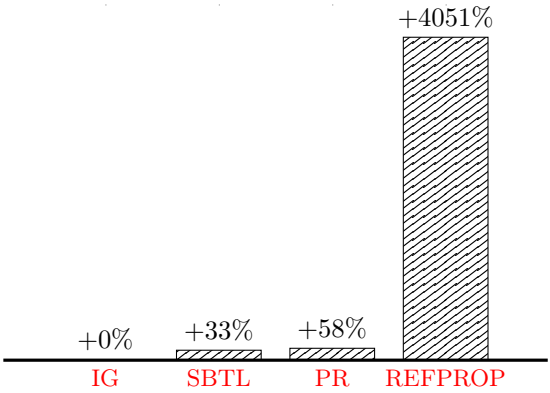

Figure 6.9: Evaluation of the computational speed of SBTL, PR and REFPROP (as implementation of the Span-Wagner EoS) relative to a baseline IG computation (see also [81])

It compares different real gas EoS implementations to a baseline IG computation. In addition to the SBTL tabulation method, which is used for all previously presented computations, the run time is also evaluated for the simple Peng-Robinson EoS (PR) and the REFPROP implementation, which is a highly optimized implementation of the Span-Wagner [168] multi-parameter EoS.

The SBTL shows an overhead of about 33 % compared to the IG computation, while the simple PR real gas EoS already leads to an overhead of about 58 %. A direct call to the multi-parameter EoS in the highly optimized REFPROP implementation is associated with an overhead of over 4000 %. Still, the SBTL implementation for CO_2 is much slower than the version for H_2O, which shows an overhead of only 2 % compared to IG for a steam turbine computation in fig. 4.6. This reveals that with additional optimization of the CO_2 implementation further gain in computational speed might be possible.

6.2 Conclusions and outlook

This chapter presents the adaption of the solution method to computations of flows with CO_2 as working medium, technically relevant especially close to the critical point. The thermodynamic data is provided by a new SBTL library implementation designed especially for such an application. The numerical method is used to show results for a supercritical CO_2 centrifugal

compressor test case.

The compressor geometry is modeled based on the available main dimensions of the SNL compressor loop. As the exact geometry is, however, not published, only a quantitative comparison to the experimental data is possible. In addition to an operating point close to the critical point, an inlet state inside the vapor region at high pressures close to the saturation line is considered. For both operating conditions, speed lines are numerically predicted based on RANS computations and compared to the available experimental data. The condensation process is not modeled accurately, as a simple HEM is used for the computation inside the two-phase region. For both operating conditions, the predicted non-dimensional performance curves are almost identical, indicating a high degree of machine similarity. At the same time, the results are in a reasonable range compared to the measurements, which serves as a proof of concept.

For all computations, cells with thermodynamic states inside the two-phase region can be found. These cells are located on leading edge and suction side of the main blade and on the leading edge of the splitter blade. Here, an acceleration of the flow leads to high Mach numbers causing a drop in terms of the static thermodynamic state, which yields a penetration of the two-phase region. This behavior is evaluated for the whole considered operating range, quantifying the volume fraction of cells inside the two-phase region with respect to the total volume of the computational domain. Overall, the operating point in the vapor phase shows much higher portions of cells with potential condensation. This appears reasonable, as the inlet state is closely located at the saturation line. At the same time, the near-critical inlet state shows a peak in this volume ratio. To improve the predictive nature of the results, computations including detailed modeling of the condensation process will be subject of future research.

The computational speed of the developed numerical method with thermodynamic data being provided by the SBTL tabulation is evaluated in comparison to other gas models, where a baseline IG computation serves as the benchmark. With an overhead of about 33 % compared to the IG computation, the SBTL based computation is still by 25 percentage points faster than a computation with the simple PR EoS. Compared to direct calls of the Span-Wagner multi-parameter EoS in REFPROP, the SBTL based computation is faster by over 4000 percentage points. At the same time, the tabulation provides an accuracy in the range of the uncertainties of the Span-Wagner EoS. Furthermore, there seems to be a speed up potential, as for H_2O an overhead of only 2 % compared to an IG computation is reported in fig. 4.6.

Overall, the computational method yields reasonable results for the supercritical CO_2 test case, while providing high accuracy at comparably low

computational costs. With further optimizations of the SBTL library implementation for CO_2, scale resolving computations can be targeted, as already realized for H_2O in this work. For such future investigations, the full condensation modeling will be necessary. This requires an adaption of the classical nucleation theory for the considered high pressures. The nozzle test case of Lettieri et al. [96] might serve as a validation test case. However, as all available test cases for CO_2, only pressure data is available, missing the required information about droplet sizes. On this basis, computations with a more accurate treatment of the condensation process will be conducted for the same test case. Of course, calculations with the exact geometry would be desirable, allowing a quantitative assessment of the results. Furthermore, computations of the complete stage with detailed modeling of the diffuser and with the tip gap will be conducted in the future.

7 Concluding Remarks

Science is eternal. It was started thousands of years ago and its progress is continuous. Principles that are deeply rooted are not likely to pass suddenly from the scene.

Theodore von Karman, 1963

Numerical modeling and simulation is central to modern industrial design and optimization. Virtualization of the whole product life cycle will increasingly require the intensive use of high-fidelity CFD simulations. The relevance of real gas effects in modern turbomachinery applications increases continuously with the demand for innovative net-zero power supply technologies, like ORC or supercritical CO_2 Brayton Cycles, in addition to traditional steam turbines. The design of computational methods for the accurate prediction of flows in such devices is very involved and subject of this work.

After an initial motivation for research in the field of compressible non-ideal gas flows in turbomachines, the mathematical model of a single-phase real gas flow with general expressions for state equation and constitutive relations is introduced. On this basis, RANS and LES approaches are discussed and an overview of relevant equations of state and tabulation techniques thereof are given. The current state-of-the-art in modeling of condensing wet steam flows is described, where the need for the investigation of the influence of the turbulence modeling approach for the overall predictability of wet steam modeling is highlighted.

On this basis, two solution methods are presented, a 2^{nd} order FVM and a high-order FDM solver, both targeted at application in high-speed compressible flows of non-ideal working media. For the computation of the advective fluxes, real gas extensions of Roe and AUSM+ schemes are discussed, followed by details about the solution strategy for scale resolving computations. The extension of the boundary treatment for real gas flows is outlined and details of a simple and a non-reflecting treatment for in- and outlet boundary conditions are presented. Finally, both solvers are validated for their application in scale resolving computations with a series of test cases.

The quality of the developed solution methods is demonstrated in applica-

tions to condensing wet steam flows, to ORC and supercritical CO_2 applications (an application to humid air flows is presented in [76]). For wet steam flows, the solution approach is chosen based on q3D inviscid computations of classical nozzle test cases, where the source term model in combination with the SBTL tabulation approach shows the highest potential for the application in more complex flow settings. Calibration and validation of the implementation is conducted by 3D laminar computations of nozzle flows with low Wilson point pressures. The overall agreement with the calibrated nucleation theory is within the known limitations of the current wet steam modeling standard. A considerable computational speed is obtained, where the SBTL method shows an overhead of only 2 % compared to a baseline IG computation, while a full condensation computation is only connected to an overhead of 26 %. RANS results of a turbomachinery configuration are presented next, for which reasonable agreement with experimental data is also reached. Finally, the first scale resolving LES computation in the field of wet steam flows is presented in this work. A highly accurate numerical treatment is adapted and proven appropriate for application in condensing wet steam flows. The quality of the LES results is demonstrated based on LES quality criteria and near wall resolution analysis. Overall, the LES results are much better able to reproduce the experimental data compared to RANS and URANS computations. The onset of nucleation and the shape of the pressure rise due to the condensation are only matched by LES, which is able to account for the unsteady interaction of "condensation shock" and pressure side shock wave. The findings prove that the inherently unsteady nature of the condensation process and its interaction with other unsteady flow phenomena, which still lack understanding today, cannot be investigated properly based on simple steady state computations. However, at the relatively moderate Reynolds numbers in the low-pressure turbine and in light of the continuously increasing computational power, high-fidelity, unsteady, scale-resolving simulation techniques such as LES hold the potential to address this research need and to improve future designs.

Next, results of a partially admitted supersonic single stage ORC turbine for heat recovery in automotive applications are presented, where the ethanol-water working medium is described by a real gas mixture based on the Peng-Robinson EoS and van der Waals mixing rule. Steady state RANS results of the full annulus are computed by the FVM solver, reproducing the measured mass flow rates accurately. The measured efficiency is matched within the measurement uncertainty for two out of three considered operating points, the discrepancy for the other point might be linked to high degrees of uncertainty related to inlet stagnation state and has also been witnessed in other numerical studies. Based on the full annulus numerical results obtained by

the presented FVM solver, a detailed description of the flow field is conducted.

Finally, the adaption of the solution method to the computation of a CO_2 flow close to critical conditions in a radial compressor is presented. The thermodynamic data is provided by the SBTL tabulation. The compressor geometry is modeled based on the available main dimensions of the SNL compressor loop; without the exact geometry only a quantitative comparison to the experimental data is possible. In addition to an operating point close to the critical point, an inlet state inside the vapor region at high pressures close to the saturation line is considered. For both operating conditions, speed lines are numerically predicted based on RANS computations and compared to the available experimental data. For now, the condensation process is not modeled accurately, as a simple HEM is used for the computation inside the two-phase region. For both operating conditions, the predicted non-dimensional performance curves are almost identical, indicating a high degree of machine similarity. At the same time, the results are in a reasonable range compared to the measurements, which serves as a proof of concept. For all computations, cells with thermodynamic states inside the two-phase regions can be found. These cells are located on leading edge and suction side of the main blade and on the leading edge of the splitter blade. Here, an acceleration of the flow leads to high Mach numbers causing a drop in terms of the static thermodynamic state, which yields a penetration of the two-phase region. In the CO_2 version, the SBTL library currently yields an overhead of about 33 % compared to a baseline IG computation, still much faster than every other simple real gas EoS. With further enhancements to the SBTL library and the description of condensation close to the critical point, scale resolving computations of supercritical CO_2 flows can be targeted.

To target DNS computations within more complex domains, the FDM solver needs to be extended for the treatment of non-uniform meshes based on the transformation to a computational grid. Generally, for scale resolving computations with both solution methods, the proper definition of the shock sensor represents a field of active research to which could be contributed. For more complex geometries, a solution method for unstructured girds is necessary. A simple node-based FVM solver with hybrid parallelization is currently under development and will serve as the basis for the development of high-order solvers on unstructured grids. For a highly accurate boundary treatment in real gas flows, the NSCBC boundary conditions have been adapted and need to be published. For the GPU architecture, the adaption of the SBTL method is necessary. Another subject of current research is the stable and efficient inversion of flux averages for arbitrarily complex EoS.

For the detailed understanding of the interaction of turbulence and wet

steam model in the description of turbulent condensing steam turbine flows, additional LES at different operating conditions need to be conducted. To further increase the overall quality of the modeling, a more sophisticated two-phase treatment might be targeted, though, computationally very challenging. Due to the small time steps in LES, an Euler-Lagrange treatment appears feasible and would provide the best description of the droplet-size spectrum, but efficient parallelization remains one of the main challenges. For steady state computations, quadrature based moment methods like QMOM will be implemented. For a further assessment of different wet steam EoS, a direct implementation of IAPWS-IF97 and other steam EoS will be done in the future, also targeted at application on GPUs. The largest obstacle connected with wet steam flows, however, remains to be the uncertainty connected to the classical nucleation theory. Research in this area will be conducted. Furthermore, the wet steam model will be extended to the high pressure region, not only for supercritical application in H_2O, but also in CO_2. Application of the solution method to the investigation of rotating instabilities in steam turbines based on the demonstrated LES capabilities might be of interest. Extension of the FVM solver to fluid–structure interaction (FSI) capabilities is currently in progress and will be applied to investigations in low pressure steam turbine stages.

In the presented ORC results, unsteady effects have not yet been taken into account. These effects might play a very important role in the prediction of turbine performance. Therefore, transient full annulus computations, especially for the high pressure OP, will be conducted in the future. Furthermore, conditions with lower levels of admission are also still left to be investigated. The research in the field of ORC will also be expanded towards full real gas mixture computations, also important to the research in geothermal steam applications, and Bethe–Zel'dovich–Thompson (BZT) fluids. Real gas mixture capabilities are also important to other fields of fluid flows, as in rockets. For further investigations in CO_2 flows close to the critical point, a validated treatment for condensing flows at high pressures will be necessary. The nozzle test case of Lettieri et al. [96] might serve as a validation test case. Of course, calculations with exact geometry would be desirable, allowing a quantitative assessment of the results. Furthermore, computations of the complete stage with detailed modeling of the diffuser and with the tip gap will be conducted in the future.

Other areas of research, which might be of interest for the application of the presented solution method, are real gas high-pressure combustion, design and investigation of N_2 turbines for fast-neutron reactors and research in the field of wet compression.

Acronyms

ADER arbitrary accuracy schemes based on derivative Riemann problems. 41
AUSM Advection Upstream Splitting Method. 3, 49, 83, 139

CBC Comte-Bellot and Corrsin [26]. 66, 71–74
CFD computational fluid dynamics. iii, 1, 2, 139
CFL number Courant–Friedrichs–Lewy number. 60, 72, 98, 103
CPU central processing unit. 2, 75, 80, 103

DG discontinuous Galerkin. 40
DHIT decay of homogeneous isotropic turbulence. 66, 71, 75, 76, 78
DNS direct numerical simulation. 2, 3, 6, 19, 20, 23, 26, 50, 60, 76, 77, 104, 141

EoS equation of state. 8, 9, 11, 13–16, 28, 30–32, 34, 50, 55, 57, 62, 63, 85, 87, 88, 93–95, 110, 113, 118, 119, 123, 127, 136, 137, 140–142, 144

FD finite difference solver, see 3.1.2. 66–71, 76–78
FDM finite difference method. 2, 3, 40, 43, 45, 47, 50, 51, 58, 60, 61, 139, 141
FSI fluid–structure interaction. 142
FV finite volume solver, see 3.1.1. 66–68, 71–78
FVM finite volume method. 3, 40, 41, 43, 47, 50, 51, 54, 58, 60, 61, 63, 101, 117, 123, 126, 127, 139–142

GPU graphics processing unit. 2, 47, 60, 61, 74, 75, 113, 141, 142

HEM homogeneous equilibrium mixture. 132, 135, 137, 141

IAPWS International Association for the Properties of Water and Steam. 30, 32–34, 85, 143, 144
IAPWS-95 IAPWS 1995 scientific formulation [188]. 32–34

IAPWS-IF97 IAPWS 1997 industrial formulation [189, 190]. 32–34, 82, 88, 113, 142
IBVP initial-boundary value problem. 3, 39, 40, 42, 43, 60, 61, 63
IG ideal gas. 87, 91, 92, 110, 136, 137, 140, 141

LES large eddy simulation. 2, 3, 6, 19, 20, 24, 26–30, 43, 50, 60, 74, 75, 80, 81, 85, 90, 92, 97, 98, 101–112, 139, 140, 142, 145
LF global Lax-Friedrichs flux splitting. 59, 67, 68, 70, 71
LLF local Lax-Friedrichs flux splitting. 59, 67, 68, 70, 71
LUSGS Lower-Upper Symmetric-Gauss-Seidel Method. 60, 84, 98, 118

MM mixture model. 85–88, 93–95
MUSCL Monotonic Upstream-centered Scheme for Conservation Laws [183]. 50, 58, 63, 68, 78

NASA National Aeronautics and Space Administration. 11, 119
NIST National Institute of Standards and Technology. 14, 144
NSCBC Navier-Stokes characteristic boundary conditions. 61, 141

ODE ordinary differential equation. 40, 44, 60
OP operating point. 97–99, 101, 105–109, 111, 117–121, 123–126, 132, 142
OpenFOAM OpenFOAM CFD solver. 85, 91, 93
ORC Organic Rankine Cycle. iii, 1–3, 14, 43, 115–126, 139, 140, 142

PDE partial differential equation. 5, 18, 39, 45, 54, 60
p.p. percentage point(s). 121
PR Peng-Robinson EoS. 136, 137

q3D quasi three-dimensional. 83, 85–90, 92–95, 97, 110, 140
QMOM quadrature method of moments. 29, 82, 113, 142

RANS Raynolds-averaged Navier-Stokes. 2, 3, 6, 19, 20, 23, 24, 27–29, 60, 80, 81, 85, 98, 99, 101–103, 105–109, 111, 112, 118, 120, 123, 129–132, 137, 139–141, 145
REFPROP NIST Reference Fluid Thermodynamic and Transport Properties Database [94]. 14, 16, 118, 136, 137
RMS root mean square. 77, 151

SA Spalart-Allmaras turbulence model [167]. 25, 88, 89, 98, 118, 129, 147

SBTL spline based table lookup method [87, 89]. 15, 33, 34, 75, 80, 85–95, 110, 113, 127, 136–138, 140, 141
sCO2 supercritical CO_2. 127
SGS subgrid scale. 21–23, 147–150
SM source term model. 85–95
SMOM standard method of moments. 29, 113
SNL Sandia National Laboratories. 127, 137, 141
STI shock-turbulence interaction. 2, 46, 51, 66

URANS unsteady RANS. 2, 19, 27–29, 60, 81, 101–103, 105–112, 121, 140

WALE Wall-Adapting Local Eddy-Viscosity LES model [119].
WENO weighted essentially non-oscillatory. 2, 50, 51, 58, 67, 68, 70, 71, 76, 78

Y88 Young's 1988 state equation [207]. 85–88, 93–95, 113

Symbols

Greek symbols

α	parameter of Young's [208] droplet growth model. 31, 90
α	dimensionless Helmholtz energy. 14, 147
α^0	ideal gas part of α. 14
α^r	residual part of α. 14
β	parameter of Young's [208] droplet growth model. 31, 32, 90
χ	cell shock sensor. 51, 103, 104
Δ	cutoff length scale. 20
ϵ	specific total energy density. 52, 62, 149
$\eta_{s,\mathrm{TS}}$	total-to-static isentropic efficiency. 120, 121, 123, 128, 131, 132
γ	isentropic exponent. 12, 23, 30, 31, 53, 54, 62, 67, 69, 75, 76
$\underline{\underline{\Lambda}}$	Eigenvalues matrix. 52, 53, 58
λ	thermal conductivity coefficient. 8, 16, 22, 24, 26, 31
λ	Taylor microscale. 71, 76–78, 150
λ^{sgs}	SGS conductivity coefficient. 23, 24
λ^t	turbulent conductivity coefficient. 26
μ	dynamic viscosity. 8, 16, 18, 22, 24, 26, 32, 77, 98
μ^{sgs}	SGS viscosity. 22–24
μ^t	turbulent viscosity. 25, 26
$\tilde{\mu}$	eddy-viscosity transport variable of the SA turbulence model. 98
Ω	domain. 41–43
ω	acentric factor. 119
ω	angular velocity. 17
Ω_i	control volume. 41, 42, 148
$\underline{\omega}$	vorticity. 51, 70, 76
$\underline{\Phi}$	numerical flux function. 42, 45, 48, 50, 51, 58, 59

ϕ	flow coefficient. 128, 130–132, 134, 135
Π	pressure function. 52, 55–57
$\underline{\varpi}$	specific momentum. 52
Ψ	ideal head coefficient. 130–132
ψ	face shock sensor. 51
ϱ	density. 6–9, 11, 12, 14, 15, 17, 18, 21–26, 33, 34, 37, 47, 48, 50, 52, 53, 56–58, 61–63, 65–67, 69, 70, 77, 107, 129, 149
ϱ_c	critical density. 14
ϱ_G	gas density. 30, 35–37
ϱ_L	liquid density. 30, 31, 34–36
ϱ_m	mixture density. 36
ϱ_r	reduced density. 14
σ	surface tension. 30, 31
$\underline{\underline{\tau}}$	viscous shear stress tensor. 7, 8, 18, 21–23, 25, 26, 37
τ	eddy turn-over time. 76, 77
$\underline{\underline{\tau}}^{\text{sgs}}$	SGS stress tensor. 21–23
$\underline{\underline{\tau}}^{t}$	turbulent stress tensor. 25, 26
$\underline{\underline{\check{\tau}}}$	computable stress tensor. 21–23, 25, 26
$\underline{\underline{\tau}}^{*}$	effective stress tensor. 23, 24, 26
θ	dilatation. 51, 76

Latin symbols

$\underline{\underline{A}}$	Jacobian Matrix of the advective fluxes. 52, 54–56, 58, 62
a	Helmholtz energy. 14, 33, 53, 54, 58, 65, 66, 75
c_p	heat capacity at constant pressure. 11, 12, 16, 23, 26, 31
c_v	heat capacity at constant volume. 11, 12, 15, 67
$\underline{w}_i$	approximated mean value of the conservative variables over the control volume Ω_i. 41, 42
d	diameter. 130
$\underline{D}_t$	turbulent diffusion. 21–23, 25, 26
$\underline{D}_v$	viscous diffusion. 21–23, 25, 26
E	specific total internal energy. 6–8, 21, 22, 25, 26, 52, 148, 149
e	specific internal energy. 7–9, 11, 12, 15, 17, 18, 21–26, 34, 36, 37, 43–45, 50, 52, 53, 57, 58, 63, 65, 148, 149
E_G	E of the gas phase. 37

e_G	e of the gas phase. 36, 37
e_L	e of the liquid phase. 36
E_m	E of the mixture. 36
e_m	e of the mixture. 36
E_{rel}	specific total internal energy in relative frame of reference. 17, 18
$\underline{\underline{F}}$	physical flux tensor. 6, 7, 21, 23, 25, 41, 43, 55, 149
$\bar{f}$	flux average. 62
$\underline{\underline{F}}^a$	advective part of $\underline{\underline{F}}$. 7, 8, 18, 21, 23, 25, 36, 37, 43–45, 49, 52, 54, 56, 58, 62
$\underline{\underline{F}}^d$	diffusive part of $\underline{\underline{F}}$. 7, 18, 21, 23, 25, 37, 43, 44
$\underline{\underline{F}}^{\text{sgs}}$	additional SGS fluxes. 21, 22
$\underline{\underline{F}}^t$	additional turbulent fluxes. 25
$\underline{\bar{f}}_{\varpi}$	momentum flux average. 62
$\underline{f}_{\text{centrifugal}}$	centrifugal forces. 17, 18
$\underline{f}_{\text{coriolis}}$	Coriolis forces. 17, 18
$\bar{f}_{\varrho}$	mass flux average. 62
$\bar{f}_{\epsilon}$	total energy flux average. 62
g	Gibbs energy. 33
H	specific total enthalpy. 47, 52, 53, 55–57, 64, 65, 149
h	specific enthalpy. 9, 11, 15, 22, 25, 34, 62–64, 66, 149
h_{fg}	specific enthalpy of evapuration. 30, 31, 37
H_G	H of the gas phase. 37
H_{in}	H at inlet. 120, 128, 130
H_{out}	H at outlet. 120, 128
$h_{s,\text{out}}$	h at outlet assuming an isentropic process. 120, 128, 130
$\underline{\underline{I}}$	identity tensor. 7, 8, 18, 21, 22, 24–26, 36, 37, 52, 53
J	nucleation rate per unit volume. 30, 35, 37, 149
J_c	classical formulation of J. 30
k	Boltzmann's constant. 30, 73, 74, 77
Kn	Knudsen number. 31
$\mathcal{L}$	length scale. 18
$\tilde{l}$	mean free path. 31, 32
M	molar mass. 11, 12, 65, 66, 69, 72, 78, 119, 122, 124, 134
$\dot{m}$	mass flow. 98, 123
$\dot{m}_c$	condensing mass flow per unit volume. 35, 37
m_D	droplet mass. 35
m_M	mass of one molecule. 30

$M_{s,\mathrm{out}}$	outlet isentropic Mach number. 97
M_t	turbulent Mach number. 75
$M_{t,0}$	initial turbulent Mach number. 76, 77
M_u	peripheral Mach number. 128
N	number of droplets per unit mass. 35–37
$\underline{\hat{n}}$	outward unit normal vector. 41, 42, 48, 49, 52–56, 58, 59, 62, 63
p	pressure. 7–9, 11, 12, 15, 18, 21, 23, 25, 26, 30–37, 47, 50, 52, 53, 57, 58, 61, 62, 64–67, 69, 86, 89, 91, 93, 94, 96, 100, 105, 109
p_c	critical pressure. 12, 13, 119
p_{out}	outlet pressure. 97, 119
p_r	reduced pressure. 12, 13, 118, 128
p_s	saturation pressure. 31, 34
p_t	total pressure. 63, 64, 84, 86, 89, 91–94, 96
$p_{t,\mathrm{in}}$	inlet total pressure. 97, 100, 105, 119, 123, 125, 128, 129
Pr	Prandtl number. 16, 31, 75
Pr^{sgs}	SGS Prandtl number. 23
Pr^t	turbulent Prandtl number. 26
$\underline{q}$	heat flux vector. 7, 8, 18, 21–23, 25, 26, 37, 55, 56
$\underline{q}^*$	effective heat flux vector. 23, 24, 26
$\underline{q}^{\mathrm{sgs}}$	SGS heat flux vector. 21–23
$\underline{q}^t$	turbulent heat flux vector. 25, 26
q_σ	surface tension coefficient. 90, 101
q_c	condensation coefficient. 30, 31
R	specific gas constant. 14, 30–32, 52, 53, 58, 59
r	radius. 17, 31, 35, 86, 89, 91, 93, 94, 96, 108, 120, 131
r_c	critical droplet radius. 30, 31, 35
R_u	universal gas constant. 11, 12, 34
Re	Reynolds number. 18, 19, 71, 85
$Re_{\lambda,0}$	initial Taylor-scale Reynolds number. 77
Re_λ	Taylor-scale Reynolds number. 71, 77
S	Sutherland temperature. 16, 31, 41, 42, 81
$\underline{s}$	source term vector. 6, 9, 15, 18, 34, 37, 41–44, 53, 63–67, 125, 126, 130, 133
$\mathrm{S_c}$	“condensation shock”. 106, 107
$\mathrm{S_p}$	pressure side shock wave at the trailing edge. 106, 107
$\underline{s}_{\mathrm{rel}}$	source terms for relative velocity formulation in the relative frame of reference. 18

S_s	suction side shock wave at the trailing edge. 106, 107
T	temperature. 8, 9, 11–16, 22–24, 26, 32–34, 50, 63, 76, 130, 133
t	time variable. 6, 20, 21, 24, 27, 31, 35–37, 41–44, 49, 54, 55, 67, 69–74, 76, 78
T_c	critical temperature. 12, 13, 119
T_G	gas temperature. 30–32
T_r	reduced temperature. 12–14, 118, 128
T_{ref}	reference temperature. 16
ΔT_s	subcooling. 31, 34, 36, 97
T_t	total temperature. 63, 64, 84, 92
$T_{t,\mathrm{in}}$	inlet total temperature. 97, 119, 125, 128, 129
$\mathcal{U}$	length scale. 18
$\underline{u}$	velocity. 6–8, 17, 21–26, 36, 37, 47, 48, 50–57, 61–67, 69, 70, 75–77, 130, 151
$\underline{u}_{\mathrm{e}}$	relative velocity. 17
$\underline{u}_{\mathrm{rel}}$	relative velocity. 17, 18
$\dot{V}$	volumetric flow rate. 130
v	specific volume. 9, 11, 13
$\underline{u}_{\mathrm{rms}}$	RMS velocity. 76, 77
$\underline{w}$	conservative variables vector. 6–8, 17, 21, 23, 25, 36, 37, 41–44, 49, 52–59, 62, 148
$\underline{w}_p$	primitive variables vector. 7, 63
$\underline{x}$	space variable. 6, 20, 21, 24, 27, 36, 37, 41–44, 49, 54, 55, 66–70, 77
$\underline{x}^+$	non-dimensional wall distances. 99, 102, 103, 118,
y	liquid phase mass (wetness) fraction. 35–37, 111
Z	compressibility factor. 12, 13

Bibliography

[1] Ahn, Y. et al. "Review of Supercritical CO2 Power Cycle Technology and Current Status of Research and Development." In: Nuclear Engineering and Technology 47.6 (2015), pp. 647–661. DOI: 10.1016/j.net.2015.06.009.

[2] Aitken, J. "Dust, Fogs, and Clouds." In: Nature 23.591 (1881), pp. 384–385. DOI: 10.1038/023384a0.

[3] Ameli, A. et al. "Numerical Sensitivity Analysis for Supercritical CO2 Radial Turbine Performance and Flow Field." In: Energy Procedia 129 (2017). 4th International Seminar on ORC Power Systems, pp. 1117–1124. DOI: 10.1016/j.egypro.2017.09.233.

[4] Anderson, J. Computational Fluid Dynamics. Vol. 1. McGraw-Hill Education, 1995.

[5] Anderson, J. D. Hypersonic and High-Temperature Gas Dynamics, Second Edition. Reston ,VA: American Institute of Aeronautics and Astronautics, 2006. DOI: 10.2514/4.861956.

[6] Bakhtar, F. et al. "Classical Nucleation Theory and Its Application to Condensing Steam Flow Calculations." In: Proceedings of the Institution of Mechanical Engineers, Part C: Journal of Mechanical Engineering Science 219.12 (2005), pp. 1315–1333. DOI: 10.1243/095440605X8379.

[7] Bakhtar, F. and Mohammadi Tochai, M. T. "An Investigation of Two-Dimensional Flows of Nucleating and Wet Steam by the Time-Marching Method." In: International Journal of Heat and Fluid Flow 2.1 (1980), pp. 5–18. DOI: 10.1016/0142-727X(80)90003-X.

[8] Bassi, F. and Rebay, S. "A High-Order Accurate Discontinuous Finite Element Method for the Numerical Solution of the Compressible Navier-Stokes Equations." In: Journal of Computational Physics 131.2 (1997), pp. 267–279. DOI: 10.1006/jcph.1996.5572.

[9] Binnie, A. M. and Woods, M. W. "The Pressure Distribution in a Convergent-Divergent Steam Nozzle." In: Proceedings of the Institution of Mechanical Engineers (1938), pp. 229–266. DOI: 10.1243/PIME_PROC_1938_138_015_02.

[10] Binnie, A. M., Green, J. R., and Southwell, R. V. "An Electrical Detector of Condensation in High-Velocity Steam." In: Proceedings of the Royal Society of London. Series A. Mathematical and Physical Sciences 181.985 (1942), pp. 134–154. DOI: 10.1098/rspa.1942.0067.

[11] Blaisdell, G. A., Spyropoulos, E. T., and Qin, J. H. "The Effect of the Formulation of Nonlinear Terms on Aliasing Errors in Spectral Methods." In: Applied Numerical Mathematics 21.3 (1996), pp. 207–219. DOI: 10.1016/0168-9274(96)00005-0.

[12] Blazek, J. Computational Fluid Dynamics: Principles and Applications. Boston, MA: Elsevier, 2015.

[13] Bogey, C. and Bailly, C. "A Family of Low Dispersive and Low Dissipative Explicit Schemes for Flow and Noise Computations." In: Journal of Computational Physics 194.1 (2004), pp. 194–214. DOI: 10.1016/j.jcp.2003.09.003.

[14] Brachet, M. E. et al. "Small-Scale Structure of the Taylor–Green Vortex." In: Journal of Fluid Mechanics 130 (1983), pp. 411–452. DOI: 10.1017/S0022112083001159.

[15] Brun, K., Friedman, P., and Dennis, R. Fundamentals and Applications of Supercritical Carbon Dioxide (SCO2) Based Power Cycles. Woodhead Publishing, 2017. 464 pp.

[16] Burcat, A. et al. Third Millenium Ideal Gas and Condensed Phase Thermochemical Database for Combustion (with Update from Active Thermochemical Tables). ANL-05/20. Argonne National Lab. (ANL), Argonne, IL (United States), 2005. DOI: 10.2172/925269.

[17] Callendar, H. L. "On the Steady Flow of Steam through a Nozzle or Throttle." In: Proceedings of the Institution of Mechanical Engineers 88.1 (1915), pp. 53–77. DOI: 10.1243/PIME_PROC_1915_088_007_02.

[18] Celik, I. B., Cehreli, Z. N., and Yavuz, I. "Index of Resolution Quality for Large Eddy Simulations." In: Journal of Fluids Engineering 127.5 (2005), pp. 949–958. DOI: 10.1115/1.1990201.

[19] Chung, T. H. et al. “Generalized Multiparameter Correlation for Nonpolar and Polar Fluid Transport Properties.” In: Industrial & Engineering Chemistry Research 27.4 (1988), pp. 671–679. DOI: 10.1021/ie00076a024.

[20] Cinnella, P. “Roe-Type Schemes for Dense Gas Flow Computations.” In: Computers & Fluids 35.10 (2006), pp. 1264–1281. DOI: 10.1016/j.compfluid.2005.04.007.

[21] Clausius, R. “Ueber Die Theoretische Bestimmung Des Dampfdruckes Und Der Volumina Des Dampfes Und Der Flüssigkeit.” In: Annalen der Physik 250.10 (1881), pp. 279–290. DOI: 10.1002/andp.18812501007.

[22] Cockburn, B. and Shu, C.-W. “Runge–Kutta Discontinuous Galerkin Methods for Convection-Dominated Problems.” In: Journal of Scientific Computing 16.3 (2001), pp. 173–261. DOI: 10.1023/A:1012873910884.

[23] Colella, P. and Glaz, H. M. “Efficient Solution Algorithms for the Riemann Problem for Real Gases.” In: Journal of Computational Physics 59.2 (1985), pp. 264–289.

[24] Collins, E. and Luke, E. “Fast Evaluation of Complex Equations of State.” In: Electronic Journal of Differential Equations (EJDE) [electronic only] 2013 (2013).

[25] Colonna, P. et al. “Real-Gas Effects in Organic Rankine Cycle Turbine Nozzles.” In: Journal of Propulsion and Power 24.2 (2008), pp. 282–294. DOI: 10.2514/1.29718.

[26] Comte-Bellot, G. and Corrsin, S. “Simple Eulerian Time Correlation of Full-and Narrow-Band Velocity Signals in Grid-Generated, ‘Isotropic’ Turbulence.” In: Journal of Fluid Mechanics 48.02 (1971), p. 273. DOI: 10.1017/S0022112071001599.

[27] Dawson, V. P. Engines and Innovation: Lewis Laboratory and American Propulsion Technology. National Aeronautics and Space Administration, Office of Management, Scientific and Technical Information Division, 1991. 296 pp.

[28] Denton, J. D. “Loss Mechanisms in Turbomachines.” In: ASME 1993 International Gas Turbine and Aeroengine Congress and Exposition. American Society of Mechanical Engineers Digital Collection, 2015. DOI: 10.1115/93-GT-435.

[29] Ducros, F. et al. “Large-Eddy Simulation of the Shock/Turbulence Interaction.” In: Journal of Computational Physics 152.2 (1999), pp. 517–549. DOI: 10.1006/jcph.1999.6238.

[30] Ducros, F. et al. “High-Order Fluxes for Conservative Skew-Symmetric-like Schemes in Structured Meshes: Application to Compressible Flows.” In: Journal of Computational Physics 161.1 (2000), pp. 114–139. DOI: 10.1006/jcph.2000.6492.

[31] Dykas, S. “Numerical Calculation of the Steam Condensing Flow.” In: TASK Quarterly : scientific bulletin of Academic Computer Centre in Gdansk 5.4 (2001), pp. 519–535.

[32] Dykas, S. and Wróblewski, W. “Two-Fluid Model for Prediction of Wet Steam Transonic Flow.” In: International Journal of Heat and Mass Transfer 60 (2013), pp. 88–94. DOI: 10.1016/j.ijheatmasstransfer.2012.12.024.

[33] Dykas, S., Wróblewski, W., and Łukowicz, H. “Prediction of Losses in the Flow through the Last Stage of Low-Pressure Steam Turbine.” In: International Journal for Numerical Methods in Fluids 53.6 (2007), pp. 933–945. DOI: 10.1002/fld.1313.

[34] Dykas, S. et al. “Experimental Study of Condensing Steam Flow in Nozzles and Linear Blade Cascade.” In: International Journal of Heat and Mass Transfer 80 (2015), pp. 50–57. DOI: 10.1016/j.ijheatmasstransfer.2014.09.010.

[35] Ekaterinaris, J. A. “High-Order Accurate, Low Numerical Diffusion Methods for Aerodynamics.” In: Progress in Aerospace Sciences 41.3-4 (2005), pp. 192–300. DOI: 10.1016/j.paerosci.2005.03.003.

[36] Fakhari, K. “Development of a Two-Phase Eulerian/Lagrangian Algorithm for Condensing Steam Flow.” In: 44th AIAA Aerospace Sciences Meeting and Exhibit. Aerospace Sciences Meetings. American Institute of Aeronautics and Astronautics, 2006.

[37] Fakhari, K. “Numerical Modeling and Investigation of Unsteady Phenomena in Condensing Flows of Industrial Steam Turbines.” Doctoral Thesis. Ruhr-Universität Bochum, 2010.

[38] Feiereisen, W. J., Reynolds, W. C., and Ferziger, J. H. “Numerical Simulation of a Compressible Homogeneous, Turbulent Shear Flow.” Ph.D. Thesis. Stanford, 1981.

[39] Fenghour, A., Wakeham, W. A., and Vesovic, V. "The Viscosity of Carbon Dioxide." In: Journal of Physical and Chemical Reference Data 27.1 (1998), pp. 31–44. DOI: 10.1063/1.556013.

[40] Ferziger, J. H. and Perić, M. Computational Methods for Fluid Dynamics. 3rd, rev. ed. Berlin ; New York: Springer, 2002. 423 pp.

[41] Fessler, T. E. FLUID: A Numerical Interpolation Procedure for Obtaining Thermodynamic and Transport Properties of Fluids. Technical Report NASA-TM-X-3572, E-9132. 1977, p. 26.

[42] Föll, F. et al. "On the Use of Tabulated Equations of State for Multi-Phase Simulations in the Homogeneous Equilibrium Limit." In: Shock Waves 29.5 (2019), pp. 769–793. DOI: 10.1007/s00193-019-00896-1.

[43] Fröhlich, J. and von Terzi, D. "Hybrid LES/RANS Methods for the Simulation of Turbulent Flows." In: Progress in Aerospace Sciences 44.5 (2008), pp. 349–377. DOI: 10.1016/j.paerosci.2008.05.001.

[44] Fuller, R. and Eisemann, K. "Centrifugal Compressor Off-Design Performance for Supercritical CO2." In: Boulder, Colorado, 2011.

[45] Fureby, C. and Tabor, G. "Mathematical and Physical Constraints on Large-Eddy Simulations." In: Theoretical and Computational Fluid Dynamics 9.2 (1997), pp. 85–102. DOI: 10.1007/s001620050034.

[46] Garnier, E., Adams, N., and Sagaut, P. Large Eddy Simulation for Compressible Flows. Red. by Chattot, J.-J. et al. Scientific Computation. Dordrecht: Springer Netherlands, 2009.

[47] Garnier, E. et al. "On the Use of Shock-Capturing Schemes for Large-Eddy Simulation." In: Journal of Computational Physics 153.2 (1999), pp. 273–311. DOI: 10.1006/jcph.1999.6268.

[48] Gatski, T. B. and Bonnet, J.-P. Compressibility, Turbulence and High Speed Flow. 2nd ed. Amsterdam ; Boston: Academic Press, 2013. 328 pp.

[49] Gerber, A. G. "Inhomogeneous Multifluid Model for Prediction of Nonequilibrium Phase Transition and Droplet Dynamics." In: Journal of Fluids Engineering 130.3 (2008), p. 031402. DOI: 10.1115/1.2844580.

[50] Gerber, A. G. "Two-Phase Eulerian/Lagrangian Model for Nucleating Steam Flow." In: Journal of Fluids Engineering 124.2 (2002), pp. 465–475. DOI: 10.1115/1.1454109.

[51] Gerber, A. G. and Kermani, M. J. "A Pressure Based Eulerian-Eulerian Multi-Phase Model for Non-Equilibrium Condensation in Transonic Steam Flow." In: International Journal of Heat and Mass Transfer 47.10–11 (2004), pp. 2217–2231. DOI: 10.1016/j.ijheatmasstransfer.2003.11.017.

[52] Gerber, A. G. and Mousavi, A. "Application of Quadrature Method of Moments to the Polydispersed Droplet Spectrum in Transonic Steam Flows with Primary and Secondary Nucleation." In: Applied Mathematical Modelling 31.8 (2007), pp. 1518–1533. DOI: 10.1016/j.apm.2006.04.011.

[53] Gerber, A. G. et al. "Predictions of Non-Equilibrium Phase Transition in a Model Low-Pressure Steam Turbine." In: Proceedings of the Institution of Mechanical Engineers, Part A: Journal of Power and Energy 221.6 (2007), pp. 825–835. DOI: 10.1243/09576509JPE456.

[54] Ghosal, S. and Moin, P. "The Basic Equations for the Large Eddy Simulation of Turbulent Flows in Complex Geometry." In: Journal of Computational Physics 118.1 (1995), pp. 24–37. DOI: 10.1006/jcph.1995.1077.

[55] Giles, M. UNSFLO: A Numerical Method for the Calculation of Unsteady Flow in Turbomachinery. Gas Turbine Laboratory, Massachusetts Institute of Technology, 1991.

[56] Giles, M. B. "Nonreflecting Boundary Conditions for Euler Equation Calculations." In: AIAA Journal 28.12 (1990), pp. 2050–2058. DOI: 10.2514/3.10521.

[57] Godlewski, E. and Raviart, P.-A. Numerical Approximation of Hyperbolic Systems of Conservation Laws. Springer Science & Business Media, 1996. 542 pp.

[58] Godunov, S. "A Finite Difference Scheme for Numerical Computation of the Discontinuous Wave Solutions of Equations of Fluid Dynamics." In: Math. Sb. 47 (1959), pp. 271–306.

[59] Grübel, M. et al. "Two-Phase Flow Modeling and Measurements in Low-Pressure Turbines—Part I: Numerical Validation of Wet Steam Models and Turbine Modeling." In: Journal of Engineering for Gas Turbines and Power 137.4 (2014), pp. 042602–042602. DOI: 10.1115/1.4028468.

[60] Guardone, A. and Vigevano, L. “Roe Linearization for the van Der Waals Gas.” In: Journal of Computational Physics 175.1 (2002), pp. 50–78. DOI: 10.1006/jcph.2001.6915.

[61] Guha, A. and Young, J. B. “Time-Marching Prediction of Unsteady Condensation Phenomena Due to Supercritical Heat Addition.” In: Turbomachinery : Latest Developments in a Changing Scene. London, UK: Institution of Mechanical Engineers, 1991, pp. 167–177.

[62] Harten, A. and Hyman, J. M. “Self Adjusting Grid Methods for One-Dimensional Hyperbolic Conservation Laws.” In: Journal of Computational Physics 50.2 (1983), pp. 235–269. DOI: 10.1016/0021-9991(83)90066-9.

[63] Hasini, H., Zamri, M., and Abd., N. “Numerical Modeling of Wet Steam Flow in Steam Turbine Channel.” In: Mechanical Engineering. Ed. by Gokcek, M. InTech, 2012. DOI: 10.5772/37394.

[64] Helmholtz, R. von. “Untersuchungen Über Dämpfe Und Nebel, Besonders Über Solche von Lösungen.” In: Annalen der Physik 263.4 (1886), pp. 508–543. DOI: 10.1002/andp.18862630403.

[65] Henderson, J. B. “Theory and Experiment in the Flow of Steam through Nozzles.” In: Proceedings of the Institution of Mechanical Engineers 84.1 (1913), pp. 253–322. DOI: 10.1243/PIME_PROC_1913_084_015_02.

[66] Hill, P. G. “Condensation of Water Vapour during Supersonic Expansion in Nozzles.” In: Journal of Fluid Mechanics 25.3 (1966), pp. 593–620. DOI: 10.1017/S0022112066000284.

[67] Hirsch, C. Numerical Computation of Internal and External Flows Fundamentals of Computational Fluid Dynamics. Oxford; Burlington, MA: Elsevier/Butterworth-Heinemann, 2007.

[68] Hirsch, C. Numerical Computation of Internal and External Flows. Volume 1: Fundamentals of Numerical Discretization. Vol. 1. 2 vols. Chichester, UK: John Wiley & Sons Ltd., 1988.

[69] Hirsch, C. Numerical Computation of Internal and External Flows. Volume 2: Computational Methods for Inviscid and Viscous Flows. Vol. 2. 2 vols. Chichester, UK: John Wiley & Sons Ltd., 1990.

[70] Hughes, F. R. et al. “A Comparison of Modeling Techniques for Polydispersed Droplet Spectra in Steam Turbines.” In: Journal of Engineering for Gas Turbines and Power 138.4 (2016), p. 042603.

[71] Hung, T. C., Shai, T. Y., and Wang, S. K. "A Review of Organic Rankine Cycles (ORCs) for the Recovery of Low-Grade Waste Heat." In: Energy 22.7 (1997), pp. 661–667. DOI: 10.1016/S0360-5442(96)00165-X.

[72] Hushmandi, N. B., Fridh, J. E., and Fransson, T. H. "Unsteady Forces of Rotor Blades in Full and Partial Admission Turbines." In: Journal of Turbomachinery 133.4 (2011). DOI: 10.1115/1.4002408.

[73] Huynh, H. T. "A Flux Reconstruction Approach to High-Order Schemes Including Discontinuous Galerkin Methods." In: 18th AIAA Computational Fluid Dynamics Conference. 0 vols. Fluid Dynamics and Co-Located Conferences. American Institute of Aeronautics and Astronautics, 2007. DOI: 10.2514/6.2007-4079.

[74] IAPWS. "Guideline on the Tabular Taylor Series Expansion (TTSE) Method for Calculation of Thermodynamic Properties of Water and Steam Applied to IAPWS-95 as an Example." available at the IAPWS website http://www.iapws.org. 2003.

[75] International Conference on the Properties of Steam, ed. The 1967 IFC Formulation for Industrial Use: A Formulation of the Thermodynamic Properties of Ordinary Water Substance. Düsseldorf: International Formulation Committee of the sixth International Conference on the Properties of Steam, 1967.

[76] Iseni, S. et al. "Numerical Analysis of the Influence of Air Humidity on a Transonic Compressor Stage." In: Proceedings of the International Gas Turbine Congress (IGTC) 2019 Tokyo, Japan. Paper No. ThAM16.1. Tokyo, Japan, 2019.

[77] Jiang, G.-S. and Shu, C.-W. "Efficient Implementation of Weighted ENO Schemes." In: Journal of Computational Physics 126.1 (1996), pp. 202–228. DOI: 10.1006/jcph.1996.0130.

[78] Jiang, G.-S. and Wu, C.-c. "A High-Order WENO Finite Difference Scheme for the Equations of Ideal Magnetohydrodynamics." In: Journal of Computational Physics 150.2 (1999), pp. 561–594. DOI: 10.1006/jcph.1999.6207.

[79] Johnsen, E. et al. "Assessment of High-Resolution Methods for Numerical Simulations of Compressible Turbulence with Shock Waves." In: Journal of Computational Physics 229.4 (2010), pp. 1213–1237. DOI: 10.1016/j.jcp.2009.10.028.

[80] Kantrowitz, A. “Nucleation in Very Rapid Vapor Expansions.” In: The Journal of Chemical Physics 19.9 (1951), pp. 1097–1100. DOI: 10.1063/1.1748482.

[81] Karaefe, R. E. et al. “Numerical Investigation of a Centrifugal Compressor for Supercritical CO2 Cycles.” Under Review. 2020.

[82] Kennedy, C. A. and Gruber, A. “Reduced Aliasing Formulations of the Convective Terms within the Navier–Stokes Equations for a Compressible Fluid.” In: Journal of Computational Physics 227.3 (2008), pp. 1676–1700. DOI: 10.1016/j.jcp.2007.09.020.

[83] Kermani, M. J. and Gerber, A. G. “A General Formula for the Evaluation of Thermodynamic and Aerodynamic Losses in Nucleating Steam Flow.” In: International Journal of Heat and Mass Transfer 46.17 (2003), pp. 3265–3278. DOI: 10.1016/S0017-9310(03)00096-6.

[84] Kopriva, D. A. and Kolias, J. H. “A Conservative Staggered-Grid Chebyshev Multidomain Method for Compressible Flows.” In: Journal of Computational Physics 125.1 (1996), pp. 244–261. DOI: 10.1006/jcph.1996.0091.

[85] Kosowski, K. et al. “Partial Admission Stages of High Efficiency for a Microturbine.” In: Advances in Vibration Engineering 2 (2014), pp. 441–448.

[86] Kruse, I. A. “IAPWS Industrial Formulation 1997 for the Thermodynamic Properties of Water and Steam.” In: Properties of Water and Steam/Zustandsgrö\s Sen von Wasser Und Wasserdampf. Springer, 1998, pp. 7–37.

[87] Kunick, M. Fast Calculation of Thermophysical Properties in Extensive Process Simulations with the Spline-Based Table Look-up Method (SBTL). Fortschritt-Berichte VDI. Reihe 6, Energietechnik. VDI Verlag GmbH, 2018.

[88] Kunick, M., Kretzschmar, H.-J., and Gampe, U. “Fast Calculation of Thermodynamic Properties of Water and Steam in Process Modelling Using Spline Interpolation.” In: Proceedings of 15th International Conference on the Properties of Water and Steam. 2008.

[89] Kunick, M. et al. “CFD Analysis of Steam Turbines with the IAPWS Standard on the Spline-Based Table Look-Up Method (SBTL) for the Fast Calculation of Real Fluid Properties.” In: Proceedings of ASME Turbo Expo 2015: Turbine Technical Conference and Exposition. Paper No. GT2015-43984. 2015.

[90] Larsson, J., Lele, S. K., and Moin, P. "Effect of Numerical Dissipation on the Predicted Spectra for Compressible Turbulence." Annual Research Briefs. Annual Research Briefs. Stanford University, Center for Turbulence Research, 2007.

[91] Lecompte, S. et al. "Review of Organic Rankine Cycle (ORC) Architectures for Waste Heat Recovery." In: Renewable and Sustainable Energy Reviews 47 (2015), pp. 448–461. DOI: 10.1016/j.rser.2015.03.089.

[92] Lee, S., Lele, S. K., and Moin, P. "Eddy Shocklets in Decaying Compressible Turbulence." In: Physics of Fluids A: Fluid Dynamics 3.4 (1991), pp. 657–664. DOI: 10.1063/1.858071.

[93] Lele, S. K. "Compact Finite Difference Schemes with Spectral-like Resolution." In: Journal of Computational Physics 103.1 (1992), pp. 16–42. DOI: 10.1016/0021-9991(92)90324-R.

[94] Lemmon, E. W. et al. NIST Standard Reference Database 23: Reference Fluid Thermodynamic and Transport Properties-REFPROP, Version 10.0, National Institute of Standards and Technology. 2018. DOI: https://dx.doi.org/10.18434/T4JS3C.

[95] Leschziner, M. A. and Drikakis, D. "Turbulence Modelling and Turbulent-Flow Computation in Aeronautics." In: Aeronautical Journal 106.1061 (2002), pp. 349–384.

[96] Lettieri, C. et al. "Characterization of Nonequilibrium Condensation of Supercritical Carbon Dioxide in a de Laval Nozzle." In: Journal of Engineering for Gas Turbines and Power 140.4 (2017), pp. 041701-041701–11. DOI: 10.1115/1.4038082.

[97] LeVeque, R. J. Finite Volume Methods for Hyperbolic Problems. Cambridge; New York: Cambridge University Press, 2002.

[98] Liberson, A. et al. "Calculation of 3D Condensing Flows in Nozzles and Turbine Stages." In: Proceedings of EPRI Nucleation Workshop. Rochester, New York, 1995.

[99] Lin, Z. and Yuan, X. "Numerical Modeling and High-Order Scheme for Wet Steam Flow." In: Proceedings of the Institution of Mechanical Engineers, Part C: Journal of Mechanical Engineering Science 230.11 (2016), pp. 1846–1860. DOI: 10.1177/0954406215584394.

[100] Liou, M.-S. "A Sequel to AUSM, Part II: AUSM+-up for All Speeds." In: Journal of Computational Physics 214.1 (2006), pp. 137–170. DOI: 10.1016/j.jcp.2005.09.020.

[101] Liou, M.-S. “A Sequel to AUSM: AUSM+.” In: Journal of Computational Physics 129.2 (1996), pp. 364–382. DOI: 10.1006/jcph.1996.0256.

[102] Liou, M.-S., Leer, B. V., and Shuen, J.-S. “Splitting of Inviscid Fluxes for Real Gases.” In: Journal of Computational Physics 87.1 (1990), pp. 1–24. DOI: 10.1016/0021-9991(90)90222-M.

[103] Liou, M.-S. and Steffen, C. J. “A New Flux Splitting Scheme.” In: Journal of Computational Physics 107.1 (1993), pp. 23–39. DOI: 10.1006/jcph.1993.1122.

[104] Mahmoudi, A., Fazli, M., and Morad, M. R. “A Recent Review of Waste Heat Recovery by Organic Rankine Cycle.” In: Applied Thermal Engineering 143 (2018), pp. 660–675. DOI: 10.1016/j.applthermaleng.2018.07.136.

[105] Martin, H. M. “A New Theory of the Steam Turbine.” In: Engineering 106 (1918), pp. 1–3, 53–55, 107–108, 161–162, 189–191, 245–246.

[106] Mcbride, B. J. G. Coefficients for Calculating Thermodynamic and Transport Properties of Individual Species. Technical Report NASA-TM-4513. 1993, p. 94.

[107] McDonald, J. E. “Homogeneous Nucleation of Vapor Condensation. I. Thermodynamic Aspects.” In: American Journal of Physics 30.12 (1962), pp. 870–877. DOI: 10.1119/1.1941841.

[108] McDonald, J. E. “Homogeneous Nucleation of Vapor Condensation. II. Kinetic Aspects.” In: American Journal of Physics 31.1 (1963), pp. 31–41. DOI: 10.1119/1.1969234.

[109] Menikoff, R. and Plohr, B. “The Riemann Problem for Fluid Flow of Real Materials.” In: Reviews of Modern Physics 61.1 (1989), pp. 75–130. DOI: 10.1103/RevModPhys.61.75.

[110] Miettinen, A. and Siikonen, T. “Application of Pressure- and Density-Based Methods for Different Flow Speeds.” In: International Journal for Numerical Methods in Fluids 79.5 (2015), pp. 243–267. DOI: 10.1002/fld.4051.

[111] Mills, A. F. and Seban, R. A. “The Condensation Coefficient of Water.” In: International Journal of Heat and Mass Transfer 10.12 (1967), pp. 1815–1827. DOI: 10.1016/0017-9310(67)90052-X.

[112] Misra, A. and Lund, T. S. "Evaluation of a Vortex-Based Subgrid Stress Model Using DNS Databases." In: Studying Turbulence Using Numerical Simulation Databases. Part 6; Proceedings of the 1996 Summer Program. 1996, pp. 359–366.

[113] Miyagawa, K. and Hill, P. G. "Rapid and Accurate Calculation of Water and Steam Properties Using the Tabular Taylor Series Expansion Method." In: Journal of engineering for gas turbines and power 123.3 (2001), pp. 707–712.

[114] Mollier, R. Neue Tabellen und Diagramme für Wasserdampf. Berlin, Heidelberg: Springer, 1906.

[115] Mondejar, M. E. et al. "A Review of the Use of Organic Rankine Cycle Power Systems for Maritime Applications." In: Renewable and Sustainable Energy Reviews 91 (2018), pp. 126–151. DOI: 10.1016/j.rser.2018.03.074.

[116] Moore, M. J. et al. "Predicting the Fog Drop Size in Wet Steam Turbines." In: Proceedings of IMECHE Conf. Wet Steam. Vol. 4. Coventry, UK, 1973, pp. 101–109.

[117] Moses, C. A. and Stein, G. D. "On the Growth of Steam Droplets Formed in a Laval Nozzle Using Both Static Pressure and Light Scattering Measurements." In: Journal of Fluids Engineering 100.3 (1978), pp. 311–322. DOI: 10.1115/1.3448672.

[118] Mottura, L., Vigevano, L., and Zaccanti, M. "An Evaluation of Roe's Scheme Generalizations for Equilibrium Real Gas Flows." In: Journal of Computational Physics 138.2 (1997), pp. 354–399. DOI: 10.1006/jcph.1997.5838.

[119] Nicoud, F. and Ducros, F. "Subgrid-Scale Stress Modelling Based on the Square of the Velocity Gradient Tensor." In: Flow, Turbulence and Combustion 62.3 (1999), pp. 183–200. DOI: 10.1023/A:1009995426001.

[120] Onischuk, A. A. et al. "Evaluation of Surface Tension and Tolman Length as a Function of Droplet Radius from Experimental Nucleation Rate and Supersaturation Ratio: Metal Vapor Homogeneous Nucleation." In: The Journal of Chemical Physics 124.1 (2006), p. 014506. DOI: 10.1063/1.2140268.

[121] Oswatitsch, K. "Kondensationserscheinungen in Überschalldüsen." In: ZAMM - Journal of Applied Mathematics and Mechanics / Zeitschrift für Angewandte Mathematik und Mechanik 22.1 (1942), pp. 1–14. DOI: 10.1002/zamm.19420220102.

[122] Pasquale, D., Ghidoni, A., and Rebay, S. "Shape Optimization of an Organic Rankine Cycle Radial Turbine Nozzle." In: Journal of Engineering for Gas Turbines and Power 135.4 (2013). DOI: 10.1115/1.4023118.

[123] Pecnik, R., Rinaldi, E., and Colonna, P. "Computational Fluid Dynamics of a Radial Compressor Operating With Supercritical CO2." In: Journal of Engineering for Gas Turbines and Power 134.12 (2012). DOI: 10.1115/1.4007196.

[124] Peng, D.-Y. and Robinson, D. B. "A New Two-Constant Equation of State." In: Industrial & Engineering Chemistry Fundamentals 15.1 (1976), pp. 59–64. DOI: 10.1021/i160057a011.

[125] Persico, G. and Pini, M. "8 - Fluid Dynamic Design of Organic Rankine Cycle Turbines." In: Organic Rankine Cycle (ORC) Power Systems. Ed. by Macchi, E. and Astolfi, M. Woodhead Publishing, 2017, pp. 253–297. DOI: 10.1016/B978-0-08-100510-1.00008-9.

[126] Pirozzoli, S. "Generalized Conservative Approximations of Split Convective Derivative Operators." In: Journal of Computational Physics 229.19 (2010), pp. 7180–7190. DOI: 10.1016/j.jcp.2010.06.006.

[127] Pirozzoli, S. "Numerical Methods for High-Speed Flows." In: Annual Review of Fluid Mechanics 43.1 (2011), pp. 163–194. DOI: 10.1146/annurev-fluid-122109-160718.

[128] Poinsot, T. J. and Lelef, S. K. "Boundary Conditions for Direct Simulations of Compressible Viscous Flows." In: Journal of Computational Physics 101.1 (1992), pp. 104–129. DOI: 10.1016/0021-9991(92)90046-2.

[129] Poinsot, T. and Veynante, D. Theoretical and Numerical Combustion. R.T. Edwards, Inc., 2005. 544 pp. Google Books: cqFDkeVABYoC.

[130] Poling, B. E., Prausnitz, J. M., O'connell, J. P., et al. The Properties of Gases and Liquids. Vol. 5. McGraw-Hill New York, 2001.

[131] Pope, S. B. Turbulent Flows. Cambridge ; New York: Cambridge University Press, 2000. 802 pp.

[132] Post, P. "Implementation and Validation of a Highly Efficient Thermodynamic Algorithm for the 3D-CFD Analysis of the Steam Flow in Turbomachinery." Master Thesis. Darmstadt: Technische Universität Darmstadt, 2015.

[133] Post, P. and di Mare, F. "Development Of A Highly Efficient Density-Based Solver For Condensing Steam Flows In Turbomachines." In: Proceedings of the 1st Global Power and Propulsion Forum GPPF 2017. Paper No. GPPF-2017-113. Zurich, Switzerland, 2017.

[134] Post, P. and di Mare, F. "Towards Direct Numerical Simulation of Shock-Turbulence Interaction in Real Gas Flows on GPUs: Initial Validation." In: Non-Ideal Compressible-Fluid Dynamics for Propulsion and Power. 2nd International Seminar on Non-Ideal Compressible-Fluid Dynamics for Propulsion & Power, NICFD 2018, October 4 – 5, 2018, Bochum, Germany. Lecture Notes in Mechanical Engineering. Springer International Publishing, 2020. DOI: 10.1007/978-3-030-49626-5.

[135] Post, P. and Mare, F. di. "Highly Efficient Euler-Euler Approach for Condensing Steam Flows in Turbomachines." In: Proceedings of Montreal 2018 Global Power and Propulsion Forum. Paper No. GPPS-NA-2018-106. Montreal, Canada, 2018.

[136] Post, P., Sembritzky, M., and di Mare, F. "Towards Scale Resolving Computations of Condensing Wet Steam Flows." In: Proceedings of the ASME Turbo Expo 2019: Turbomachinery Technical Conference and Exposition. Vol. 8: Microturbines, Turbochargers, and Small Turbomachines; Steam Turbines. Turbo Expo: Power for Land, Sea, and Air. Paper No. GT2019-91269. Phoenix, Arizona, USA: American Society of Mechanical Engineers Digital Collection, 2019. DOI: 10.1115/GT2019-91269.

[137] Post, P., Winhart, B., and di Mare, F. "Large Eddy Simulation of a Condensing Wet Steam Turbine Cascade." Under Review. 2020.

[138] Praneeth, S. and Hickey, J.-P. "Uncertainty Quantification of Tabulated Supercritical Thermodynamics for Compressible Navier-Stokes Solvers." In: (2018). arXiv: 1801.06562.

[139] Pulliam, T. H. and Steger, J. L. "Recent Improvements in Efficiency, Accuracy, and Convergence for Implicit Approximate Factorization Algorithms." In: AIAA paper 854360 (1985).

[140] Quartapelle, L. et al. "Solution of the Riemann Problem of Classical Gasdynamics." In: Journal of Computational Physics 190.1 (2003), pp. 118–140. DOI: 10.1016/S0021-9991(03)00267-5.

[141] Rahbar, K. et al. "Review of Organic Rankine Cycle for Small-Scale Applications." In: Energy Conversion and Management 134 (2017), pp. 135–155. DOI: 10.1016/j.enconman.2016.12.023.

[142] Ren, Y.-X., Liu, M., and Zhang, H. "A Characteristic-Wise Hybrid Compact-WENO Scheme for Solving Hyperbolic Conservation Laws." In: Journal of Computational Physics 192.2 (2003), pp. 365–386. DOI: 10.1016/j.jcp.2003.07.006.

[143] Rettaliata, J. T. "Undercooling in Steam Nozzles." In: TRANS. ASME 58 (1936), p. 599.

[144] Rinaldi, E., Pecnik, R., and Colonna, P. "Computational Fluid Dynamic Simulation of a Supercritical CO2 Compressor Performance Map." In: Journal of Engineering for Gas Turbines and Power 137.7 (2015), p. 072602. DOI: 10.1115/1.4029121.

[145] Rinaldi, E., Pecnik, R., and Colonna, P. "Steady State CFD Investigation of a Radial Compressor Operating With Supercritical CO2." In: Proceedings of the ASME Turbo Expo 2013: Turbomachinery Technical Conference and Exposition. ASME Turbo Expo 2013: Turbine Technical Conference and Exposition. Turbo Expo: Power for Land, Sea, and Air. Paper No. GT2013-94580. San Antonio, Texas, USA: American Society of Mechanical Engineers, 2013. DOI: 10.1115/GT2013-94580.

[146] Ritschel, T. K. S. et al. An Open-Source Thermodynamic Software Library. Technical Report 12. Technical University of Denmark (DTU), 2016, p. 27.

[147] Robens, S. et al. "Adaption of Giles Non-Local Non-Reflecting Boundary Conditions for a Cell-Centered Solver for Turbomachinery Applications." In: ASME Turbo Expo 2013: Turbine Technical Conference and Exposition. American Society of Mechanical Engineers, 2013.

[148] Roe, P. L. "Approximate Riemann Solvers, Parameter Vectors, and Difference Schemes." In: Journal of Computational Physics 43.2 (1981), pp. 357–372. DOI: 10.1016/0021-9991(81)90128-5.

[149] Rogallo, R. S. Numerical Experiments in Homogeneous Turbulence. NASA Tech. Memo. 81315. 1981.

[150] Rubino, A. et al. "A Look-up Table Method Based on Unstructured Grids and Its Application to Non-Ideal Compressible Fluid Dynamic Simulations." In: Journal of Computational Science 28 (2018), pp. 70–77. DOI: 10.1016/j.jocs.2018.08.001.

[151] Sagaut, P. and Meneveau, C. Large Eddy Simulation for Incompressible Flows. Berlin [u.a.]: Springer, 2006.

[152] Sanders, R., Morano, E., and Druguet, M.-C. "Multidimensional Dissipation for Upwind Schemes: Stability and Applications to Gas Dynamics." In: Journal of Computational Physics 145.2 (1998), pp. 511–537. DOI: 10.1006/jcph.1998.6047.

[153] Sandham, N. D., Li, Q., and Yee, H. C. "Entropy Splitting for High-Order Numerical Simulation of Compressible Turbulence." In: Journal of Computational Physics 178.2 (2002), pp. 307–322. DOI: 10.1006/jcph.2002.7022.

[154] Saurel, R., Larini, M., and Loraud, J. C. "Exact and Approximate Riemann Solvers for Real Gases." In: Journal of Computational Physics 112.1 (1994), pp. 126–137. DOI: 10.1006/jcph.1994.1086.

[155] Saxer, A. and Giles, M. "Quasi-Three-Dimensional Nonreflecting Boundary Conditions for Euler Equations Calculations." In: Journal of Propulsion and Power 9.2 (1993), pp. 263–271. DOI: 10.2514/3.23618.

[156] Scalabrin, G. et al. "A Reference Multiparameter Thermal Conductivity Equation for Carbon Dioxide with an Optimized Functional Form." In: Journal of Physical and Chemical Reference Data 35.4 (2006), pp. 1549–1575. DOI: 10.1063/1.2213631.

[157] Schmidt, E. VDI-Wasserdampftafeln / VDI-Steam Tables / Tables VDI des constantes. Berlin, Heidelberg: Springer Berlin Heidelberg, 1963.

[158] Schmidt, E., Koch, W., and Ingenieure, V. D. VDI-Wasserdampftafeln: VDI Steam Tables. Tables VDI de La Vapeur d'eau. Bis 800°C Und 1000 at. Kcal, At. Springer, 1968. 206 pp.

[159] Senoo, S. and White, A. J. "Analysis and Design of Wet-Steam Stages." In: Advances in Steam Turbines for Modern Power Plants. Woodhead Publishing, 2017, pp. 165–218.

[160] Seume, J. R., Peters, M., and Kunte, H. "Design and Test of a 10kW ORC Supersonic Turbine Generator." In: Journal of Physics: Conference Series 821 (2017), p. 012023. DOI: 10.1088/1742-6596/821/1/012023.

[161] Shu, C.-W. "Essentially Non-Oscillatory and Weighted Essentially Non-Oscillatory Schemes for Hyperbolic Conservation Laws." In: Cockburn, B. et al. Advanced Numerical Approximation of Nonlinear Hyperbolic Equations. Ed. by Quarteroni, A. Vol. 1697. Berlin,

Heidelberg: Springer Berlin Heidelberg, 1998, pp. 325–432. DOI: 10.1007/BFb0096355.

[162] Shu, C.-W. and Osher, S. "Efficient Implementation of Essentially Non-Oscillatory Shock-Capturing Schemes, II." In: Journal of Computational Physics 83.1 (1989), pp. 32–78. DOI: 10.1016/0021-9991(89)90222-2.

[163] Shu, C.-W. et al. "Numerical Convergence Study of Nearly Incompressible, Inviscid Taylor–Green Vortex Flow." In: Journal of Scientific Computing 24.1 (2005), pp. 1–27. DOI: 10.1007/s10915-004-5407-y.

[164] Skillings, S. A. and Jackson, R. "A Robust 'Time-Marching' Solver for One-Dimensional Nucleating Steam Flows." In: International Journal of Heat and Fluid Flow 8.2 (1987), pp. 139–144. DOI: 10.1016/0142-727X(87)90014-2.

[165] Smagorinsky, J. "General Circulation Experiments with the Primitive Equations." In: Monthly Weather Review 91.3 (1963), pp. 99–164. DOI: 10.1175/1520-0493(1963)091<0099:GCEWTP>2.3.CO;2.

[166] Soave, G. "Equilibrium Constants from a Modified Redlich-Kwong Equation of State." In: Chemical Engineering Science 27.6 (1972), pp. 1197–1203. DOI: 10.1016/0009-2509(72)80096-4.

[167] Spalart, P. and Allmaras, S. "A One-Equation Turbulence Model for Aerodynamic Flows." In: 30th Aerospace Sciences Meeting and Exhibit. 0 vols. Aerospace Sciences Meetings. American Institute of Aeronautics and Astronautics, 1992. DOI: 10.2514/6.1992-439.

[168] Span, R. and Wagner, W. "A New Equation of State for Carbon Dioxide Covering the Fluid Region from the Triple-Point Temperature to 1100 K at Pressures up to 800 MPa." In: Journal of Physical and Chemical Reference Data 25.6 (1996), pp. 1509–1596. DOI: 10.1063/1.555991.

[169] Spurk, J. H. and Aksel, N. Fluid mechanics. Berlin: Springer, 2008.

[170] Starzmann, J. et al. "Numerical Investigation of Boundary Layers in Wet Steam Nozzles." In: Journal of Engineering for Gas Turbines and Power 139.1 (2016). DOI: 10.1115/1.4034213.

[171] Starzmann, J. et al. "Results of the International Wet Steam Modeling Project." In: Proceedings of the Institution of Mechanical Engineers, Part A: Journal of Power and Energy 232.5 (2018), pp. 550–570. DOI: 10.1177/0957650918758779.

[172] Stastny, M. and Sejna, M. “Numerical Modelling the Flow with Parallel Homogeneous and Heterogeneous Condensation in Steam Turbine Cascades.” In: Proceedings of ABB Seminar on Condensing Flows in Steam Turbines. Baden, Switzerland, 1997.

[173] Stodola, A. Dampf- und Gasturbinen: Mit Einem Anhang über die Aussichten der Wärmekraftmaschinen. 1924.

[174] Stodola, A. “Undercooling of Steam through Nozzle.” In: Engineering (1915), pp. 643–646.

[175] Sutherland, W. “The Viscosity of Gases and Molecular Force.” In: The London, Edinburgh, and Dublin Philosophical Magazine and Journal of Science 36.223 (1893), pp. 507–531. DOI: 10.1080/14786449308620508.

[176] Tam, C. K. W. and Webb, J. C. “Dispersion-Relation-Preserving Finite Difference Schemes for Computational Acoustics.” In: Journal of Computational Physics 107.2 (1993), pp. 262–281. DOI: 10.1006/jcph.1993.1142.

[177] Tartière, T. and Astolfi, M. “A World Overview of the Organic Rankine Cycle Market.” In: Energy Procedia. 4th International Seminar on ORC Power Systems 129 (2017), pp. 2–9. DOI: 10.1016/j.egypro.2017.09.159.

[178] Taylor, G. I. “The Spectrum of Turbulence.” In: Proceedings of the Royal Society of London A: Mathematical, Physical and Engineering Sciences 164.919 (1938), pp. 476–490. DOI: 10.1098/rspa.1938.0032.

[179] Taylor, G. I. and Green, A. E. “Mechanism of the Production of Small Eddies from Large Ones.” In: Proceedings of the Royal Society of London. Series A - Mathematical and Physical Sciences 158.895 (1937), pp. 499–521. DOI: 10.1098/rspa.1937.0036.

[180] Thorade, M. and Saadat, A. “Partial Derivatives of Thermodynamic State Properties for Dynamic Simulation.” In: Environmental Earth Sciences 70.8 (2013), pp. 3497–3503. DOI: 10.1007/s12665-013-2394-z.

[181] Toro, E. F. Riemann Solvers and Numerical Methods for Fluid Dynamics a Practical Introduction. Dordrecht; New York: Springer, 2009.

[182] Toumi, I. “A Weak Formulation of Roe’s Approximate Riemann Solver.” In: Journal of computational physics 102.2 (1992), pp. 360–373.

[183] Van Leer, B. "Towards the Ultimate Conservative Difference Scheme. V. A Second-Order Sequel to Godunov's Method." In: Journal of Computational Physics 32.1 (1979), pp. 101–136. DOI: 10.1016/0021-9991(79)90145-1.

[184] Vermeire, B. C., Nadarajah, S., and Tucker, P. G. "Implicit Large Eddy Simulation Using the High-Order Correction Procedure via Reconstruction Scheme." In: International Journal for Numerical Methods in Fluids 82.5 (2016), pp. 231–260. DOI: 10.1002/fld.4214.

[185] Vinokur, M. "An Analysis of Finite-Difference and Finite-Volume Formulations of Conservation Laws." In: Journal of Computational Physics 81.1 (1989), pp. 1–52. DOI: 10.1016/0021-9991(89)90063-6.

[186] Visbal, M. and Gaitonde, D. "Shock Capturing Using Compact-Differencing-Based Methods." In: 43rd AIAA Aerospace Sciences Meeting and Exhibit. 0 vols. Aerospace Sciences Meetings. American Institute of Aeronautics and Astronautics, 2005. DOI: 10.2514/6.2005-1265.

[187] Waals, J. D. van der. "Over de continuiteit van den gas- en vloeistoftoestand." Leiden: A.W. Sijthoff, 1873.

[188] Wagner, W. and Pruß, A. "The IAPWS Formulation 1995 for the Thermodynamic Properties of Ordinary Water Substance for General and Scientific Use." In: Journal of Physical and Chemical Reference Data 31.2 (2002), pp. 387–535. DOI: 10.1063/1.1461829.

[189] Wagner, W. et al. "The IAPWS Industrial Formulation 1997 for the Thermodynamic Properties of Water and Steam." In: Journal of Engineering for Gas Turbines and Power 122.1 (2000), pp. 150–184. DOI: 10.1115/1.483186.

[190] Wagner, W. and Kretzschmar, H.-J. International Steam Tables. Berlin, Heidelberg: Springer Berlin Heidelberg, 2008.

[191] Wang, J., Liang, C., and Miesch, M. S. "A Compressible High-Order Unstructured Spectral Difference Code for Stratified Convection in Rotating Spherical Shells." In: Journal of Computational Physics 290 (2015), pp. 90–111. DOI: 10.1016/j.jcp.2015.02.047.

[192] Wang, Z. J. "High-Order Methods for the Euler and Navier–Stokes Equations on Unstructured Grids." In: Progress in Aerospace Sciences 43.1 (2007), pp. 1–41. DOI: 10.1016/j.paerosci.2007.05.001.

[193] Wang, Z. J. et al. “High-Order CFD Methods: Current Status and Perspective.” In: International Journal for Numerical Methods in Fluids 72.8 (2013), pp. 811–845. DOI: 10.1002/fld.3767.

[194] Wang, Z. “Spectral (Finite) Volume Method for Conservation Laws on Unstructured Grids. Basic Formulation.” In: Journal of Computational Physics 178.1 (2002), pp. 210–251. DOI: 10.1006/jcph.2002.7041.

[195] Wang, Z. et al. “Spectral Volume and Spectral Difference Methods.” In: Handbook of Numerical Analysis. Vol. 17. Elsevier, 2016, pp. 199–226. DOI: 10.1016/bs.hna.2016.09.013.

[196] Weiß, A. P. “Volumetric Expander Versus Turbine - Which Is the Better Choice for Small ORC Plants?” In: 3rd International Seminar on ORC Power Systems. Brussels, Belgium, 2015.

[197] White, A. J., Young, J. B., and Walters, P. T. “Experimental Validation of Condensing Flow Theory for a Stationary Cascade of Steam Turbine Blades.” In: Philosophical Transactions of the Royal Society of London A: Mathematical, Physical and Engineering Sciences 354.1704 (1996), pp. 59–88. DOI: 10.1098/rsta.1996.0003.

[198] Wilcox, D. C. Turbulence Modeling for CFD. La Cañada, CA, USA: DCW Industries, 2006.

[199] Wilson, C. T. R. “Condensation of Water Vapour in the Presence of Dust-Free Air and Other Gases.” In: Proceedings of the Royal Society of London 61 (1897), pp. 240–242.

[200] Witherden, F., Vincent, P., and Jameson, A. “High-Order Flux Reconstruction Schemes.” In: Handbook of Numerical Analysis. Vol. 17. Elsevier, 2016, pp. 227–263. DOI: 10.1016/bs.hna.2016.09.010.

[201] Wright, S. A. et al. Operation and Analysis of a Supercritical CO2 Brayton Cycle. SAND2010-0171, 984129. 2010. DOI: 10.2172/984129.

[202] Wróblewski, W., Dykas, S., and Chmielniak, T. “Models for Water Steam Condensing Flows.” In: Archives of Thermodynamics 33.1 (2012). DOI: 10.2478/v10173-012-0003-2.

[203] Wróblewski, W., Dykas, S., and Gepert, A. “Steam Condensing Flow Modeling in Turbine Channels.” In: International Journal of Multiphase Flow 35.6 (2009), pp. 498–506. DOI: 10.1016/j.ijmultiphaseflow.2009.02.020.

[204] Xia, G., Li, D., and Merkle, C. L. "Consistent Properties Reconstruction on Adaptive Cartesian Meshes for Complex Fluids Computations." In: Journal of Computational Physics 225.1 (2007), pp. 1175–1197. DOI: 10.1016/j.jcp.2007.01.034.

[205] Yellot, J. "Supersaturated Steam." In: TRANS. ASME 56 (1934), pp. 411–430.

[206] Yellott, J. I. and Holland, C. K. "The Condensation of Flowing Steam." In: TRANS. ASME 59 (1937), pp. 171–183.

[207] Young, J. B. "An Equation of State for Steam for Turbomachinery and Other Flow Calculations." In: Journal of Engineering for Gas Turbines and Power 110.1 (1988), pp. 1–7. DOI: 10.1115/1.3240080.

[208] Young, J. B. "Spontaneous Condensation of Steam in Supersonic Nozzles." In: Physicochemical Hydrodynamics (PCH) 3.1 (1982), pp. 57–82.

[209] Young, J. B. "Two-Dimensional, Nonequilibrium, Wet-Steam Calculations for Nozzles and Turbine Cascades." In: ASME J. Turbomach 114.3 (1992), pp. 569–579.

[210] Ziaja, K. et al. "Numerical Investigation of a Partially Loaded Supersonic ORC Turbine Stage." Under Review. 2020.

Curriculum Vitae

Personal Information

Pascal Post
born 20 June 1988 in Diez, Germany

Professional Experience

since 01/2018	research assistant and doctoral student, team leader "Numerical Methods", chair of Thermal Turbomachines and Aeroengines, department of Mechanical Engineering, Ruhr-Universität Bochum, Germany
2015 – 2017	research assistant and doctoral student, institute of Energy and Power Plant Technology, department of Mechanical Engineering, Technische Universität Darmstadt, Germany
2012 – 2014	student research assistant, institute of Gas Turbines and Aerospace Propulsion, department of Mechanical Engineering, Technische Universität Darmstadt, Germany

Academic Education

2008 – 2015	Mechanical and Process Engineering, Technische Universität Darmstadt, Germany
03/2015	Master of Science with honors
04/2012	Bachelor of Science

Civilian Service

2007 – 2008	Gemeinnützige Schottener Reha GmbH, residential care home for the elderly, Kirberg, Germany

School Education

2004 – 2007	secondary school (Abitur), Peter-Paul-Cahensly Schule, Limburg an der Lahn, Germany
1998 – 2004	secondary school, Tilemannschule, Limburg an der Lahn, Germany
1994 – 1998	elementary school, Astrid-Lindgren Schule, Aarbergen-Kettenbach, Germany